Wide Bandgap Semiconductor Radiation Detectors for Future Space Applications

Thesis submitted for the degree of

Doctor of Philosophy

Shifan Zhao

Space Research Group

School of Engineering and Informatics

University of Sussex

January 2019

Abstract

SiC and $Al_{0.52}In_{0.48}P$ photodiodes were experimentally investigated for their suitability as radiation detectors for use in high temperature (≥ 20 °C) environments applications.

Commercial-off-the-shelf (COTS) 4H-SiC UV p-n photodiodes were repurposed for use as X-ray detectors. Custom-made $Al_{0.52}In_{0.48}P$ p^+-i-n^+ mesa X-ray photodiodes were also studied. The measurements used an ^{55}Fe radioisotope X-ray source. The electrical characterisation of the commercial 4H-SiC UV p-n photodiodes and the $Al_{0.52}In_{0.48}P$ p^+-i-n^+ mesa X-ray photodiodes were investigated at temperatures up to 140 °C and 100 °C, respectively. The photocurrent of the commercial 4H-SiC UV p-n photodiodes were also investigated at temperatures up to 80 °C. The temperature dependences of the energy resolution (*FWHM* at 5.9 keV) of photon counting spectrometers employing these two different kinds of photodiodes are reported, along with shaping time noise analysis.

One of the commercial 4H-SiC UV p-n photodiodes was subsequently characterised under illumination from X-rays of energy 4.95 keV to 21.17 keV, generated by fluorescing high purity metal foils with X-rays from a Mo target X-ray tube. These measurements were conducted at a temperature of 33 °C. The investigation included measurements of spectrometer energy resolution, energy response linearity, and flux linearity measurements.

One of the commercial 4H-SiC UV p-n photodiodes was further studied as a direct electron detector of soft (< 66 keV) electrons (β^- particles) at temperatures up to 100 °C. In addition to experimental measurements, Monte Carlo simulations were conducted and compared with the spectrometer's response.

Results of the research presented in this thesis indicates the commercial 4H-SiC UV photodiodes and the $Al_{0.52}In_{0.48}P$ X-ray photodiodes can be used for high temperature X-rays spectroscopy. Moreover, the results also show that the commercial 4H-SiC UV photodiode can be used for high temperature electron spectroscopy. The work with the 4H-SiC UV photodiodes shows that they can be repurposed for use in low cost X-ray spectroscopy missions, such as CubeSat instrumentation to monitor solar X-rays. The work with the $Al_{0.52}In_{0.48}P$ X-ray photodiodes shows the current state of the art of custom compound semiconductor X-ray detectors specifically designed for such environments.

Acknowledgements

First and foremost, I would like to express my sincere gratitude to my PhD supervisor Prof. Anna M. Barnett for accepting me to pursue my PhD. I also appreciate for her continuous support over my duration of my PhD study, for her patience, motivation, encouragement, and immense knowledge. Her guidance helped me all through my research and the writing of this thesis. I could not have imagined having a better supervisor and mentor for my PhD studies.

I am grateful to Dr Andrey Krysa, for growing the AlInP epitaxial structures, and Dr Robert J. Airey and Saurabh Kumar for fabricating the AlInP devices.

My sincere thanks also go throughout the Space Research Group, particularly Tina Gohil who warmly welcomed me and taught me how to start performing measurements, and Dr Grammtiki Lioliou and Dr Silvia Butera for their useful discussions during data analysis and for their good suggestions for changes and additions to the journal articles which results from this research. My thanks also go to: Michael Whitaker who modified the Labview script to increase the automation level of the temperature experiments; Dr Nathan Gemmell for helping me take the high resolution photographs of the detectors; Dr Elizabeth Rendon for giving me encouragement from time to time; and technician Martin Nock for his technical support during the early days of this research.

Last but by no means least, I would like to dedicate this thesis and expresses my thanks to my dear parents for supporting me spiritually throughout the writing of this thesis and my life in general.

Contents

Publications

Journal articles on work in this thesis

Zhao, S., Gohil, T., Lioliou, G., and Barnett, A.M., 2016, *Soft X-ray Detection and Photon Counting Spectroscopy with Commercial 4H-SiC Schottky Photodiodes*, Nuclear Instruments and Methods in Physics Research A, Vol. 830, pp. 1-5.

> **Zhao, S.**, Gohil, T., Lioliou, G., and Barnett, A.M., 2017, *Corrigendum to 'Soft X-ray detection and photon counting spectroscopy with commercial 4H-SiC Schottky photodiodes' [Nucl. Instrum. Methods Phys. Res. A 830 1–5]*, Nuclear Instruments and Methods in Physics Research A, Vol. 870, pp. 174.

Zhao, S., Lioliou, G., and Barnett, A.M., 2017, *Temperature Dependence of Commercial 4H-SiC UV Schottky Photodiodes for X-ray Detection and Spectroscopy*, Nuclear Instruments and Methods in Physics Research A, Vol. 859, pp. 76-82.

> **Zhao, S.**, Lioliou, G., and Barnett, A.M., 2017, *Corrigendum to 'Temperature dependence of commercial 4H-SiC UV Schottky photodiodes for X-ray detection and spectroscopy' [Nucl. Instrum. Methods Phys. Res. A 859 (2017) 76–82]*, Nuclear Instruments and Methods in Physics Research A, Vol. 870, pp. 175.

Zhao, S., Lioliou, G., and Barnett, A.M., 2018, *X-ray Spectrometer with A Low-cost SiC Photodiode*, Nuclear Instruments and Methods in Physics Research A, Vol. 887, pp. 138-143.

Zhao, S., Lioliou, G., Butera, S., Whitaker, M.D.C., and Barnett, A.M., 2018, *Electron Spectroscopy with a Commercial 4H-SiC Photodiode*, Nuclear Instruments and Methods in Physics Research A, Vol. 910, pp. 35-40.

Zhao, S., Butera S., Lioliou, G., Krysa, A.B., and Barnett, A.M., 2019, *AlInP photodiode X-ray detectors*, Journal of Physics D, Vol. 52, pp. 1-9.

Zhao, S., Butera S., Lioliou, G., Krysa, A.B., and Barnett, A.M., *High temperature AlInP X-ray spectrometers*, in preparation.

Other journal article contributions

Lioliou, G., Butera, S., **Zhao, S**., Whitaker, M.D.C., and Barnett, A.M., 2018, *GaAs Spectrometer for Planetary Electron Spectroscopy*, Journal of Geophysical Research: Space Physics, Vol. 123, pp. 1-13.

Chapter 1 Introduction

1.1 Background

Proportional counters are a type of gas-filled radiation detector, which produce an output signal proportional to the incident radiation energy. They were intensively studied in the early age of X-ray astronomy and widely used in X-ray astronomy missions (e.g. EXOSAT, HEAO-2, and ROSAT). Proportional counters include a windowed gas cell and electrodes. The electrodes are used to provide a number of low and high electric field regions. The electrodes are also used to collect the generated charges by the created electron-ions pairs through the radiation ionisation of gas molecules. Compared to gas-filled detectors, two of the chief benefits of semiconductor radiation detectors are better energy resolutions and smaller volumes. In part, the former is due to the smaller average electron-hole pair creation energy in semiconductors (e.g. 3.62 eV in Si (Bertuccio & Casiraghi, 2003)) cf. the larger electron-ion pair production energy in gas-filled detectors (e.g. ~22 eV in Xe gas at ~1 atm with 5.9 keV X-rays (Borges & Conde, 1996)). The latter is due to the greater density of solid state semiconductors (e.g. 2.33 g/cm^3 for Si at room temperature (Bertuccio & Casiraghi, 2003)) compared with gaseous detector media (e.g. 0.0059 g/cm^3 for Xe gas at 0 °C and 1 atm (Greenwood & Earnshaw, 1997)) which enables higher quantum detection efficiencies in semiconductor detectors even with smaller detector volumes. As such, semiconductor radiation detector systems have been used widely in numerous applications, including in space science (Tavendale & Ewan, 1963) (McKenzie, 1979) (Hassler et al., 2012). Moreover, in order to meet different requirements of different applications, many other radiation detection techniques have been developed, such as flat-panel (Spahn et al., 2000), microchannel plates (MCP) (Ladislas Wiza, 1979), and photostimulated luminescence (PSL) (Miyahara et al., 1986).

At the time of writing, Si is the most commonly used material for semiconductor X-ray detectors. However, its relatively narrow bandgap (E_g = 1.1 eV (Bertuccio & Casiraghi, 2003) at room temperature) means that Si detectors must be cooled (e.g. to -120 °C (Abbey et al., 2003)) in order to achieve sufficiently low thermal noise for optimum operation in photon counting X-ray spectrometers (see **Section 2.7**). For many applications including space science, the introduction of cooling systems is undesirable since it increases the volume, mass, and power consumption of the instrumentation. As such, significant international effort has been dedicated to developing new semiconductor radiation detectors that can operate uncooled at temperatures $\geqslant$ 20 °C. Further impetus to develop new semiconductor detectors is given by the drive for detectors which can resist radiation damage and thus continue to function for longer periods or in harsher radiation

environments than current Si detectors. Radiation hardness characterisation of semiconductor detectors is beyond the scope of this thesis but a relatively recent review is given by Sellin & Vaitkus (2006).

In the quest to produce high temperature tolerant solid state radiation detectors, work has concentrated on wide bandgap semiconductor materials (McGregor & Hermon, 1997) (Sellin, 2003) (Owens & Peacock, 2004) (Zaletin & Varvaritsa, 2011) (Owens, 2012) because of the lower leakage currents detectors made from such materials can possess (see **Section 1.6**).

1.2 Motivation

Narrow bandgap semiconductors detectors, e.g. Si and Ge, require cooling apparatus in order to maintain the optimum operating condition in a high temperature environment. The work presented in this thesis investigates the suitability of two different kinds of wide bandgap semiconductor (4H-SiC and $Al_{0.52}In_{0.48}P$) radiation detectors operating at high temperatures without cooling. If these wide bandgap semiconductor detectors can be used to detect X-rays or electrons, they have the potential to benefit many space science applications that experience restrictions in cost, mass, volume, or energy. Such detectors may be good candidates for radiation spectrometers for future space missions, e.g. investigation of the surface of Mercury. The commercial-of-the-shelf 4H-SiC detectors may be a good choice for budget-limited university-led CubeSat missions, e.g. monitoring solar X-ray activity from Earth orbit. In addition to space applications, radiation detectors can also be used in other potential applications, such as oil condition monitoring, geochemical prospecting (e.g. ocean mining), archaeological provenancing, medical diagnosis, gas detection, nuclear decommissioning, and detection and interdiction of contraband nuclear materials.

1.3 Requirements for space applications

It is essential to consider the mass, volume, power consumption, financial, and environmental restrictions when deploying instruments on board spacecraft. Particularly so for radiation spectrometers that are designed to be deployed on landers or rovers for in situ planetary analysis. The environments in which space instruments have to operate can be extreme in both temperature and radiation dose rate. For example, the two spacecraft comprising the BepiColombo mission to Mercury will have to endured temperatures as high as 400 °C (Benkhoff et al., 2010); a spacecraft visiting Jupiter's moon Europa would have to endure a radiation doses of 20 krad/day

at the surface of Europa (Kolawa et al., 2007). Of course, such instruments must not only survive such extreme conditions; they must also have adequate performance (e.g. in energy resolution and count rate performance) to fulfil their scientific objectives. As such, in order to enable operation of space instruments in such extreme environments, two design approaches exist: use conventional technology and try to protect the instruments (e.g. with radiation shielding and cooling systems) or redesign the instruments to use materials and technologies which are inherently more tolerant of high temperatures and intense radiation.

1.4 X-ray spectroscopy in space science

1.4.1 X-ray spectroscopy in planetary science

X-ray spectrometers play a critical role in the planetary science since they can be used to determine the elemental composition of planetary surfaces through X-ray fluorescence spectroscopy.

X-ray fluorescence spectrometers built for in situ planetary analysis includes the Alpha Particle X-ray Spectrometer (APXS), which was on board Mars Science Laboratory rover (Grotzinger et al., 2012) (landed on Mars in 2012). It was used to measure the chemical composition of Martian soil and rocks to explore the habitability of Mars. A Si drift detector (area of 10 mm^2) was used to detect the fluorescent X-ray energies from ~700 eV to ~25 keV, moreover, a good energy resolution (~140 eV *FWHM* at 5.9 keV) can be achieved when the detector was cooled down to a low temperature (< ~-20 °C) (Gellert et al., 2009).

From a British space science perspective, another important X-ray fluorescence spectrometer was included on the Beagle 2 Mars lander (with which communication was lost during decent to the Martian surface) (Sims et al., 1999). The Beagle 2 X-ray fluorescence spectrometer contained a Si drift detector. The spectrometer was able to detect X-ray photons with energy up to ~15 keV and had an energy resolution (full width at half maximum, *FWHM*) of $\approx$160 eV at 5.9 keV (Fraser, 2008) (Talboys et al., 2009). In order to achieve the optimum operation of the spectrometer, cooling apparatus was used to achieve the operating temperature of -23 °C (Talboys et al., 2009). The Beagle 2 X-ray fluorescence spectrometer had a mass of 0.34 kg and a power consumption of 5 W (Fraser, 2008).

Both of the above X-ray fluorescence spectrometers used internal radioisotope sources to fluoresce their samples. However, remote sensing X-ray fluorescence spectroscopy is also possible; for example, as will be performed by the Mercury Imaging X-ray Spectrometer (MIXS)

that is on board the BepiColombo Mercury Planetary Orbiter (Fraser et al., 2010) (launched on October 2018). By using solar X-rays and solar wind electrons and protons that are incident on the Mercury's surface, MIXS is expected to measure the surface elemental composition of the Mercury to help to address various outstanding questions regarding that planet, e.g. surface evolution processes (Benkhoff et al., 2010). The MIXS detectors can be used to measure the fluorescent X-rays with energies from 0.5 keV – 7.5 keV (with an energy resolution (*FWHM*) of 100 eV at 1 keV) (Fraser et al., 2010).

1.4.2 X-ray spectroscopy in heliophysics

Many heliophysics phenomena can be studied with X-ray spectroscopy.

In the mid-1980s, a solar observatory satellite (Yohkoh) was launched to study plasma heating and particle acceleration processes during solar flares (Ogawara et al., 1991). The main instruments for this on board the satellite included Solar X-ray Telescope (SXT) (Tsuneta et al., 1991), Wide Band Spectrometer (WBS) (Yoshimori et al., 1991), Hard X-ray Telescope (HXT) (Kosugi et al., 1991), and Bragg Crystal Spectrometer (BCS) (Culhane et al., 1991). The WBS contained a soft X-ray spectrometer (two gas proportional detectors), a hard X-ray spectrometer (a NaI scintillation detector), and a γ-ray spectrometer (two bismuth germinate (BGO) scintillation detectors) to detect of X-rays and γ-rays. The soft X-ray spectrometer had an energy resolution (*FWHM*) of 1.18 keV at 5.9 keV and covered the energy range of 2 keV to 30 keV (Yoshimori et al., 1991). Later, in 2002, the Reuven Ramaty High-Energy Solar Spectroscopic Imager (RHESSI) was launched to investigate the processes of particle acceleration and impulsive energy release during solar flares (Lin et al., 2002). A high energy resolution (~1 keV *FWHM* at 3 keV; ~5 keV *FWHM* at 5 MeV) spectrometer was included as part of the RHESSI mission, it contained 9 Ge detectors which were used to detect X-ray and γ-ray photons with energies between 3 keV and 17 MeV; it operated at low temperature (72 K – 76 K) (Lin et al., 2002) (Smith et al., 2002).

A future heliophysics facility will include the ability to stereoscopically map solar flare X-rays by observing the solar flare from two different locations on orbit using Solar Orbiter (Müller et al., 2013) and the Micro Solar-Flare Apparatus (MiSolFA) (Casadei et al., 2017). Both satellites are expected to be launched in 2020. The X-ray imaging spectrometer (Spectrometer/Telescope for Imaging X-rays, STIX) on board Solar Orbiter will be used to study the interaction between the Sun and the heliosphere by imaging the X-ray emission from Bremsstrahlung processes in the near Sun environment (Krucker et al., 2013). STIX and MiSolFA will both use CdTe X-ray detectors (Krucker et al, 2013) (Casadei, 2014) (Grimm et al., 2015). STIX will contain 32 CdTe X-ray detectors providing detection capability for X-rays of energy from 4 keV to 150 keV with

an energy dependent energy resolution (*FWHM*) of 1 keV – 15 keV (Benz et al., 2012).

1.4.3 X-ray spectroscopy in 'general' astronomy

X-ray spectroscopy is a key tool within astronomy today; it can be used to measure the X-rays emitted from astronomical objects and cosmic phenomena, including γ-ray bursts, active galactic nuclei (AGN), stellar coronae, and black holes (Fraser, 1989) (Costa et al., 1997) (Baganoff et al., 2001) (Seward & Charles, 2010). The influence of X-ray astronomy has been and continues to be wide and varied across many areas of astronomical research including stellar evolution, cosmology, and the structure and activity of supernova remnants.

With the discovery of the first extrasolar X-ray source (Sco X-1) in 1962, X-ray astronomy as a distinct field came into being, with many more missions following, including ANS, Ariel V, HEAO-1, ROSAT, and EXOSAT (Elvis et al., 1975) (Trümper, 1982) (Seward & Charles, 2010) (Santangelo & Madonia, 2014). In 1999, the Chandra X-ray Observatory and XMM-Newton were launched as general and complementary X-ray observatories (Jansen et al., 2001) (Schwartz, 2014). The Advanced CCD Imaging Spectrometer (using high-purity Si wafers) is on board Chandra (Garmire et al., 2002), it has a sub-arcsecond angular spatial resolution covering the energy range 0.08 keV to 10 keV (Weisskopf et al., 2002). XMM-Newton uses Si pn-CCDs in its imaging X-ray spectrometer which simultaneously provides X-ray imaging and spectroscopy at energies up to 15 keV (Strüder et al., 2001). Both X-ray space observatories have collected many useful data including details of X-ray emission from black holes and active galactic nuclei (Baganoff et al., 2001) (Weisskopf et al., 2002) (Hameury et al., 2003) (Comerford et al., 2011) (Guainazzi, 2013).

A more specialised X-ray space telescope, the Swift γ-ray explorer was launched in 2004, containing both the Burst Alert Telescope (BAT) and X-ray Telescope (XRT) (Gehrels et al., 2004). BAT was used to detect γ-ray bursts and determine the position of these events, such that the spacecraft could be rapidly oriented to observe these phenomena. In addition, it was also used for hard X-rays observation. BAT includes CdZnTe detectors providing a total detecting area of 5240 cm^2 (through multiple 4 × 4 mm^2 devices), it covers the energy range 15 keV – 150 keV with an energy resolution (*FWHM*) of 6.2 keV at 122 keV (Barthelmy et al., 2005). Following determination of the bust location with BAT, spectra can be collected using the XRT (Burrows et al., 2005). The XRT has an effective area > 120 cm^2 at 1.5 keV and detects photons of energy 0.2 keV to 10 keV with an energy resolution (*FWHM* at 5.9 keV) of 140 eV.

Notable upcoming X-ray astronomy missions include the Large Observatory For X-ray Timing (LOFT) (scheduled for launch in 2022) (Feroci et al., 2012) and Athena (not yet approved, but

anticipated to launch around 2030) (Fioretti et al., 2018).

LOFT is designed to measure rapidly varying X-ray fluxes and spectra to help understand the properties of, and processes at work in, neutron star and black holes (Feroci et al., 2012). In order to meet the scientific requirements of LOFT, the Large Area Detector (LAD) and Wide Field Monitor (WFM) instruments are included in the mission and both use Si Drift Detectors. LAD is designed to have an energy resolution < 260 eV *FWHM* at 6 keV and be able to detect photons in the energy range 2 keV to 30 keV (also be able to extend up to 50 keV). The WFM is expected to have an energy resolution (*FWHM*) of ~300 eV at 5.9 keV and cover the energy range 2 keV to 50 keV. Both instruments are expected to operate at temperatures between -30 °C and 0 °C.

Athena will be equipped with the Wide Field Imager (WFI) (Meidinger et al., 2016) to explore many X-ray related phenomena, e.g. the assemble and formation of baryonic matter and the history of black holes (Barcons et al., 2015). WFI is expected to a have a large field of view (40 arcmin × 40 arcmin), high count-rate capability (≥ 1 Crab), and cover energies from 0.2 keV to 15 keV. DEPFET active pixel detectors will be used (proving energy resolutions ≤ 170 eV *FWHM* at 7 keV) and operating at temperatures between -80 °C to -60 °C (Meidinger et al., 2016).

1.5 Electron spectroscopy in planetary science

Electron spectrometers play a key role in planetary and solar system where they are used to measure energetic electron particle distributions in order to study planetary magnetospheres and plasma environments.

In 1989, the Galileo spacecraft was launched, in 1995 it became the first spacecraft to orbit Jupiter (Johnson et al., 1992) (Williams et al., 1992). The Energetic Particle Detector (EPD) instrument was on board Galileo to measure the particle population in the Jovian magnetosphere. The mass of EPD was 10.5 kg which including the two bi-directional solid-state detector telescopes, Low Energy Magnetospheric Measurement System (LEMMS), and the Composition Measurement System (CMS) (Williams et al., 1992). The power consumption of EPD was 10 W (6 W for the electronics and 4 W for the heaters). Detection of electrons with energies from 15 keV to 11 MeV was achieved with LEMMS which had 8 Si solid state surface barrier detectors. The LEMMS was operated at temperatures between -18 °C to -20 °C.

More recently at Jupiter, the Juno spacecraft has been measuring the distributions of energetic electrons as part of efforts to understand plasma processes in Jovian magnetosphere (Bolton et al., 2017). The measurements are enabled by the Jovian Auroral Distributions Experiment (JADE)

and the Jupiter Energetic Particle Detector Instrument (JEDI). Three identical electron sensors (JADE-Es) of the JADE instrument are for the electrons detection. The JADE-E has a total mass of 5.24 kg (the mass is including radiation shielding) and a total power consumption of 1 W which can measure electrons with energies between ~0.1 keV to ~100 keV (McComas et al., 2017). The Jupiter Energetic Particle Detector Instrument (JEDI), which uses Si drift detectors, is sensitive to electrons of energy 25 keV to 1 MeV. The JEDI has a total mass of 6.4 kg which taking into account the mass of the box structure for shielding (~5 kg), and the operational power for the instrument is 3.1 W (Mauk et al., 2017).

Electron spectroscopy is also of interest in the outer solar system: the Pluto Energetic Particle Spectrometer Science Investigation (PEPSSI) was flown aboard the New Horizons spacecraft to measure energetic particles in the near-Pluto environment (McNutt et al., 2008). The total mass and the power consumption of PEPSSI were 1.475 kg and 2.49 W, respectively. PEPSSI used a solid state Si detector (CCD) array; it enabled detection of energetic electrons with energies from 25 keV to 500 keV, with energy resolution (*FWHM*) of < 5 keV across the interested energy range (McNutt et al., 2008).

1.6 Wide bandgap semiconductors for radiation detection

In this thesis, wide bandgap (WBG) semiconductors are considered to be those with a bandgap energy, $E_g \geq 1.4$ eV at room temperature (Owens, 2012). Semiconductors with $E_g < 1.4$ eV are considered to be narrow bandgap (NBG) materials. Some parameters of the most commonly used NBG semiconductor material (Si) along with the two WBG semiconductor materials use in this thesis (4H-SiC and $Al_{0.52}In_{0.48}P$) are shown in **Table 1.1**.

Parameter	**Si**	**4H-SiC**	**$Al_{0.52}In_{0.48}P$**
Bandgap (eV)	1.12	3.27	2.31
Density (g/cm^3)	2.33	3.21	3.66
Electron-hole pair creation energy (eV)	3.62	7.8	5.34
Fano factor	0.116	0.10	0.12

Table 1.1. Key parameters of Si, 4H-SiC, and $Al_{0.52}In_{0.48}P$ at room temperature (Bertuccio & Casiraghi, 2003) (Bertuccio et al., 2011) (Seyller, 2006) (Cheong et al., 2014) (Butera et al., 2018b). The experimental Fano factor of $Al_{0.52}In_{0.48}P$ has not yet been reported and a conservation assumption Fano factor of the $Al_{0.52}In_{0.48}P$ has been used (Butera et al, 2016a). The density of $Al_{0.52}In_{0.48}P$ was calculated by three steps: 1. Calculation of the compound lattice parameter by using the mixing rule according to Vegard's law (Vegard, 1921) and the Adachi (2005) data. 2. Calculation of the mass of the unit cell of the compound using the mixing rule (Kotz et al., 2008) and the Lide (2003) data. 3. Division of the mass of the unit cell of the compound by the corresponding volume.

NBG semiconductor materials have been widely used in the X-ray spectroscopy applications (Lowe & Sareen, 2013). Si semiconductor technology and instrument readout electronics have advanced sufficiently over the past two decades that the energy resolution (*FWHM*) of cooled Si X-ray detectors now approaches the theoretical limit (i.e. the Fano-limited energy resolution, see **Equation 2.11**) (Nakajima et al., 2005). However, at high temperatures (> 20 °C) the relatively high leakage currents of NBG detectors limit the achievable energy resolution. This is one motivating factor for the development of WBG detectors. The intrinsic carrier concentration of detector's material, n_i (in units of cm^{-3}), plays a critical role in the detector's leakage current (see **Equations 2.4** and **2.5**), and it is related to the bandgap energy of the material, E_g (in units of eV), the Boltzmann constant, k, 1.38 × 10^{-23} JK^{-1}, and the operating temperature, T (in units of K), where

$$n_i \propto e^{\frac{-E_g}{2kT}}. \tag{1.1}$$

NBG semiconductor materials have high intrinsic carrier concentrations (e.g. n_i = 1.4 × 10^{10} cm^{-3}

for Si at room temperature (Bertuccio & Casiraghi, 2003)) which result in high leakage currents, which degrade the performance of such detectors. Therefore, NBG semiconductor detectors require a low temperature operation environment in order to achieve lower intrinsic carrier concentration. In addition, radiation shielding for NBG semiconductor detectors is often required in space applications, as they are easily damaged from radiation and degrade their performance (Lindström, 2003) (Hall & Holland, 2010). Clearly, a radiation detector must be exposed to the radiation which it is required to measure, and as such detectors which are damaged by the radiation they are trying to measure are undesirable in most circumstances.

WBG semiconductor detectors have a lower intrinsic carrier concentration (e.g. 8.2×10^{-9} cm^{-3} for 4H-SiC at room temperature (Bertuccio & Casiraghi, 2003)), which results in lower thermally generated leakage currents even at high operating temperatures (> 20 °C).

However, there are three main limitations that have historically been considered to degrade the performance of the WBG semiconductor detectors. Firstly, many WBG semiconductors have a poorer charge carrier transport properties (e.g. carrier mobility and lifetime) compared to the NBG semiconductors. For example, Si has an electron and hole mobilities of 1400 $cm^2V^{-1}s$ and 1900 $cm^2V^{-1}s$, respectively, whilst 4H-SiC has electron and hole mobilities of 1000 $cm^2V^{-1}s$ and 115 $cm^2V^{-1}s$, respectively. In addition, Si has electron and hole lifetimes ~10^{-3} s whilst those of 4H-SiC are ~10^{-7} s (Owens & Peacock, 2004). The second historical limitation has been the quality of the WBG semiconductors detectors, poor crystalline quality can lead to charge trapping within the detector with the consequence of degraded energy resolution and unstable performance. The third limitation is the degradation in Fano-limited energy resolution which occurs as the bandgap increases (Butera et al., 2018a) as a consequence of increased electron-hole pair creation energy. Additionally, larger electron-hole pair creation energies place more stringent demands on the readout electronics since fewer electron-hole pairs are produced upon absorption of an X-ray of given energy.

However, despite these problems, the motivation to develop WGB detectors is strong because of their utility at high temperature and in environments of intense radiation, and indeed many WBG semiconductor materials have been studied as part of efforts to develop such detectors, e.g. GaAs (Owens et al., 2002) (Lioliou & Barnett, 2016), AlGaAs (Barnett et al., 2015) (Whitaker et al., 2016), SiC (Bertuccio et al., 2004) (Bertuccio et al., 2011), $Al_{0.52}In_{0.48}P$ (Auckloo et al., 2016) (Butera et al., 2016a) (Butera et al., 2016b), GaN (Owens et al., 2012) (Gohil et al., 2016), CdZnTe (Owens, 2012) (Hansson et al., 2014), and $In_{0.5}Ga_{0.5}P$ (Butera et al., 2017).

This thesis reports work on devices made from two WBG materials, 4H-SiC and $Al_{0.52}In_{0.48}P$, with a view to increasing their readiness for use in future space science missions which require

soft X-ray (< 25 keV) and soft electron (< 100 keV) spectrometers. For 4H-SiC, work concentrated on repurpose using two different active area (0.06 mm^2 and 0.5 mm^2) commercial 4H-SiC p-n UV photodiodes as radiation detectors for soft X-ray and soft electron (β^- particle) detection (see **Chapters 3** and **4**). Such work is particularly valuable for cost-sensitive applications such as university-led CubeSat space missions which may require high temperature or radiation tolerant radiation detectors but that cannot afford, or do not have the capability to produce, custom made WBG radiation detectors. For $Al_{0.52}In_{0.48}P$, investigations focused on using custom-made 6 µm i layer thick $Al_{0.52}In_{0.48}P$ p^+-i-n^+ photodiodes for photon counting spectroscopic detection of soft X-rays (see **Chapter 5**). In contrast to the commercially available SiC devices, these $Al_{0.52}In_{0.48}P$ detectors represent some of the most leading edge custom-made WBG detectors available today. For both types of devices, the high temperature performance was investigated. The devices' structures are presented in **Section 1.9**.

1.7 SiC radiation detectors

SiC has excellent physical properties, such as large bandgap (e.g. 4H-SiC (E_g = 3.27 eV (Seyller, 2006)) cf. Si (E_g = 1.12 eV (Owens, 2012))) yielding low thermally generated currents, large breakdown voltages (e.g. 4H-SiC's breakdown voltage is about three times larger than Si (Bertuccio & Casiraghi, 2003)) which provides good visible-blind performance and stable operation. 4H-SiC also had excellent radiation hardness (Nava et al., 2003) (Bertuccio, 2010) (Bertuccio et al., 2013a) (Torrisi et al., 2015) although detailed discussion of this is beyond the scope of this thesis. As such, SiC is a good candidate for radiation detection. The first report of the use of SiC as a particle detector was in 1999; detectors made from a 310 µm thick semi-insulating 4H-SiC substrate and with different sizes of circular Ohmic contacts (1 mm to 3 mm diameter) were illuminated with a ^{90}Sr β^- particle source (Rogalla et al., 1999). Since then, SiC has been studied intensively for particle detection. SiC particle detectors can have high charge collection efficiencies (Bruzzi et al., 2003) (Nava et al., 2004), good linear energy response, and excellent energy resolution (Ruddy et al., 2006) (Zat'ko et al., 2015). SiC particle detectors have also shown stability for extended periods and suitability for operation over a wide range of temperatures (27 °C to 227 °C) (Abubakar et al., 2015).

Outside of particle detection, significant work developing SiC for photon counting X-ray spectroscopy has been conducted and reported with superb results. The first experimental report of X-ray spectroscopy with SiC was in 2001; Np L X-rays and the 59.5 keV γ-ray emissions from an ^{241}Am radioisotope γ-ray source were detected using a heavily n doped 4H-SiC device with a Schottky contact (Bertuccio et al., 2001). SiC was first shown to be suitable for X-ray detection

and spectroscopy at high temperatures (100 °C) in 2002 (Bertuccio et al., 2003), a more detailed study with improved results was subsequently reported in 2004 (Bertuccio et al., 2004). Moreover, the ultra-low leakage current achievable with SiC detectors has stimulated the development of ultra-low-noise charge-sensitive preamplifiers (Bertuccio & Caccia, 2007). SiC detectors coupled to ultra-low-noise preamplifier electronics have been demonstrated with excellent energy resolution (233 eV *FWHM* at 5.9 keV) even at high temperatures (100 °C) (Bertuccio et al., 2011).

In summary, SiC brings benefits of low leakage currents across a wide range temperatures and high radiation tolerance. Thus, SiC detectors are attractive options for space missions and terrestrial applications that have mass, power, and volume restrictions, since the requirements for cooling and shielding for SiC detectors can be less onerous than for silicon detectors. Within space science and astronomy, SiC detectors may find applicability for in situ and remote X-ray fluorescence (XRF) spectrometry of planetary surfaces in high temperature or intense radiation environments (Fraser, 2008) (Seward & Charles, 2010) (Duvet et al., 2014), as well as for investigation of planetary radiation environments, and near sun heliophysics and X-ray astrophysics. Recently, SiC p-n photodiodes intended for UV detection have become widely commercially available. With well-developed fabrication technology and high-quality material, low cost Commercial Off The Shelf (COTS) SiC detectors open the possibility of using SiC detectors for applications such as low cost space science (e.g. as X-ray spectrometers to measure the solar X-rays in low earth orbit or as electron spectrometers to measure the energy and particle density of electrons in low earth orbit and elsewhere). Whilst larger space missions (those comparable to ESA Cosmic Vision S-, M-, and L- Class missions) are likely to continue to use custom-detectors for the foreseeable future, mass-produced COTS SiC detectors may be of value to groups developing CubeSat space science missions at universities and other organisations.

1.8 AlInP radiation detectors

$Al_yIn_{1-y}P$ ($0 < y < 1$) is a III-V WBG ternary compound semiconductor, which has wide range of bandgap energies (1.3 eV < E_g < 3.8 eV at room temperature (Abdollahi et al., 2016)). It is near lattice-matched with GaAs when $y = 0.52$, enabling it to be epitaxially grown on GaAs substrates. Therefore, it has been used in different applications including multi-junction solar cells (Yamaguchi et al., 2006) and undersea optical communications (Cheong et al., 2015).

In the recent years, $Al_{0.52}In_{0.48}P$, which has an indirect bandgap of 2.31 eV at room temperature (Cheong et al., 2014), has attracted interest because of its ability to operate as photon counting X-ray detector. One benefit of $Al_{0.52}In_{0.48}P$ over many of the other wide bandgap materials so far

demonstrated for photon counting X-ray detection is its high X-ray linear attenuation coefficients, μ (in units of cm^{-1}). For example, at 5.9 keV, $Al_{0.52}In_{0.48}P$ has a substantially higher linear absorption coefficient ($\mu_{5.9keV}$ = 1302 cm^{-1}) than 4H-SiC ($\mu_{5.9keV}$ = 346 cm^{-1}), $Al_{0.8}Ga_{0.2}As$ ($\mu_{5.9keV}$ = 640 cm^{-1}), and GaAs ($\mu_{5.9keV}$ = 837 cm^{-1}) (Henke et al., 1993). This leads to a higher quantum detection efficiency for a given detector thickness. The first reported $Al_{0.52}In_{0.48}P$ X-ray detectors were avalanche photodiodes with an avalanche region of 1 µm (Auckloo et al., 2016). Lately, Butera et al. have first reported an energy resolution (*FWHM* at 5.9 keV) of 1.57 keV using an $Al_{0.52}In_{0.48}P$ (2 µm thick i layer) non-avalanche X-ray photodiode at 100 °C (Butera et al., 2016b). Hence, $Al_{0.52}In_{0.48}P$ has started to emerge as a promising material for use in high temperature (> 20 °C) X-ray detectors for space science applications, e.g. in situ planetary/comet analysis, planetary remote sensing, and observations of solar activity.

1.9 Device Structures

1.9.1 4H-SiC UV p-n photodiodes

Four SiC UV p-n photodiodes of two different active areas (0.06 mm^2 and 0.5 mm^2) manufactured by sglux SolGel Technologies GmbH, Berlin, Germany (SGlux SolGel Technologies GmbH, SG01S-18) (SGlux SolGel Technologies GmbH, SG01D-18), were purchased from a standard electronics retailer. The photodiodes were supplied mounted in TO-18 packages. The UV-transparent windows of the TO-18 packages were removed as shown in **Figure 1.1** so that the devices could be directly illuminated with X-rays and β^- particles (electrons). The 4H-SiC structure had an epitaxial layer consisting of a 0.15 µm thick p type layer and a ~5 µm thick n type layer on top of a 4H-SiC substrate. The geometry of the devices can be found in Prasai et al. (2013).

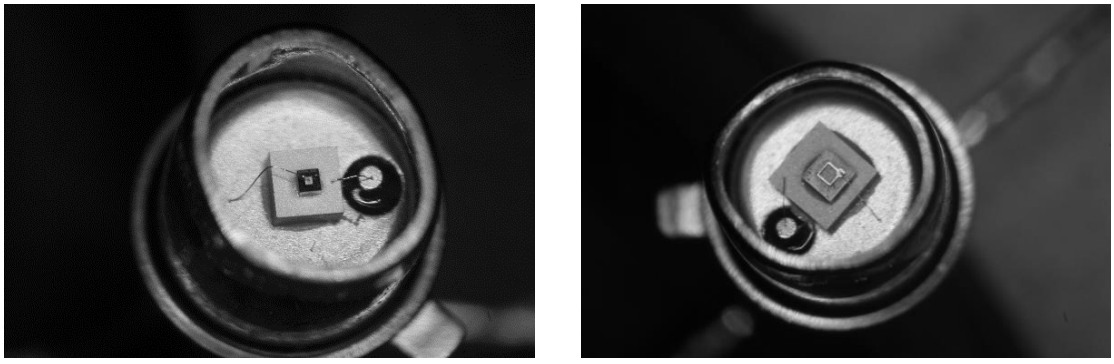

(a) (b)

Figure 1.1. Photograph of one of the packaged (a) 0.06 mm^2 and (b) 0.5 mm^2 4H-SiC UV p-n photodiodes with UV window removed.

1.9.2 $Al_{0.52}In_{0.48}P$ mesa p^+-i-n^+ photodiodes

$Al_{0.52}In_{0.48}P$ p^+-i-n^+ epilayers were grown lattice matched on a commercial (100) GaAs n^+ substrates by metalorganic vapour phase epitaxy (MOVPE) at the EPSRC National Epitaxy Facility, Sheffield, UK. The details of the epilayer are summarised in **Table 1.2**. Device fabrication occurred at University of Sheffield under contract to University of Sussex. Chemical etching techniques were used to fabricate circular mesa photodiodes of two different sizes ($\approx$ 200 µm and $\approx$ 400 µm). Initially, the etching was started using a 1:1:1 H_3PO_4:H_2O_2:H_2O solution. However, because of the slow vertical etch rate achieved, the etching recipe was modified. Thereafter, a 1:1:1 $K_2Cr_2O_7$:HBr:CH_3COOH solution followed by 10 s in a 1:8:80 H_2SO_4:H_2O_2:H_2O solution was used. The diameters of the devices were measured after fabrication to be 217 µm ± 15 µm and 409 µm ± 28 µm, respectively. The stated uncertainties reflect the accuracy of the optical microscope calibration rather than variation of diameter between devices intended to be of the same size.

Top Ohmic annular contacts, Ti/Au (20 nm / 200 nm), were evaporated onto the GaAs p^+ layer of each device. The areas covered by the top contacts were 0.014 mm^2 and 0.041 mm^2 on the 217 µm and 409 µm diameter photodiodes, respectively. An optical microscope photograph showing the geometry of the top contacts is presented in **Figure 1.2**. The rear Ohmic contact, InGe/Au (20 nm / 200 nm), was evaporated onto the reverse of the GaAs n^+ substrate. The detectors were all packaged in a TO-5 can.

Figure 1.2. Photograph of the $Al_{0.5}In_{0.48}P$ photodiodes showing the geometry of the top contacts. The photodiodes at the bottom of the figure are the 409 µm diameter devices; the photodiodes at the top are the 217 µm diameter devices.

Layer	Material	Thickness (μm)	Dopant	Dopant Type	Doping density (cm^{-3})
1	GaAs	0.01	Zn	p^+	1×10^{19}
2	$Al_{0.52}In_{0.48}P$	0.2	Zn	p^+	5×10^{17}
3	$Al_{0.52}In_{0.48}P$	6	undoped		
4	$Al_{0.52}In_{0.48}P$	0.1	Si	n^+	2×10^{18}
5	Substrate n^+ GaAs				

Table 1.2. Layer details of the $Al_{0.52}In_{0.48}P$ structure.

1.10 Thesis organisation

In **Chapter 2**, a review of relevant semiconductor detector physics is given along with an introduction to the experimental methods used. **Chapter 3** presents initial work on the electrical characterisation of commercially available 4H-SiC p-n UV photodiodes and their utility as soft X-ray detectors in spectrometers at temperatures from 0 °C to 100 °C. **Chapter 4** reports further work on one of the photodiodes from **Chapter 3**; here the photodiode was investigated as X-ray detector at X-ray energies from 4.95 keV to 21.17 keV at 33 °C, moreover, the photodiode was further studied as a detector for soft electron spectroscopy at temperatures from 20 °C to 100 °C. **Chapter 5**, provides results from work with custom-made $Al_{0.52}In_{0.48}P$ p^+-i-n^+ photodiodes; the devices were electrically characterised and X-ray spectroscopy is reported at temperatures between 0 °C and 100 °C. **Chapter 6** provides a summary of the work, draws overarching conclusions, and suggests possible future directors for research in these areas.

Chapter 2 Semiconductor Detector Physics and Experimental Methods

2.1 Introduction

This chapter introduces the physical mechanisms by which X-rays and electrons (β^- particles) interact with detectors for the relatively soft radiation energies used in the experiments conducted and reported. Photodiodes, both p-n and p^+-i-n^+ junction varieties, are briefly introduced. A short discussion about the radiation sources used in the experiments is included. A review of the basics of radiation spectroscopy is presented; it contains consideration of detection efficiency, charge generation, and spectrometer noise. The experimental methods used in the thesis are also discussed.

2.2 Interactions of soft X-rays with matter

When X-ray photons interact with matter, the energy of the incident photons can be lost through one or more interaction mechanisms depending on the energy of the incident photon and the atomic number of the material with which it is interacting. These mechanisms are the photoelectric effect, Compton scattering, and pair production (Knoll, 2010) (Owens, 2012) (Leroy & Rancoita, 2016). In this thesis, detectors made from two different semiconductor materials (4H-SiC and $Al_{0.52}In_{0.48}P$) were investigated using relatively soft X-rays (energy < 25 keV); details of the X-rays sources used in the experiments can be found in **Section 2.10.1**. At such energies, the photoelectric effect is the dominant interaction mechanism. The relatively low energy photons interact with the electrons in the shells of the atoms. The energy of the incident photon is transferred to the atom, ejecting a photoelectron (of energy equal to the incident photon less than binding energy) from the shell, resulting in the creation of a vacancy in that shell (Knoll, 2010) (Leroy & Rancoita, 2016). The vacancy is shortly filled by, for example, rearrangement of the higher energy shells of the atom. When an atom undergoes such shell rearrangement, an X-ray fluorescence photon of material specific characteristic energy can be produced (Knoll, 2010) (Leroy & Rancoita, 2016). A full review of X-ray interaction mechanisms is given in Knoll (2010).

X-rays are attenuated (or absorbed) through matter in accordance to the Beer-Lambert Law (Jenkins et al., 1995). The residual intensity, I_r, of a monoenergetic collimated X-ray photon

beam of initial intensity, I_0, passing through a medium of thickness, x (in units of cm), can be calculated by the Beer-Lambert law,

$$I_r = I_0 e^{-\mu_0 x} \tag{2.1}$$

where μ_0 (in units of cm^{-1}) is the linear attenuation coefficient of the absorber (Lowe & Sareen, 2013). The linear attenuation coefficient is given by the product of the absorber's mass attenuation coefficient and density. It should be noted that the attenuation coefficient may be substituted for the absorption coefficient when it is desired to find the fraction of the beam absorbed in the medium rather than attenuated by absorption and other processes.

The linear attenuation coefficients as a function of X-ray energy for $Al_{0.52}In_{0.48}P$, 4H-SiC, and Si are shown in **Figure 2.1** as calculated from the Henke et al. (1993) data. The values for $Al_{0.52}In_{0.48}P$ and 4H-SiC were calculated using the mixing rule (Jenkins et al., 1995) and the Henke et al. (1993) elemental data. The discontinuities are the absorption edges. These edges occur in the linear attenuation (and absorption) coefficient plots at energies equal to the binding energies of the electrons of the atoms present in the medium. At absorption edges, a slightly higher energy photon has a higher probability of being absorbed by the material than the slightly low energy photon; this is because a photon with sufficient energy can not only liberate the electrons in the current shell but also the electrons in the higher energy shell.

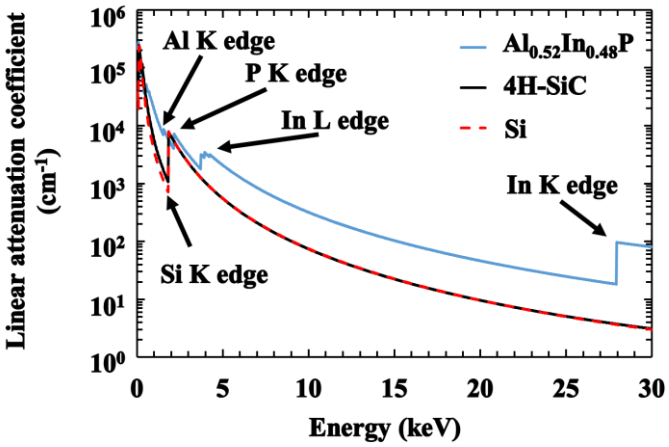

Figure 2.1. Linear attenuation coefficient as a function of X-ray energy for $Al_{0.52}In_{0.48}P$ (blue line), 4H-SiC (black line), and Si (red dash line) Henke et al. (1993). The corresponding absorption edges are also shown.

2.3 Interactions of soft β^- particles with matter

In the work reported in this thesis, a ^{63}Ni radioisotope β^- particle source was used to investigate the response of a 4H-SiC detector to illumination with soft β^- particles (energy < 66 keV). Details of the β^- particle source are given in **Section 2.10.2**. It should be noted that β^- particles are charged particles (energetic electrons) and the interaction mechanism is not identical to that for X-rays.

Whilst a soft X-ray is commonly considered to lose all of its energy in a single localised interaction, the same is not necessarily true for β^- particles. As a β^- particle travels through a medium, the particle's energy is lost along the length of its path. The three main interaction mechanisms for β^- particles are: ionisation and excitation; elastic scattering; and bremsstrahlung radiation (Knoll, 2010) (Owens, 2012) (Leroy & Rancoita, 2016). At the β^- particle energies (< 66 keV) of interest in this thesis, ionisation and excitation is the dominant interaction mechanism. A fast-moving charged particle may transfer its energy to the atomic electrons with the consequence of atomic ionisation. With sufficient energy transfer, an atom may eject an electron. If the ejected electron has sufficient energy, it can cause the next ionisation. Eventually, the β^- particles lose all their energy (Nikjoo et al., 2012) (Owens, 2012). It should be noted that when β^- particles are incident upon matter there is the possibility of backscattering. In such a case only a small portion of the backscattered electrons' energy will be absorbed by the interacted matter. As such, when this occurs at the interface of a detector, little or no energy is deposited in the detector thus preventing efficient detection (Knoll, 2010).

2.4 p-n and p^+-i-n^+ photodiodes in X-ray and β^- particle detection

The research in this thesis concerns p-n and p^+-i-n^+ photodiodes (4H-SiC p-n photodiodes, and $Al_{0.52}In_{0.48}P$ p^+-i-n^+ photodiodes). Compared to p-n photodiode, p^+-i-n^+ photodiode has an intrinsic layer (i region) between the p^+ layer (acceptor doped semiconductor with a large fraction of positive charged holes in the valence band) and the n^+ layer (donor doped with a large fraction of negative charged electrons in the conduction band). Whilst using these kinds of photodiodes for X-ray or β^- particle detection, they are normally reverse biased in order to have a lower capacitance (see **Equation 2.2**). This can reduce the series white noise (see **Section 2.7.3**) and the 1/*f* series noise (see **Section 2.7.4**). It also provides a larger depletion region (if the photodiode is not fully depleted by its internal bias) to allow a larger fraction of the incident X-rays or β^- particles to be absorbed usefully, this increases the photodiode's quantum efficiency (see **Equation 2.9**). Moreover, the electric field strength within the photodiode is increased by reverse biasing the photodiode, which can bring the benefit of the improvement in charge transport. This

can be important to ensure optimal operation of the detector. In this section, a review of the fundamental physics of the operation of p-n (p^+-i-n^+) photodiodes under reverse bias is presented.

Under thermal diffusion, holes diffuse from the p side into the n side and leaving the negative acceptor ions at the junction, meanwhile, electrons diffuse from the n side into the p side and leave thing positive donor ions at the junction. It should be noted that the i layer of p^+-i-n^+ photodiode is an intrinsic region, which is a notionally pure semiconductor with ideally no doping. However, some residual unintentional doping will always be present. Electrons and holes can easy travel in this region. Therefore, a mobile carrier free region is formed; such a region is called the depletion region or depletion layer. At thermal equilibrium, a potential barrier is formed between the p side and n side, limiting the diffusion of charge. When the photodiode is reverse biased, the potential barrier is increased (electron and hole concentrations reduced) along with the increased depletion width. The mobile carriers within the depletion region are swept towards the electrodes, under the influence of the electric field created by the applied reverse bias. Moreover, with the increased reverse bias, the depletion region will increase possibly enabling the photodiode to be fully depleted (i.e. depletion width = i layer width) before the breakdown voltage of the photodiode is reached. A high electric field strength in the i layer leads to improvement in charge transport (Spieler, 2005) (Sze & Ng, 2007).

When a p-n or p^+-i-n^+ photodiode is connected in a reverse bias condition, the capacitance of the p-n and p^+-i-n^+ photodiode can be considered to arise from the depletion region capacitance, C_d, as shown (Schroder, 2006) (Sze & Ng, 2007),

$$C_d = A_d \sqrt{\frac{q\varepsilon_0 \varepsilon_r N_D}{2\left(V_{bi} - V_R - \frac{kT}{q}\right)}} \tag{2.2}$$

where ε_0 is the permittivity of free space, ε_r is the relative permittivity of the detector material (9.3 for 4H-SiC (Patrick & Choyke, 1970); 11.25 for $Al_{0.52}In_{0.48}P$ (Ong et al., 2011)), A_d is the area of the photodiode, V_{bi} is the built-in voltage, V_R is the applied reverse bias voltage, N_D is the doping concentration in the depletion region, q is the elementary charge.

The depletion region thickness, W, is inversely proportional to the depletion region capacitance, and can be expressed as (Schroder, 2006),

$$W = \frac{\varepsilon_0 \varepsilon_r A_d}{C_d} \tag{2.3}$$

The total reverse leakage current of a p-n or p^+-i-n^+ junction consists the diffusion and generation currents (Sze & Ng, 2007). The diffusion current is predominant at high temperatures, whereas

the generation current becomes dominant at low temperatures. The diffusion current, I_{diff}, is related to the area of the photodiode, the intrinsic carrier concentration, and determined by the acceptor and donor concentrations, N_a, and N_d, the diffusion coefficient and the diffusion length of the electrons in the p layer, D_n and L_n, and the diffusion coefficient and the diffusion length of the holes in the n layer, D_p and L_p, as shown,

$$I_{\text{diff}} = \text{q}A_{\text{d}}n_{\text{i}}^2\left(\frac{D_{\text{p}}}{N_{\text{d}}L_{\text{p}}} + \frac{D_{\text{n}}}{N_{\text{a}}L_{\text{n}}}\right) \tag{2.4}$$

The generation current, I_{gen}, is proportional to the area of the photodiode, the intrinsic carrier concentration, and the thickness of the depletion region. It is also inversely proportional to the generation lifetime, τ_g, as expressed by,

$$I_{\text{gen}} = \frac{\text{q}A_{\text{d}}n_{\text{i}}W}{2\tau_{\text{g}}}. \tag{2.5}$$

When a significant high reverse direction electric field is applied to the p-n or p^+-i-n^+ photodiode, it may induce junction breakdown which can result in a large current passing through the photodiode. The photodiodes used in this research were operated in such conditions as to prevent junction breakdown; breakdown can irreparably damage the performance of a radiation detector and should be avoided except for detectors specifically designed to operate in the breakdown region. Two main mechanisms of junction breakdown include the tunnelling effect and avalanche multiplication. The tunnelling effect occurs when a large reverse bias is applied to a high doping concentration p-n junction; electrons in the valance band penetrate through the energy bandgap into the conduction band. Avalanche multiplication (also known as impact ionisation) may occur in a moderately doped p-n or p^+-i-n^+ junction under a large enough reverse bias. Electrons in the depletion region may acquire sufficient energy from the applied electric field and interact with atoms, consequently generating further electron-hole pairs. Those electron-hole pairs may then themselves gain sufficient energy to create more electron-hole pairs, with the consequence of a 'snowballing' or avalanche of charge creation (Sze & Ng, 2007).

When X-ray photons or energetic electrons are absorbed by a semiconductor detector, a number of electron-hole pairs will be created (a more detailed discussion can be found in **Section 2.6**), and the generated charge carriers will contribute to the device's current. Such photon (or particle) generated current, I_{photon} and electron generated current, $I_{electron}$, can be calculated using **Equations 2.6** and **2.7**, respectively.

$$I_{\text{photon}} = \frac{A_{\text{Fe}}}{2}\frac{A_{\text{d}}}{A_{\text{source}}}\left(Em_{\text{K}\alpha}T_{\text{K}\alpha}QE_{\text{K}\alpha}\frac{5900}{\omega_{\text{ehp}}} + Em_{\text{K}\beta}T_{\text{K}\beta}QE_{\text{K}\beta}\frac{6500}{\omega_{\text{ehp}}}\right)\text{q} \tag{2.6}$$

and

$$I_{\text{electron}} = \sum_{i=start\ point\ energy=1\ (\text{keV})}^{end\ point\ energy\ =\ 66\ (\text{keV})} \frac{A_{\text{Ni}}}{2} E_{mi} \frac{A_{\text{d}}}{A_{\text{source}}} DE_i \frac{i}{\omega_{ehp}} \text{q} \quad (2.7).$$

In **Equation 2.6**, A_{Fe} is the activity of the ^{55}Fe radioisotope X-ray source, A_{source} is the active area of the radioisotope source, $Em_{\text{K}\alpha}$ and $Em_{\text{K}\beta}$ are the dimensionless emission probabilities of the Mn Kα and Mn Kβ X-rays from the ^{55}Fe radioisotope X-ray source, $T_{\text{K}\alpha}$ and $T_{\text{K}\beta}$ are the dimensionless transmission probabilities of the Mn Kα and Mn Kβ X-rays through the radioisotope source's Be window, and the $QE_{\text{K}\alpha}$ and $QE_{\text{K}\beta}$ are the dimensionless quantum efficient of the detector at 5.9 keV and 6.5 keV which can be calculated using **Equation 2.9**, ω_{ehp} (in units of eV) is the average electron-hole pair creation energy which is related to the bandgap of the semiconductor material (Butera et al., 2018a). Details of the ^{55}Fe radioisotope X-ray source can be found in **Section 2.10.1**.

In **Equation 2.7**, A_{Ni} is the apparent activity of the ^{63}Ni radioisotope β^- particle source thus including consideration of self-absorption (Alam & Pierson, 2016), E_{mi} (a dimensionless quantity) is the emission probability of the ^{63}Ni radioisotope β^- particle source adjusted for self-absorption (Liu et al., 2015), DE_i (a dimensionless quantity) is the percentage of each electron energy deposited in the active region of the detector, considering the losses before the β^- particles reach the active region of the detector (e.g. losses in the protective overlayer of the source, and the atmosphere between the source and detector) and the quantum efficiency of the detector which may be calculated from **Equation 2.8**. Details of the ^{63}Ni radioisotope β^- particle source can be found in **Section 2.10.2**.

2.5 Quantum Detection efficiency

The quantum detection efficiency (*QE*) of a radiation semiconductor detector can be defined as

$$QE = \frac{N_{\text{deposited}}}{N_{\text{incident}}} \quad (2.8)$$

where $N_{\text{deposited}}$ is the number of radiation quanta deposited in the active region, N_{incident} is the number of radiation quanta incident on the detector. Since the incoming X-ray photons or β^- particles may need to go through some dead layers (depending on the detector's structure) before they reach the detector's active region (considered to be the entire epitaxial layer for the SiC p-n photodiodes, but solely the i layer for the $Al_{0.52}In_{0.48}P$ p^+-i-n^+ photodiodes). Therefore, the quantum detection efficiency of a semiconductor detector is expressed more usefully as

$$QE = (\prod_m e^{-\mu_m t_m})(1 - e^{-\mu_s d}) \quad (2.9)$$

where the first term is the linear attenuation coefficient of the *m*th dead layer, μ_m (in units of μm^{-1}), and the thickness of the *m*th dead layer, t_m; the second term is the linear attenuation coefficient of the active layer, μ_s, and the thickness of the active layer, d (Fraser, 1989).

2.6 Charge generation

In this thesis, the soft X-ray photons are absorbed in semiconductor photodiode by the photoelectric effect. The process by which β^- particles are absorbed in the semiconductor photodiode is slightly different. However, the consequence of both processes is the same: a number of charge carriers (electron-hole pairs) are created. The average number of generated electron-hole pairs, N_{gen}, is given by,

$$N_{\text{gen}} = \frac{E}{\omega_{\text{ehp}}} \tag{2.10}$$

where E is the absorbed energy and ω_{ehp} is the material's characteristic electron-hole pair creation energy, which is considered here to be photon energy invariant across the photon and electron energies used in this thesis (Fraser et al., 1994).

However, the process of charge creation is probabilistic. As such, variation in the number of electron-hole pairs created from one absorption event to the next is expected, even when the same amount of energy is deposited (Owens, 2012). If the charge generation process was Poissonian, the statistical fluctuation in the total number of the created charge carriers would be $\sqrt{N_{\text{gen}}}$. However, the observed variation in the number of created charge carriers is not Poissonian; this is because the creation of each electron-hole pair in the multitude of electron-hole pairs is not independent. Therefore, a dimensionless factor (the Fano factor, F, (Fano, 1947)) is defined,

$$F = \frac{Observed\ variance}{Poissonian\ predicted\ variance}. \tag{2.11}$$

The Fano factor is necessarily between 0 and 1. For semiconductors $F \approx 0.1$ (0.116 for Si (Bertuccio & Casiraghi, 2003); 0.10 for 4H-SiC (Bertuccio et al., 2011); and, as yet, unmeasured for $Al_{0.52}In_{0.48}P$, but commonly assumed to be ≈ 0.12).

Such statistical fluctuation in the number of created charge carriers sets a fundamental limit to the best energy resolution possible with radiation spectrometers made of each material. The Fano noise (the ultimately achievable energy resolution, if all other noise sources are nil) is given by

$$FWHM_{\text{Fano}}[\text{eV}] = 2.355\sqrt{FE\omega_{\text{ehp}}} \tag{2.12}$$

where all terms have been defined previously.

2.7 Non-Fano noises in non-avalanche semiconductor X-ray and β^- particles photodiode spectrometers

2.7.1 Introduction

The energy resolution of a non-avalanche semiconductor detector spectrometer is broadened not only by the Fano noise, but also other noise sources, namely electronic noise and incomplete charge collection noise, such that **Equation. 2.12** becomes,

$$FWHM\ [\text{eV}] = 2.355\sqrt{FE\omega_{\text{ehp}} + M^2 + aE^b} \tag{2.13}$$

where M is equivalent noise charge of the electronic noise (in units of eV), aE^b is the equivalent noise charge of the incomplete charge collection noise (in units of eV), a and b are dimensionless parameters which are treated as semi-empirical constants determined by best-fitting (Owens, 2012). The electronic noise arises from the detector and the preamplifier system (Bertuccio et al., 1996). The incomplete charge collection noise arises from charge losses as the carriers are swept to the contacts; it depends on the detector's charge diffusion and collection properties, and the trap density distribution (Owens, 2012). The electronic noise includes parallel white noise, series white noise, 1/f series noise, dielectric noise, and induced gate current noise. Each of which are summarised below.

2.7.2 Parallel white noise

The shot noise of the leakage current of the detector, I_{LD}, and the input JFET gate current of the preamplifier, I_{LT}, are the main noise contributors to the parallel white noise contributors (Bertuccio et al., 1996). If there is a feedback resistor in the preamplifier, R_{f}, the shot noise of it also contributes to the parallel white noise (Bertuccio et al., 1996). The parallel white noise power spectral density can be expressed as

$$S_{\text{WP}}[\text{V}^2/\text{Hz}] = 2\text{q}\alpha(I_{\text{LD}} + I_{\text{LT}}) + \frac{4\text{k}T}{R_{\text{f}}} \tag{2.14}$$

where α is a dimensionless constant parameter, (α = 1 in the case of the total leakage current = I_{LD} + I_{LT}). The contribution of parallel white noise's equivalent noise charge, ENC_{WP}, is

$$ENC_{\mathrm{WP}}[\mathrm{e^-rms}] = \frac{1}{\mathrm{q}}\sqrt{\frac{A_3}{2}S_{\mathrm{WP}}\tau} \tag{2.15}$$

where A_3 is a dimensionless constant factor (0.5 to 3.6) and depending on the type of the implemented shaping amplifier (A_3 = 1.85 for the RC-CR shaping amplifier), and τ is the shaping time of the shaping amplifier (Gatti et al., 1990) (Bertuccio et al., 1996). Because the parallel white noise is related to the leakage current of the detector and the shaping time, when the detector has a large leakage current, shorter shaping times are typically used to minimise the parallel white noise.

2.7.3 Series white noise

The thermal noise in the preamplifier's input JFET's drain current is the dominant noise contributor to the series white noise (Bertuccio et al., 1996). The series white noise power spectral density, S_{WS}, is proportional to a dimensionless parameter, γ, and inversely proportional to the JFET transconductance, g_m. The parameter γ is determined by the JFET bias condition and the gate length (Klaassen, 1971). The series white noise power spectral density is given by,

$$S_{\mathrm{WS}}[\mathrm{V^2/Hz}] = \gamma\frac{4\mathrm{k}T}{g_m}. \tag{2.16}$$

The series white noise equivalent noise charge, it is also dependent on the total capacitance at the preamplifier input, C_{T}, and the shaping time of the shaping amplifier. It can be expressed by,

$$ENC_{\mathrm{WS}}[\mathrm{e^-\ rms}] = \frac{1}{\mathrm{q}}\sqrt{\frac{A_1}{2}S_{\mathrm{WS}}C_{\mathrm{T}}^2\frac{1}{\tau}} \tag{2.17}$$

where A_1 is a dimensionless constant (ranging from 0.5 to 4) determined by the type of the shaping amplifier, e.g. A_1 = 1.85 for an RC-CR shaping amplifier (Gatti et al., 1990). When a radiation detector has a large capacitance, a longer shaping time may be selected to minimise the series white noise.

2.7.4 1/f series noise

The 1/f series noise arises from noise in drain current of the preamplifier's input JFET (Lioliou & Barnett, 2015). The 1/f series noise is shaping time independent and increases with greater total capacitance at the preamplifier's input. The 1/f series noise equivalent noise charge, $ENC_{1/f}$, can be expressed as

$$ENC_{1/f}[\mathrm{e^-rms}] = \frac{1}{\mathrm{q}}\sqrt{A_2\pi A_f C_{\mathrm{T}}^2} \tag{2.18}$$

where A_2 is a dimensionless constant (0.64 to 2) determined by the type of shaping amplifier (A_2 = 1.18 for the RC-CR shaping amplifier) (Gatti et al., 1990) (Bertuccio et al., 1996), and A_f is a dimensionless characteristic constant of the preamplifier's input JFET (Lioliou & Barnett, 2015).

2.7.5 Dielectric noise

Thermal fluctuations in insulators in close proximity to the preamplifier's input cause dielectric noise (Bertuccio et al., 1996). Contributions from the feedback capacitance, test capacitance, as well as the input JFET and detector themselves along with the packaging materials of these components all increase the dielectric noise (Pullia & Bertuccio, 1996). The dielectric noise's equivalent noise charge, ENC_{D}, is given by

$$ENC_{\mathrm{D}}[\mathrm{e^-rms}] = \frac{1}{\mathrm{q}}\sqrt{A_2 2\mathrm{k}TDC_{\mathrm{die}}} \tag{2.19}$$

where D is the dielectric dissipation factor, and C_{die} is the capacitance of the lossy dielectrics, (Bertuccio et al., 1996). It should be noted that the dielectric noise is shaping time independent. Directly wire bonding the detector to the gate of the input JFET can reduce the quantity of lossy dielectric material in proximity to the gate of the preamplifier by elimination of packaging materials and can thus reduce dielectric noise (Bertuccio et al., 1995). Based on that concept, Depleted Field Effect Transistor detectors (DEPFETs) were designed and can achieve very good energy resolutions (e.g. 191 eV *FWHM* at 5.9 keV) (Zhang et al., 2006).

2.7.6 Induced gate current noise

The induced gate current noise is due to fluctuations in the drain current (see **Section 2.7.3**); the gate and the channel of the JFET are capacitively coupled (Lioliou & Barnett, 2015). As such, the induced gate current noise is correlated with the series white noise, S_{WS}, and a dimensionless correction factor, G_{C}, (commonly taken such that $\sqrt{G_{\mathrm{C}}} \approx 0.8$ (Bertuccio et al., 1996)). The induced gate noise power spectral density taking in to account the series white noise can be expressed as

$$S_{\mathrm{WSC}}[\mathrm{V^2/Hz}] = S_{\mathrm{WS}}G_{\mathrm{C}}. \tag{2.20}$$

The corresponding equivalent noise charge, ENC_{WSC}, is given by

$$ENC_{\mathrm{WSC}}[\mathrm{e^-\ rms}] = ENC_{\mathrm{WS}}\sqrt{G_{\mathrm{C}}}. \tag{2.21}$$

2.7.7 Incomplete charge collection noise

Incomplete charge collection noise arises as a consequence of either the trapping or recombination

of radiation-created charge carriers in the detector (Owens, 2012). This results in those charge carriers not being able to induce their complete charge on the contacts of the detector, with a subsequent reduction of the energy position at which the corresponding count occurs in the spectrum. To some extent, a reduction in trapping noise, when it is present, can be achieved by increasing the electric field applied to the detector to increase carrier drift length. A universally applicable physical model of charge trapping noise does not exist.

2.8 Method of measurements of photodiodes' currents as functions of applied reverse bias

In this thesis, the currents of the photodiodes were measured as functions of applied reverse bias using a Keithley 6487 Picoammeter/Voltage source. The picoammeter can supply voltages from ±200 μV to ±505 V, and has a current measurement range from ±10 fA to ±21 mA. The uncertainty associated with the current reading was related to the selected current range; for the 2 nA current range used in this thesis, the uncertainty was 0.3% of the current reading + 400 fA, while the current reading was within the current range of 2 nA (Keithley Instruments, 2011).

In order to measure the leakage current of an investigated photodiode, the investigated photodiode was installed in a light-tight aluminium box. The voltage source output and the current input of the Keithley 6487 were connected to the cathode and the anode of the photodiode, respectively. The photodiode was reverse bias by applying a positive voltage. Because the measurement cables (for current input to picoammeter) themselves may have non-zero leakage currents and contribute charge to the measurement through the tribocharging of their insulators both which can affect the measurements at low signal levels, custom high quality triaxial cables were used providing signal, guard, and shield conductors (Keithley Instruments, 2013).

The voltage source output of the Keithley 6487 used two standard banana sockets, they were connected to the signal and shield conductors of a high quality PTFE insulated SMA coaxial cable through a dual banana to BNC adapter and then a BNC to SMA adaptor, the Output High and the Output Low were connected to the signal and shield line of the coaxial cable, respectively.

The light-tight aluminium box had two connectors (triaxial socket and SMA socket), the guard and the shield of the triax connector were connected to the aluminium box, the shield of the SMA connector was connected to the aluminium box as well. Hence, the aluminium box was served as the ground of the measurement system as the Output Low of the Voltage source of the Keithley 6487, and the Input Low and the Chassis ground of the Current Input of the Keithley

6487 were all connected to the aluminium box.

Whilst measuring the radiation generated current of an investigated photodiode, the investigated photodiode along with a PTFE radiation source's holder were installed in the light-tight aluminium box. The investigated detector was positioned central to the aperture of the source's holder. The radiation generated current measurement was completed in two steps. Firstly, the current of the investigated detector was measured without any radiation illumination in the light-tight aluminium box. Secondly, the current of the investigated detector was measured under illumination of the ^{55}Fe radioisotope X-ray source or the ^{63}Ni radioisotope β^- particles source in the light-tight aluminium box. It should be noted that a better set up for this kind of measurement could be been achieved in principle using a chopper wheel and lock-in amplifier to avoid any disturbance from placing the radioisotope source or time variation of the detector's leakage current.

When measuring the leakage current of the investigated photodiode at different temperatures, the light-tight aluminium box which contained the investigated detector was installed in a TAS Micro MT climatic cabinet for temperature control.

National Instruments Labview software was used to automate the current measurements reported in this thesis.

2.9 Method of measurements of photodiodes' capacitances as functions of applied reverse bias

In this thesis, the measurements of the investigated photodiodes' capacitances as functions of applied reverse bias were made using an HP 4275A Multi frequency LCR meter (Hewlett Packard, 1979) and a Keithley 6487 Picoammeter/Voltage Source (Keithley Instruments, 2011) as the external voltage supply. The Voltage Source Output of the Keithley 6487 was connected to the EXT ± 200V of the LCR meter through a high-quality PTFE insulated SMA coaxial cable. The HP 4275A LCR meter had a capacitance measurement range from 1000 fF to 100 μF. The uncertainty in the capacitance reading were related to the value of the capacitance reading (e.g. 0.1% of reading + 3 counts), and the accuracy multiple factor which was related to the AC test signal (e.g. an accuracy multiple factor of 1.17 corresponded to an AC test signal of 60 mV rms). The LCR meter was used in its four terminal capacitance measurement mode. Further details of the HP 4275A LCR meter can be found in its manual (Hewlett Packard, 1979).

In order to eliminate adverse effects from light and electromagnetic interference, each

investigated photodiode was mounted in a custom-made light-tight aluminium box. The custom-made light-tight aluminium box had two connectors (SMA sockets), they were connected to a custom-made adapter which was attached to the HCUR, HPOT, LPOT, and LCUR of the LCR meter by two SMA coaxial cables through two dual banana to BNC adapters and then two BNC to SMA adaptors. The shield of the SMA connectors was connected to the aluminium box and the box was served as the ground of the measurement. The zero offset adjustment was used before each capacitance measurement to automatically normalise the readout offset due to the residuals inherent stray capacitance, residual inductances and resistances from the test fixture, attached cables and wires. The zero offset adjustment was completed in two steps, 1. Zero Open check (without connecting anything to the test wires) by setting the AC test voltage signal magnitude and frequency to 1 V rms and 1 MHz; 2. Zero Short check by shorting the test wires. After completed the zero offset adjustment, the investigated photodiode was connected to the test wires with setting the magnitude AC test voltage signal to 60 mV rms.

When measuring the photodiodes' capacitance at varying temperature, the zero offset adjustment was completed inside the cabinet at 20 °C. National Instruments Labview software was used to automate the measurements.

2.10 Radiation sources

Two difference X-ray sources (Eckert and Ziegler 3204-encapsulated ^{55}Fe radioisotope X-ray source; LD Didactic X-ray apparatus with a Mo X-ray tube), and one β^- particle source (custom-made Eckert and Ziegler ^{63}Ni radioisotope β^- particle source) were used to study the radiation response of the investigated photodiodes. The sources are briefly discussed in this section.

2.10.1 X-ray sources

An Eckert and Ziegler 3204-encapsulated ^{55}Fe radioisotope X-ray source was used to investigate the response of the 4H-SiC photodiodes (see **Sections 3.3** and **3.5**) and $Al_{0.52}In_{0.48}P$ photodiodes (see **Sections 5.3.1** and **5.5.1**). The ^{55}Fe was electrodeposited as iron metal on the face of a copper disc, sealed in a welded Monel capsule with brazed 0.25 mm thick Be window. The active area of the source was 28.27 mm^2. The original activity of the ^{55}Fe radioisotope source was 370 MBq, and its activity at the time of the specific measurements is given where those measurements are reported. ^{55}Fe decays by electron capture producing characteristic Mn Kα and Kβ X-ray lines (5.9 keV and 6.49 keV). The relative emission probabilities of these lines are: Mn Kα 5.9 keV = 0.245; Mn Kβ 6.49 keV = 0.0338 (Schötzig, 2000). The transmission probabilities of

the Mn Kα and Mn Kβ X-rays through the source's Be window were calculated to be 0.576 and 0.667, respectively (Cromer & Liberman, 1970) (Hubbell, 1982).

Investigation of the X-ray energy dependent response of the photodiodes was performed by using an LD Didactic X-ray apparatus (part number 554 800) along with a Mo X-ray tube (part number 554 861) (Mo Kα = 17.4 keV; Kβ = 19.6 keV) and with eight high-purity metal foils (see **Section 4.3**). The Mo cathode X-ray tube was used to fluorescence the foils to produce characteristic X-ray emission lines (X-ray energies from 4.95 keV to 21.17 keV) (see **Table 2.1**) with which to characterise the instrument. The X-ray tube had a voltage range from 0.0 kV to 35.0 kV with step width of 0.1 kV. The X-ray tube emission current was adjustable from 0.00 mA – 1.00 mA with step width of 0.01 mA. For all the measurements reported the tube was operated at 35.0 kV. An LD Didactic goniometer (part number 554 831) and target stand were used to position the spectrometer and fluorescence foils respectively (LD Didactic GmbH, N.D.).

Material	**$K\alpha_1$ line energy (keV)**	**$K\beta_1$ line energy (keV)**
V	4.95	5.42
Cr	5.41	5.94
Mn	5.89	6.49
Cu	8.04	8.90
Zn	8.63	9.57
Ge	9.88	10.98
Nb	16.61	18.62
Pd	21.17	23.81

Table 2.1. The high-purity (≥ 98.7%) metal foils used, together with the two primary X-ray emission line energies used. The emission line energies were drawn from Sánchez del Rio et al. (2003).

2.10.2 Radioisotope β^- particle source

A custom-made Eckert and Ziegler ^{63}Ni radioisotope β^- particle source (^{63}Ni endpoint energy = 66 keV) was used to investigating the response of one of the 4H-SiC photodiodes to soft β^- particles (see **Sections 4.4.2** and **4.4.3**). The ^{63}Ni radioisotope β^- particle source had an active

face area of 49 mm^2 with an original activity of 185 MBq. The activity of the source at the time of the measurements is detailed where those measurements are reported. It consisted of a 3 μm thick ^{63}Ni layer electroplated onto a ~50 μm thick inactive Ni foil substrate and then covered with a protective 1 μm thick inactive electroplated Ni overlayer. The emission probability of the ^{63}Ni radioisotope β^- particle source adjusted for self-absorption taking into account its thickness but excluding attenuation due to the protective Ni overlayer is shown in **Figure 2.2**.

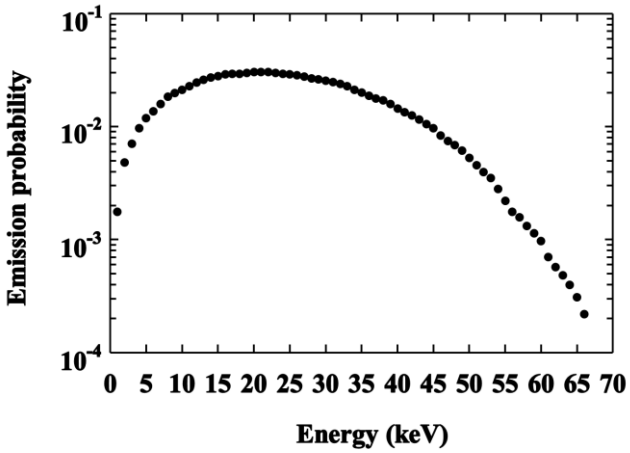

Figure 2.2. The emission probability of the ^{63}Ni radioisotope β^- particle source adjusted for self-absorption (based on Liu et al., (2015)).

2.11 Photon counting X-ray and particle counting β^- spectroscopy

In this thesis, the investigated photodiodes were each in turn connected to two different custom-made low-noise charge-sensitive preamplifiers and operated as spectrometers. Both preamplifiers were of feedback resistorless design similar to Bertuccio et al. (1993). The elimination of the feedback resistor in the preamplifier circuit is achieved with an additional feedback loop for stabilising the working point of the preamplifier and utilising a slightly forward bias n type JFET, as a path for the feedback capacitor discharge (Bertuccio et al., 1993). One of the preamplifiers had a wire-ended packaged 2N4416A Si JFET (capacitance = 2 pF) (Siliconix, 2001) as the input transistor and was used in spectrum accumulation mode to obtain spectra of the ^{55}Fe radioisotope X-ray source and the ^{63}Ni radioisotope β^- particle source. The other preamplifier contained a wire-ended packaged 2N4416 Si JFET (capacitance = 2 pF) (Siliconix, 2001) as the input transistor and was used in the accumulation of the fluoresced X-ray spectra inside the LD Didactic X-ray apparatus. The performance of the preamplifiers was sufficiently similar that they can be considered as identical for the purposes of measurements reported.

A Keithley 6487 Picoammeter/Voltage source was used as a voltage source to reverse bias the investigated photodiodes. Each of investigated photodiode was only biased while accumulating the radiation spectra. Both preamplifiers were biased constantly through the spectra accumulation measurement by a TTi PL303QMD-P power supply. In all cases, the output of the preamplifier was connected to an ORTEC 572A shaping amplifier. The output of the shaping amplifier was connected to an ORTEC EASY-MCA 8k multi-channel analyser (MCA) for digitisation. A block diagram of the connection of the instruments can be found in **Figure 2.3**.

When X-ray photons or β^- particles were usefully absorbed in the semiconductor detector, the electron-hole pairs which were created were swept out of the detector by virtue of the applied reverse bias. The movement of the electron-hole pairs induced charge on the contacts of the detector in accordance with Schockley-Ramo theorem (He, 2001). The charge-sensitive preamplifier converted this charge pulse to a proportionally-sized voltage pulse. A pulse generator can be used to simulate a detector by charging a capacitor within the preamplifier which then deposits that charge at the input of the preamplifier similarly to as would occur with a detector. The voltage tail pulse from the output of the preamplifier was further processed by the shaping amplifier to improve the signal-to-noise ratio and facilitate onwards digitisation. The output of the shaping amplifier was connected to the MCA which digitised the pulses and binned them in such a way as to form a histogram which is the spectrum.

When obtaining the spectra from the ^{55}Fe radioisotope X-ray source (Mn Kα = 5.9 keV; Mn Kβ = 6.49 keV) and the ^{63}Ni radioisotope β^- particle source (^{63}Ni endpoint energy = 66 keV), each radioisotope source was positioned above the photodiode upon a custom-made PTFE source holder. For the temperature dependence X-ray spectra accumulation, the investigated photodiodes along with the preamplifier were installed in the TAS Micro MT climatic cabinet for temperature control but the shaping amplifier and the MCA remained outside of the cabinet and were operated at room temperature. In order to ensure thermal equilibrium of the photodiodes and preamplifier with the atmosphere of the chamber at each temperature, the spectrometers were allowed to stabilise for 30 min before the spectra accumulation at each temperature.

While accumulating the spectra of the fluoresced X-ray foil targets using the LD Didactic X-ray apparatus, the spectrometers were positioned within radiation chamber of the apparatus. The sample stand was positioned at 45° with respect to the collimator. The spectrometer was positioned at 135° with respect to the collimator, with the detector facing towards the focus of the circle of rotation. Custom-made Al collimators (lined with PTFE to absorb all fluorescence of the Al, and of two different central open diameters, 8 mm and 20 mm) were used to collimate the X-ray emissions from the tube when condition measurements with the LD Didactic X-ray apparatus.

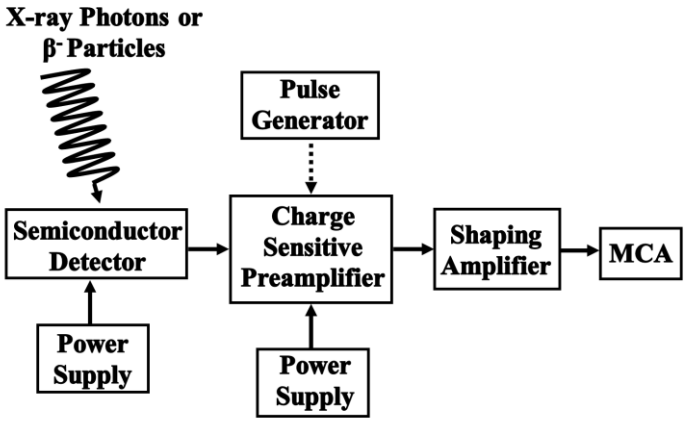

Figure 2.3. Block diagram of the spectrometer system.

Chapter 3 Soft X-ray Detection with Commercial 4H-SiC UV Photodiodes

3.1 Introduction

The performance of SiC photodiode X-ray detectors has been investigated extensively over the past 15 years; high energy resolutions (*Full Width at Half Maximum*) have been achieved with SiC photodiode X-ray detectors, across a wide range of temperatures e.g. *FWHM* at 5.9 keV of 196 eV and 233 eV, at 30 °C and 100 °C, respectively (Bertuccio et al., 2011). Nevertheless, such detectors are still very specialist items not available to all researchers or those who wish to implement such technologies either on low cost space missions or for terrestrial purposes. However, SiC UV photodiodes have been readily commercially available from standard electronic component retailers for some years, if these devices could be repurposing as low cost SiC X-ray detectors they may find use in such applications, even if their performance was not as good as custom detectors.

In this chapter, the results of the electrical characterisation and X-ray detection measurements of two different active area (0.06 mm^2 and 0.5 mm^2) commercial 4H-SiC p-n UV photodiodes at room temperature are presented (see **Sections 3.2** and **3.3**). One of the 0.06 mm^2 photodiodes and one of the 0.5 mm^2 photodiodes were selected for further electrical characterisation and then investigated for its response to illumination with soft X-rays when operated at high temperature (see **Sections 3.4** and **3.5**).

3.2 Electrical characterisation at room temperature

3.2.1 Capacitance-voltage measurements

The capacitances of all four 4H-SiC photodiodes were measured as functions of applied reverse bias at room temperature (24 °C) up to 150 V in 1 V steps using an HP 4275A Multi Frequency LCR meter and a Keithley 6487 Picoammeter/Voltage Source as the external voltage supply (see **Section 2.9**). The AC test voltage signal magnitude and frequency of the LCR meter were set at 60 mV rms and 1 MHz, respectively. National Instruments Labview software was used to automate the capacitance measurements. In order to extract the capacitances of the photodiodes themselves, the bond wires of sacrificial devices of the same type were removed to measure

packaging capacitances. The capacitance of each photodiode was calculated by subtracting the capacitances of packages (0.67 pF ± 0.07 pF for the 0.06 mm^2 photodiodes and 0.65 pF ± 0.07 pF for 0.5 mm^2 photodiodes) from the total capacitances of the packaged devices. The measured capacitances and the calculated depletion width of each photodiode as functions of applied reverse bias are shown in **Figures 3.1** and **3.2**, respectively. The photodiodes were fully depleted at an applied reverse bias of 120 V and 150 V for the 0.06 mm^2 and 0.5 mm^2 devices, respectively. The thickness of the depletion widths of the 0.06 mm^2 and 0.5 mm^2 photodiodes were determined to be 2.5 µm ± 0.04 µm and 4.5 µm ± 0.03 µm at 150 V reverse bias, respectively. The uncertainties associated with the calculated depletion widths were computed taking into account the uncertainties in the capacitance measurements and the Debye length. In comparison to other previously reported wide bandgap X-ray detectors, they are thinner than previously reported custom GaAs X-ray detectors (7 µm) (Lioliou et al., 2016a) and custom SiC X-ray detectors (25 µm) (Bertuccio et al., 2011) but comparable to custom AlGaAs X-ray detectors (1.7 µm) (Barnett et al., 2015).

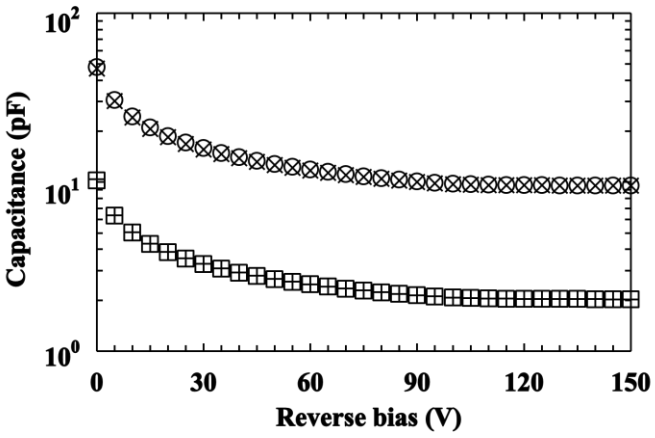

Figure 3.1. Measured capacitances of two 0.06 mm^2 (+ symbols and open squares) and two 0.5 mm^2 (× symbols and open circles) photodiodes as functions of applied reverse bias.

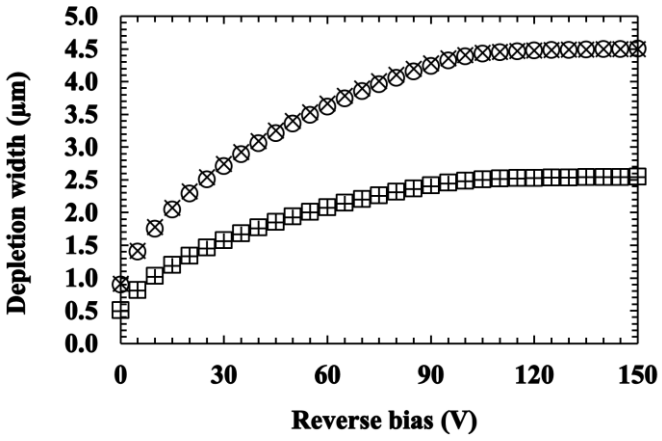

Figure 3.2. Calculated depletion widths of the 0.06 mm^2 (+ symbols and open squares) and 0.5 mm^2 (× symbols and open circles) photodiodes as functions of applied reverse bias.

Assuming the efficiency of these photodiodes is determined by the absorption in the depletion width, their efficiencies can be estimated from **Equation 2.9**. **Figure 3.3** shows the quantum efficiency for these photodiodes at their maximum depletion widths (150 V reverse bias) at X-ray energies up to 10 keV. The quantum efficiencies of the devices at 5.9 keV ($\mu_{5.9keV}$ = 348 cm^{-1}; $\mu_{6.49keV}$ = 263 cm^{-1} (Cromer & Liberman, 1970)) were 0.085 and 0.145, for the 0.06 mm^2 and 0.5 mm^2 photodiodes, respectively.

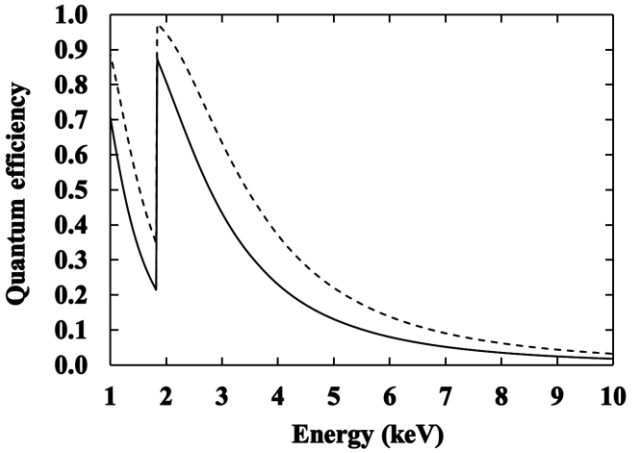

Figure 3.3. The calculated quantum efficiencies of the 4H-SiC 0.06 mm^2 photodiodes depletion layer thickness = 2.5 μm (solid line), and 0.5 mm^2 photodiodes depletion layer thickness = 4.5 μm (dash line) at 150 V reverse bias with varying X-ray energy. The discontinuity at 1.8 keV is the Si K absorption edge.

3.2.2 Current-voltage measurements

The leakage currents of the four photodiodes were measured as functions of applied reverse bias from 0 V to 100 V at room temperature (24 °C) with 1 V per step using a Keithley 6487 Picoammeter/Voltage Source (see **Section 2.8**). The results are presented in **Figure 3.4**. National Instruments Labview software was used to automate the measurements. The photodiodes had low leakage currents (< 10 pA) at high reverse bias (corresponding to leakage current densities of 937 pA/cm^2 and 347 pA/cm^2 at electric fields of 403 kV/cm for the 0.06 mm^2 photodiodes; and 1.4 nA/cm^2 and 1.18 nA/cm^2 at electric fields of 227 kV/cm for the 0.5 mm^2 photodiodes). These are greater than some previously reported SiC X-ray detectors (1 pA/cm^2 with mean electric fields of 53 and 103 kV/cm at room temperature) (Bertuccio et al., 2011), but better than semi-insulating SiC X-ray photodiodes (from 2.6 nA/cm^2 to 65 nA/cm^2 with internal electric fields from 7 kV/cm to 28 kV/cm) (Bertuccio et al., 2013b) and GaAs X-ray photodiodes (e.g. 17.4 nA/cm^2 with internal electric field 22 kV/cm) (Lioliou et al., 2016a).

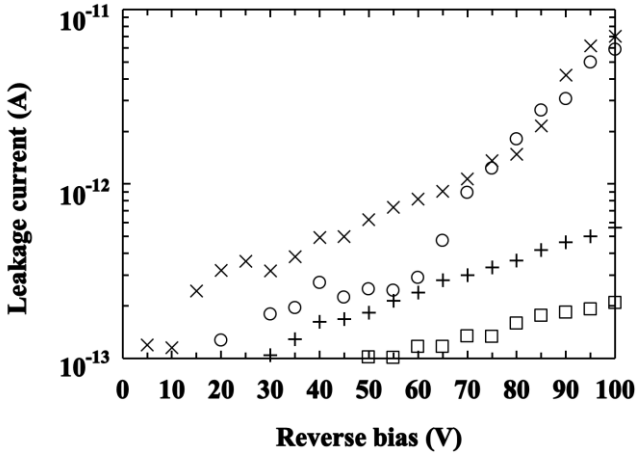

Figure 3.4. Leakage currents as functions of applied bias for the 0.06 mm^2 (+ symbols and open squares) and 0.5 mm^2 (× symbols and open circles) photodiodes.

3.3 X-ray detection at room temperature

3.3.1 Current mode X-ray detection

In order to characterise the response of the diodes to illumination with soft X-rays, an ^{55}Fe radioisotope X-ray source (Mn Kα = 5.9 keV; Mn Kβ = 6.49 keV; activity = 260 MBq; active area = 28.27 mm^2) was placed 2 mm above the photodiodes (see **Section 2.8**). The reverse bias was increased from 0 V to 100 V in 1 V steps. The measured photocurrent (the current measured

with the devices illuminated with the previously measured leakage current subtracted) are presented for the 0.06 mm^2 and 0.5 mm^2 devices in **Figure 3.5**.

Given the quantum efficiencies of the devices computed from the calculated depletion widths at 100 V reverse bias (2.48 μm and 4.4 μm, for the 0.06 mm^2 and 0.5 mm^2 devices, respectively), the activity geometry of the ^{55}Fe radioisotope X-ray source, and the relative emission probabilities (Mn Kα 5.9 keV = 0.245; Mn Kβ = 6.49 keV = 0.0338 (Schötzig, 2000)), using **Equation 2.6**, the calculated expected photocurrents at 100 V reverse bias of 0.06 mm^2 photodiodes (0.44 pA) and 0.5 mm^2 photodiodes (6.3 pA), assuming only charge created in the depletion width contributed to the signal and 100% charge collection efficiency (Sze, 1985), were much smaller than the measured photocurrents of the 0.06 mm^2 photodiodes (4.6 pA) and 0.5 mm^2 photodiodes (18 pA) at 100 V reverse bias. The greater than expected photocurrent suggests that there may have been significant contributions to the signal from charge created outside of the depletion region by photons absorbed there. Furthermore, one 0.5 mm^2 photodiode showed an exponential trend in photocurrent at reverse biases > 60 V indicative of avalanche multiplication even though the electric field strength, assuming a uniform electric field across the depletion layer, was lower than that at which significant impact ionisation has been previously observed to occur (Loh et al., 2008). It was hypothesised that this may have been due to defects in the material of the detector leading to localised regions of high electric field strength.

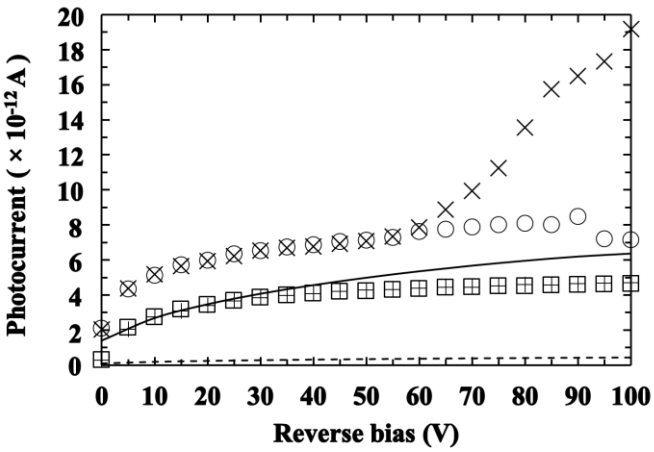

Figure 3.5. Photocurrent as a function of applied reverse bias for the 0.06 mm^2 (+ symbols and open squares) and 0.5 mm^2 (× symbols and open circles) photodiodes. Expected photocurrent for the 0.06 mm^2 photodiodes (dash line) and 0.5 mm^2 photodiodes (solid line).

3.3.2 X-ray spectroscopy and noise analysis

3.3.2.1 Photon counting spectroscopy with an ^{55}Fe radioisotope X-ray source

The photodiodes were each in turn connected to a custom-made low-noise charge-sensitive preamplifier with a 2N4416A silicon input JFET (capacitance = 2 pF). An ORTEC 572A shaping amplifier and a multi-channel analyser (MCA) were connected to the preamplifier (see **Section 2.11**). Spectra were accumulated using the ^{55}Fe radioisotope X-ray source. The ^{55}Fe radioisotope X-ray source was placed 2 mm above the photodiodes. Spectra were accumulated at reverse biases from 0 V to 100 V in 10 V steps. The temperature of the detector and preamplifier was 22 °C. The live time limit for each spectrum was 60 s.

Because of the large capacitances and low leakage currents of these devices, the longest shaping time available (10 µs) was selected (Bertuccio et al., 1996) (Barnett et al., 2012). The resulting spectra were calibrated in energy terms by using the position of the zero energy noise peak and the position of the fitted Mn Kα at 5.9 keV for each spectrum as points of known energy on MCA's charge scale and assuming a linear variation of detected charge with energy. The energy resolution of the devices as quantified by the full width at half maximum (*FWHM*) of the 5.9 keV peak is presented in **Figure 3.6** as a function of applied reverse bias. A photopeak could not be resolved with the 0.5 mm^2 photodiodes at reverse biases below 50 V due to the large capacitance of the devices. For both sizes of device (0.06 mm^2 and 0.5 mm^2) the best energy resolutions, 1.8 keV *FWHM* and 3.3 keV *FWHM*, were obtained at the maximum investigated reverse bias (100 V). The ^{55}Fe X-ray spectrum obtained at 100 V with one of the 0.06 mm^2 photodiodes is presented in **Figure 3.7**; two Gaussians were fitted to the observed photopeak to represent the Mn Kα (5.9 keV) and Mn Kβ (6.49 keV) emissions from the radioisotope X-ray source in the accepted ratio (Schötzig, 2000). The MCA's low energy threshold was set at 2.85 keV as a compromise between minimising the number of noise counts from the tails of the zero energy noise peak and maintaining the low energy response of the spectrometer. The energy resolutions at 5.9 keV were not as good as some wide bandgap devices specifically designed for X-ray detection e.g. GaAs mesa photodiodes (840 eV, area of 0.03 mm^2; and 1.07 keV, area of 0.13 mm^2) (Barnett, 2014), AlGaAs X-ray detectors (1.1 keV, area of 0.03 mm^2 (Barnett et al., 2010); and 1.27 keV, area of 0.13 mm^2 (Barnett et al., 2015)), and the best result of SiC X-ray detectors (196 eV at 30 °C, area of 0.4 mm^2) (Bertuccio et al., 2011). However, the *FWHM* of the 0.06 mm^2 area diode was better than some larger area AlGaAs photodiodes (0.13 mm^2) (1.95 keV) (Barnett et al., 2013a).

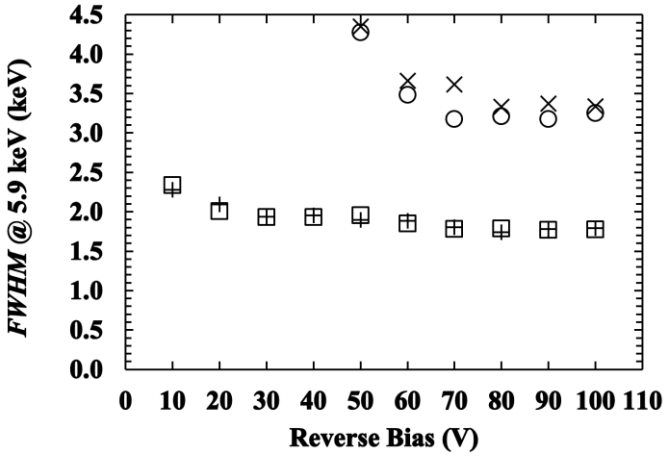

Figure 3.6. Measured *FWHM* at 5.9 keV of 0.06 mm^2 (+ symbols and open squares) and 0.5 mm^2 (× symbols and open circles) photodiodes as functions of applied reverse bias.

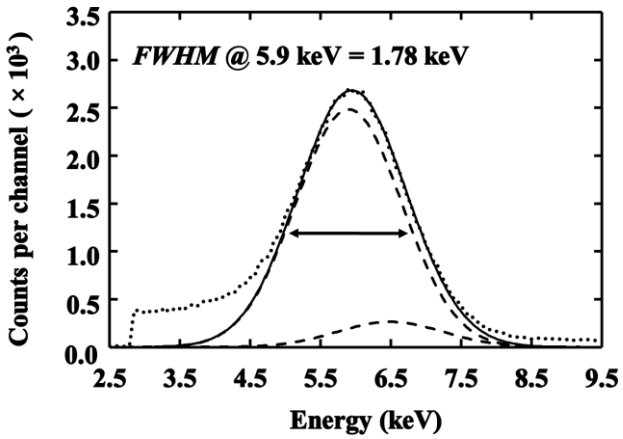

Figure 3.7. ^{55}Fe X-ray spectrum obtained one of the 0.06 mm^2 photodiodes at 100 V reverse bias. The dashed lines are the fitted Mn Kα and Kβ peaks.

3.3.2.2 Noise analysis

The fundamental 'Fano-limited' energy resolution ($FWHM_{Fano}$) of a non-avalanche photodiode is given by **Equation 2.12**. However, the energy resolution of a photodiode spectrometer is further influenced by noise from incomplete charge collection and electronic noise from the connection of the detector to the preamplifier, such that as the electronic noise arises not only from the shot noise of the detector but also the noise from the amplification system as described in **Equation 2.13**.

The expected Fano limited energy resolution, $FWHM_{Fano}$ in SiC is 160 eV *FWHM* at 5.9 keV (Bertuccio et al., 2011). Therefore, it is essential to consider the other noise sources contributing to the measured energy resolution of the system. The electronic noise of this system consists of

five contributors: series white noise, parallel white noise, 1/*f* series noise, dielectric noise and the induced gate drain current noise. A detailed explanation of the origin of each electronic contributors can be found in **Section 2.7**. The total electronic noise contribution was measured for the system with the 0.06 mm^2 devices by injecting a delta test pulse signal into the preamplifier with the detector connected but unilluminated (American National standards Institute, 1976) (Bertuccio et al., 1996) (Barnett et al., 2012).

The dielectric noise (and series white noise from unknown stray capacitances (Barnett et al., 2015)) can be calculated by the subtraction of the calculated series white noise including induced gate drain current noise, parallel white noise, and 1/*f* series noise in quadrature from the measured total electronic noise (Lioliou & Barnett, 2015). The other noise components were calculated as per **Section 2.7**. The calculated electronic noise components are presented as a function of reverse bias in **Figure 3.8**. As is the case for other detectors connected to similar charge-sensitive preamplifiers, the dielectric noise (and noise from stray capacitances) is the most significant noise component (Barnett et al., 2015) (Lioliou & Barnett, 2015). Such noise is thought to arise from dielectric materials of the capacitances and packages (Bertuccio et al., 1996). The presently reported preamplifier used a wire-end input JFET for convenience; a bare die JFET directly wire-bonded to the detector would be expected to significantly reduce the noise. If this noise could be eliminated entirely, an energy resolution (*FWHM* at 5.9 keV) of 1.1 keV could be achieved with the 0.06 mm^2 photodiode.

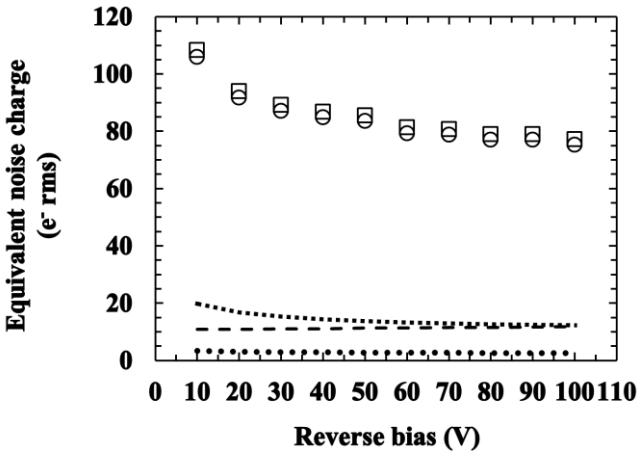

Figure 3.8. Calculated electronic noise contributions for one 0.06 mm^2 photodiode, connected to the custom low-noise charge-sensitive preamplifier, at varied reverse bias. Measured electronic noise (open squares), computed dielectric noise and series white noise from unknown stray capacitances (open circles), series white noise including induced gate current noise (square dot line), parallel white noise (dash line), and 1/*f* series noise (round dot line).

Incomplete charge collection noise is related to the detector's charge diffusion and collection properties as well as to the trap density distribution in the detector (Owens, 2012). In this system, the incomplete charge collection noise can be calculated by subtracting in quadrature the predicted Fano noise and the total electronic noise from the measured energy resolution at 5.9 keV. The calculated contributions from incomplete charge collection for the 0.06 mm^2 photodiode are shown in **Figure 3.9**. Interestingly, the incomplete charge collection noise was independent of applied electric field. This supports the hypothesis introduced in **Section 3.3.1** to explain the greater than expected photocurrent that significant amounts of charge created outside of the depletion region (by photons absorbed in those positions) contributed to the detected signal. Since the applied bias mainly resulted in an electric field across the epilayer/depletion region, the field strength in the volume below the depletion region remained low, regardless of applied bias. Thus the incomplete charge collection noise, which probably arose from recombination of electrons and holes in the low field region remained constant. The data and explanation are consistent high quality material close to top contact exhibiting comparatively little charge trapping and a volume of material with consistently low electric field strength below it showing moderate amounts (≈ 58 e^- rms equivalent noise charge) of incomplete charge collection noise.

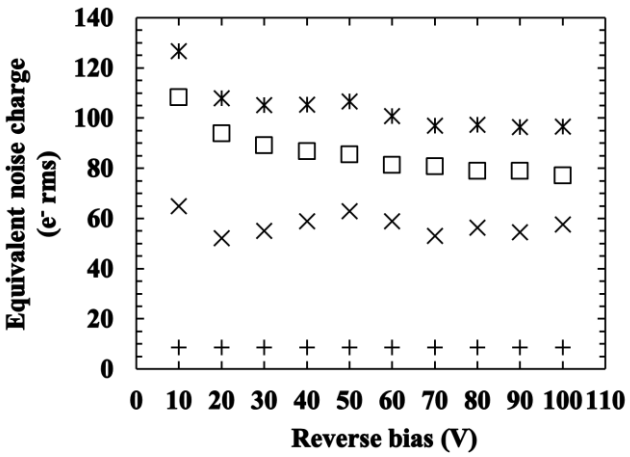

Figure 3.9. Computed noise contributions of one of the 0.06 mm^2 photodiodes at varied reverse bias. Total *FWHM* measured at 5.9 keV (stars), electronic noise (open squares), incomplete charge collection noise (× symbols), and the Fano noise (+ symbols).

3.4 Electrical characterisation at high temperatures

3.4.1 Capacitance-voltage measurements

The capacitance of one of the 0.06 mm^2 photodiodes and one of the 0.5 mm^2 photodiodes were

measured as functions of applied reverse bias across the temperature range 0 °C to 140 °C. In turn, each photodiode was installed in a TAS Micro MT climatic cabinet for temperature control. The capacitance measurements were made using an HP 4275A Multi Frequency LCR meter with an AC test signal of 60 mV rms magnitude and 1 MHz frequency; a Keithley 6487 Picoammeter/Voltage source was used as the external voltage supply. Measurements of the devices' capacitances as functions of temperature were made from 140 °C to 0 °C, with a decrement step size of 20 °C. To ensure thermal equilibrium, the devices were allowed to stabilise at each temperature for 30 min before measurements were started at each temperature (see **Section 2.9**). The devices were reverse biased from 0 V to 120 V, in 1 V increments. National Instruments Labview software was used to automate the measurements.

The capacitances of the packages with the dice still mounted in each package, but the bond wires removed, were measured across the temperature range using the same procedure as was outlined above. The capacitances of the packages were independent of applied bias but dependent on temperature. The results are presented in **Figure 3.10**.

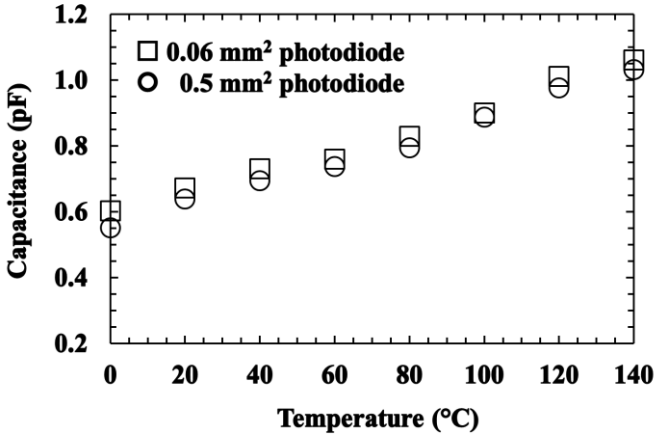

Figure 3.10. Measured capacitances of the detectors' packages as functions of temperature for the 0.06 mm^2 photodiode (open squares) and 0.5 mm^2 photodiode (open circles).

To determine the capacitances of the photodiodes themselves, the package capacitances (presented in **Figure 3.10**) were subtracted from the capacitances measured with the photodiodes wire-bonded. The device capacitances as subsequently determined, and the depletion width of each diode implied by those capacitances are shown in **Figure 3.11**, for the 0.06 mm^2 and the 0.5 mm^2 photodiodes at the temperature of 20 °C and 100 °C, respectively. **Figure 3.11** showed the 0.06 mm^2 photodiode was fully depleted (2.30 μm ± 0.04 μm) at more than 90 V reverse bias and the 0.5 mm^2 photodiode has been fully depleted (4.49 μm ± 0.03 μm) at the reverse bias of more than 110 V. The uncertainties associated with the calculated depletion widths were

computed taking into account the uncertainties in the capacitance measurements and the Debye length. Two contributors can explain the recorded increases in the capacitances of these devices with increased temperature. One is an increase in charge density in the depletion layer with increased temperature; a similar effect was previously found in abrupt p^+-n diodes and attributed to an effect where the trap density with an energy level near the centre of the bandgap contributed to a measured increase in capacitance with temperature. Thus, there may have been an increase in the excess donor concentration with temperature, with the capacitance of the device at each temperature (see **Equation 2.2**). The other contributor is the progressive ionisation of previously non-ionised donors in a thin region around the depletion layer with increasing temperature (Mazzillo et al., 2012).

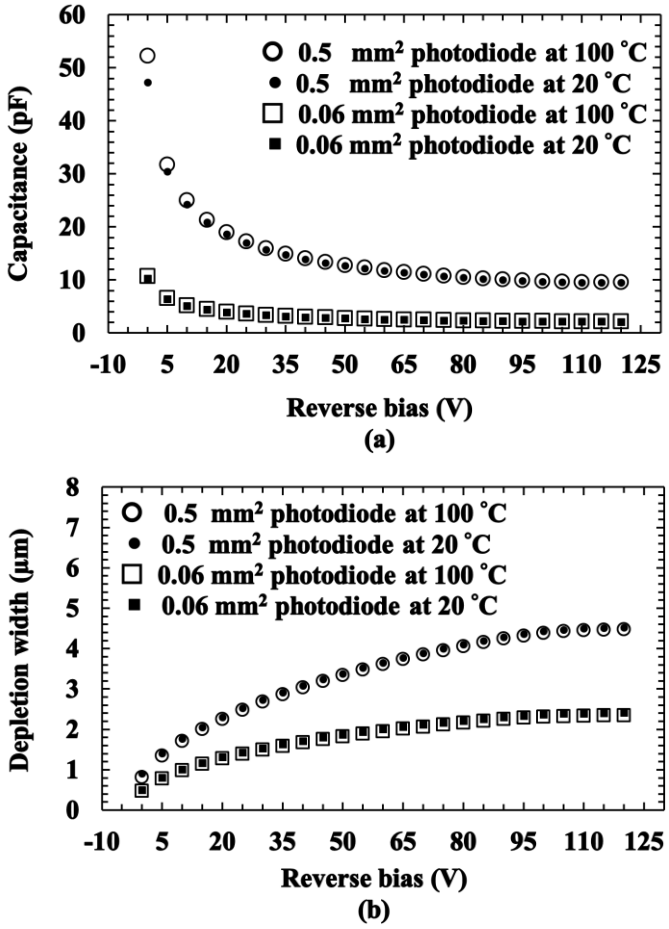

Figure 3.11. (a) Measured capacitances of 0.5 mm^2 (open circles 100 °C and solid circles 20 °C) and 0.06 mm^2 (open squares 100 °C and solid squares 20 °C) photodiode as functions of applied reverse bias. (b) Calculated depletion width of 0.5 mm^2 (open circles 100 °C and solid circles 20 °C) and 0.06 mm^2 (open squares 100 °C and solid squares 20 °C) photodiode as functions of applied reverse bias.

The temperature dependence of each diode's capacitance and depletion width became less

significant at high reverse biases (> 20 V), as shown in **Figures 3.12** and **3.13**. This may be explained by the lower the ratio between the thickness of the thin region near the depletion layer with non-ionised donors, and the thickness of the depletion layer at high reverse biases (Mazzillo et al., 2012). The capacitance temperature coefficient (from 0 °C to 140 °C) was found to be 0.3 $fF \cdot °C^{-1}$ and 0.1 $fF \cdot °C^{-1}$ for the 0.06 mm^2 photodiode and the 0.5 mm^2 photodiode by the measured capacitances at 120 V reverse bias. The thicknesses of the depletion widths of the 0.06 mm^2 and 0.5 mm^2 photodiodes were found to be 2.34 µm ± 0.04 µm and 4.47 µm ± 0.03 µm, respectively, both at 120 V reverse bias and 140 °C.

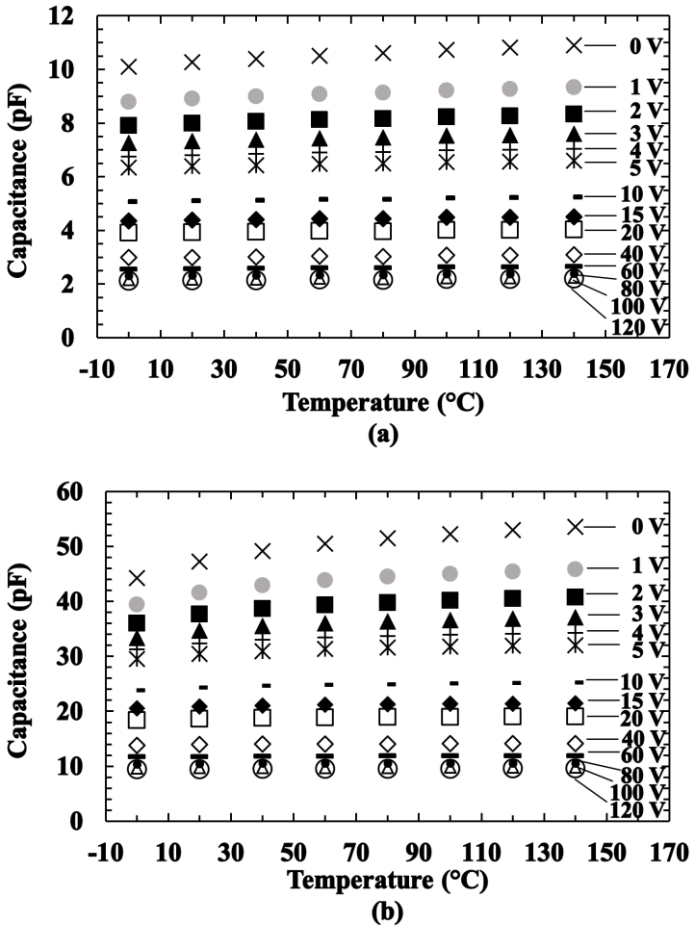

Figure 3.12. Capacitance as a function of temperature for (a) the 0.06 mm^2 photodiode and (b) the 0.5 mm^2 photodiode in the temperature range of 0 °C to 140 °C at varying reverse biases, 0 V (× symbols), 1 V (grey circles), 2 V (dark squares), 3 V (dark triangles), 4 V (+ symbols), 5 V (stars), 10 V (short dashes), 15 V (dark diamonds), 20 V (open squares), 40 V (open diamonds), 60 V (dashes), 80 V (black circles), 100 V (open triangles), 120 V (open circles).

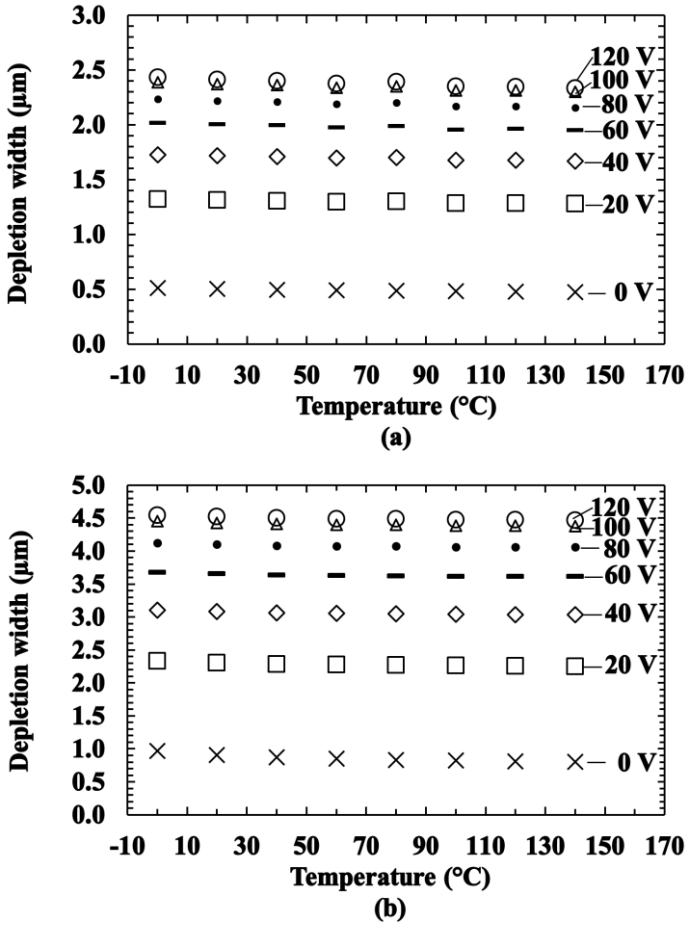

Figure 3.13. Calculated depletion width as a function of temperature for (a) 0.06 mm^2 photodiode and (b) 0.5 mm^2 photodiode in the temperature range of 0 °C to 140 °C at seven reverse biases 0 V (× symbols), 20 V (open squares), 40 V (open diamonds), 60 V (dashes), 80 V (dark circles), 100 V (open triangles), 120 V (open circles).

3.4.2 Current-voltage measurements

The ultra-low leakage currents of SiC junctions are one of key beneficial features of SiC detectors (Bertuccio et al., 2006). The leakage currents of the two photodiodes were measured each in turn as functions of applied reverse bias from 0 V to 120 V in 1 V increments, at temperatures from 140 °C to 40 °C, in steps of 20 °C. The devices were installed in a TAS Micro MT climatic cabinet for temperature control. A Keithley 6487 Picoammeter/Voltage Source was used to bias the devices. National Instruments Labview software was used to automate the measurements. To ensure thermal equilibrium, each device was allowed 30 min to stabilise at each temperature before measurements began (see **Section 2.8**).

The results showed that the dark current was increased at high temperatures for all applied bias, as shown in **Figure 3.14**. The dark currents of both devices at the same reverse bias and

temperature were similar because the packages of the diodes (rather than the semiconductor junctions) are the dominant source of leakage current in the system. The dark currents of the 0.06 mm^2 photodiode and the 0.5 mm^2 photodiode at 120 V reverse bias were both found to be 0.2 pA ± 0.4 pA at 40 °C, and 1.454 nA ± 0.005 nA and 1.537 nA ± 0.005 nA, respectively, at 140 °C. At temperatures < 40 °C, the leakage currents of the devices were too small to measure with the experimental apparatus used. It is interesting to compare the high temperature leakage currents of the present devices with high-quality custom-made X-ray photodiodes. The leakage current densities of the 0.06 mm^2 and 0.5 mm^2 photodiodes at 100 °C were 7.9 nA/cm^2 ± 0.7 nA/cm^2 and 2.6 nA/cm^2 ± 0.1 nA/cm^2, respectively, at applied electric fields of 101 kV/cm. These are comparable to previously reported custom-made SiC X-ray detectors of high quality (e.g. 1 nA/cm^2 with mean electric field of 103 kV/cm at 107 °C (Bertuccio et al., 2011)), and better than some custom-made GaAs X-ray photodiodes at 100 °C (e.g. 20 $\mu A/cm^2$ with an electric field of 21.4 kV/cm (Lioliou et al., 2016b)).

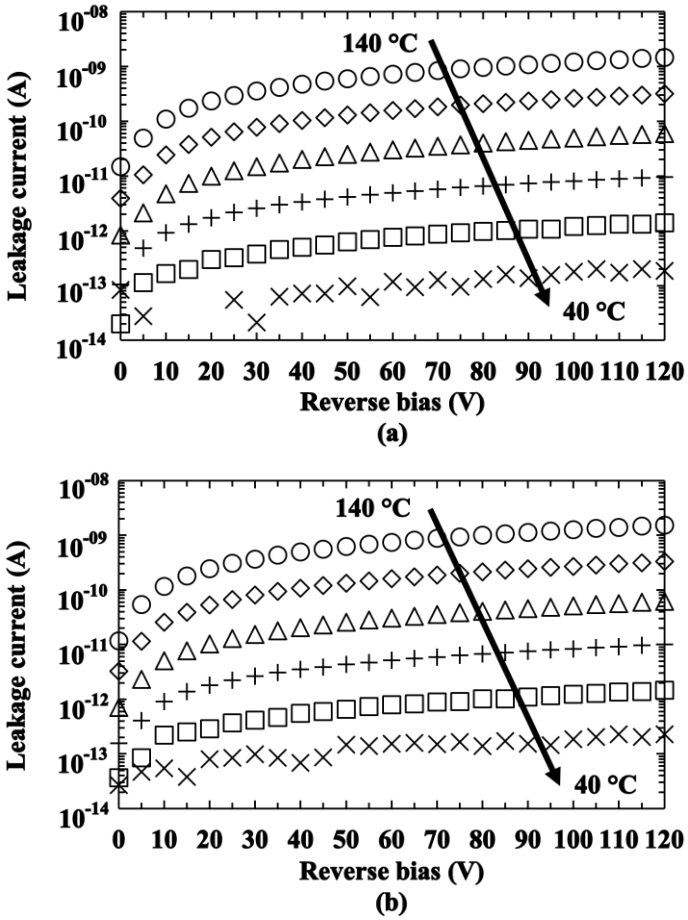

Figure 3.14. Leakage current as a function of temperature for (a) 0.06 mm^2 photodiode and (b) 0.5 mm^2 photodiode in the range of 40 °C to 140 °C at varying reverse biases.

3.5 X-ray detection at high temperatures

3.5.1 Current mode X-ray detection

An ^{55}Fe radioisotope X-ray source (Mn Kα = 5.9 keV; Mn Kβ = 6.49 keV; activity = 231 MBq; active area = 28.27 mm^2) was placed 2 mm above the photodiodes to investigate the soft X-ray response of the photodiodes at varying temperatures (see **Section 2.8**). The measured photocurrents (the illuminated current with the previously measured dark current subtracted) as functions of applied reverse bias for the 0.06 mm^2 and 0.5 mm^2 devices are presented in **Figure 3.15**, at temperatures from 40 °C to 80 °C. At temperatures above 80 °C, the photocurrents of both devices could not be measured due to the high dark currents of the devices at temperatures > 80 °C relative to the comparatively small photocurrent, and the sensitivity of the Keithley 6487 Picoammeter/Voltage Source. The photocurrents of the 0.06 mm^2 photodiode and the 0.5 mm^2 photodiodes were found to be 4.2 pA ± 0.2 pA and 28.4 pA ± 1.3 pA at 80 °C and 120 V reverse bias, respectively.

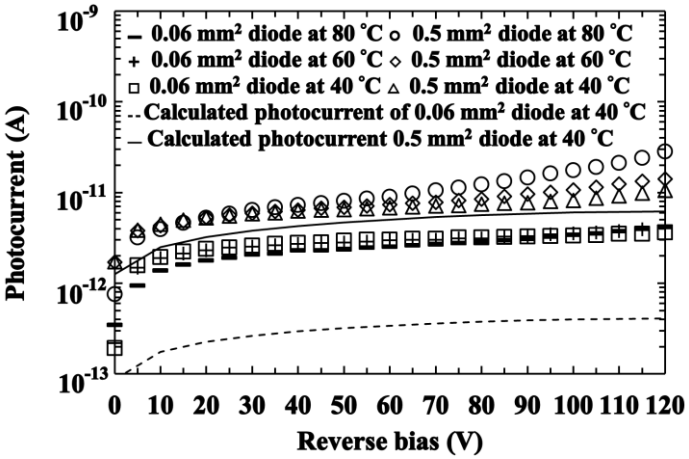

Figure 3.15. Photocurrent as a function of applied reverse bias for the 0.06 mm^2 (80 °C, open squares; 60 °C, + symbols; 40 °C, dashes) and 0.5 mm^2 (80 °C, open circles; 60 °C, open diamonds; 40 °C, open triangles) photodiode. Expected photocurrents for the 0.06 mm^2 photodiode (dash line), and 0.5 mm^2 photodiode (solid line) at 40 °C.

In order to calculate the expected photocurrents for these photodiodes, assuming an electron-hole pair creation energy for 4H-SiC = 7.8 eV (Bertuccio & Casiraghi, 2003), and given the quantum efficiencies of the devices computed from the calculated depletion widths at 120 V reverse bias (2.4 µm for 0.06 mm^2 photodiode; 4.5 µm for 0.5 mm^2 photodiode) at 40 °C, as well as the activity geometry of the ^{55}Fe radioisotope X-ray source, and its relative X-ray emission probabilities (Mn Kα 5.9 keV = 0.245; Mn Kβ 6.49 keV = 0.0338 (Schötzig, 2000)), by using

Equation 2.6, the calculated expected photocurrents at 120 V reverse bias of the 0.06 mm^2 photodiode and 0.5 mm^2 photodiode were 0.41 pA and 6.17 pA, respectively. These values assume that only charge created in the depletion region contributed to the signal and that there was 100 % charge collection efficiency (Sze, 1985) (Nava et al., 2008).

Interestingly, the expected photocurrents were much smaller than the measured photocurrents of the 0.06 mm^2 photodiode and 0.5 mm^2 photodiode at 120 V and 40 °C. The largest measured photocurrents of the 0.06 mm^2 photodiode 4.23 pA ± 0.41 pA and 0.5 mm^2 photodiode 28.41 pA ± 0.49 pA were obtained at 120 V reverse bias and 80 °C.

The apparent greater than expected photocurrents are possibly due to several factors. Firstly, contribution from electron-hole pairs generated around the edge of the depletion region leading to collection of charge carriers from a greater volume than assumed will have augmented the signal (i.e. at least some carriers generated outside of the depletion region contributed to the detected signal). If this was the sole influencing effect, the detected photocurrents imply that the active thicknesses of the detectors were 8.1 µm for the 0.5 mm^2 photodiode (i.e. 3.6 µm beyond the depletion region, which is conceivable), and 34.5 µm for the 0.06 mm^2 photodiode (which is too large to be reasonable). Secondly, there may also have been some contribution from impact ionisation (Loh et al., 2008); however, it should be noted that the devices were operated at a lower electric field strength (0.5 MV/cm, assuming a uniform field across the depletion layer) than that at which avalanche multiplication in 4H-SiC has been previously reported to start to play a role in current generation (0.9 MV/cm (Loh et al., 2008)). Thus, it is hypothesized that if there was impact ionisation, it would have been due to localised material defects in the detector leading to localised regions of high electric field strength, rather than multiplication across the whole of the depletion layer. The electric field-dependence of the photocurrent of the 0.5 mm^2 photodiode became significant at high reverse bias (> 60 V) which is consistent with increased avalanche multiplication, which is also field-dependent. However, the effects were found to be more significant at higher temperatures. Since the temperature dependences of the impact ionisation coefficients have previously been reported to be such that avalanche multiplication is reduced at higher temperatures as a result of increased phonon scattering (Raghunathan & Baliga, 1999) (Niwa et al., 2014), if an explanation of a contribution from impact ionisation is correct, the mechanism or mechanisms causing the increased localised high electric field strength would have implied a stronger positive temperature coefficient than the negative temperature coefficient of the impact ionisation coefficients. Thus, the exact nature of any contribution from impact ionisation, if there was any, is still to be determined. A third explanation for the increasing photocurrent seen at high temperatures and reverse biases may be that under these conditions, the electron-hole pairs created by the X-ray photons increased the conductivity of the material such

that a greater current from the bias supply could flow as a result of that decreased resistivity; this is thought to be unlikely given the relatively small amount of charge being created in the detectors by the X-ray photons per unit time. A final alternative explanation, is that the leakage current of the detectors may have been increased (relative to the prior leakage current measurements) if the detectors were disturbed when the ^{55}Fe radioisotope X-ray source was positioned above each of them. However, the utmost care was taken to avoid such disturbance. Use of a chopper wheel and lock-in amplifier may have enabled this influence to be quantified or discounted, but our laboratory does not have such equipment at present.

3.5.2 X-ray spectroscopy and noise analysis

3.5.2.1 Photon counting spectroscopy with an ^{55}Fe radioisotope X-ray source

The 0.06 mm^2 photodiode was connected to a custom-made low-noise charge-sensitive preamplifier with a wire-ended packaged 2N4416A silicon input JFET (capacitance = 2 pF) and installed in a TAS Micro MT climatic cabinet for temperature control. The leg of the detector was directly soldered to the gate leg of the packaged JFET. An ORTEC 572A shaping amplifier and an ORTEC EASY-MCA 8k multi-channel analyser (MCA) were connected to the preamplifier (see **Section 2.11**). The photodiode was illuminated with the ^{55}Fe radioisotope X-ray source, which was placed 2 mm above the photodiode. The system was investigated at different shaping times (0.5 μs, 1 μs, 2 μs, 3 μs, 6 μs, and 10 μs) at each temperature (from 100 °C to 0 °C, with 20 °C steps) with the photodiode reverse biased at 100 V. Each spectrum had a live time limit of 60 s. The resulting spectra were calibrated in energy terms by using the position of the zero energy noise peak and the position of the fitted Kα at 5.9 keV for each spectrum as points of known energy on MCA's charge scale and assuming a linear variation of detected charge with energy. The energy resolution of the system at temperatures from 100 °C to 0 °C as quantified by the full width at half maximum (*FWHM*) of the 5.9 keV peak as functions of shaping time is shown in **Figure 3.16**.

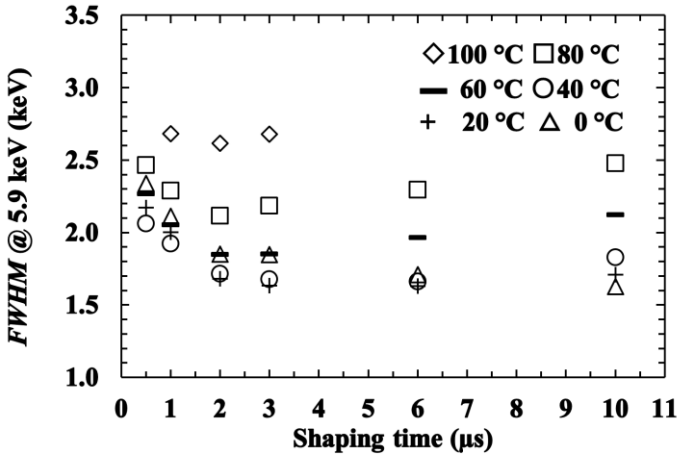

Figure 3.16. Measured *FWHM* at 5.9 keV of the system as functions of applied shaping time at 100 V reverse bias.

At 100 °C, the photopeak could not be resolved from the zero energy noise peak at shaping times longer than 3 μs due to the large leakage current of the device (50 pA). At this temperature, the photopeak was also unresolved from the zero energy noise peak at a shaping time of 0.5 μs, due to the capacitance of the detector. However, a photopeak was resolved with the system at this temperature for shaping times of 1 μs (*FWHM* = 2.68 keV), 2 μs (*FWHM* = 2.62 keV), and 3 μs (*FWHM* = 2.68 keV). The best energy resolution achieved with the system at each temperature is shown in **Figure 3.17**. The energy resolutions at 5.9 keV at high temperature were not as good as some wide bandgap devices specifically designed for X-ray detection, e.g. GaAs mesa photodiodes (1.5 keV at 80 °C, area of 0.03 mm^2 (Barnett et al., 2011); 840 eV at 60 °C, area of 0.03 mm^2 (Lioliou et al., 2016b) and the best results obtained with custom-made SiC X-ray detectors (233 eV at 100 °C, area of 0.4 mm^2) (Bertuccio et al., 2011), however, the *FWHM* of the device was comparable to $Al_{0.8}Ga_{0.2}As$ X-ray detectors at 80 °C (2.0 keV, area of 0.03 mm^2) (Barnett et al., 2010). Example spectra obtained with the present system at 0 °C and 60 °C are shown in **Figure 3.18**.

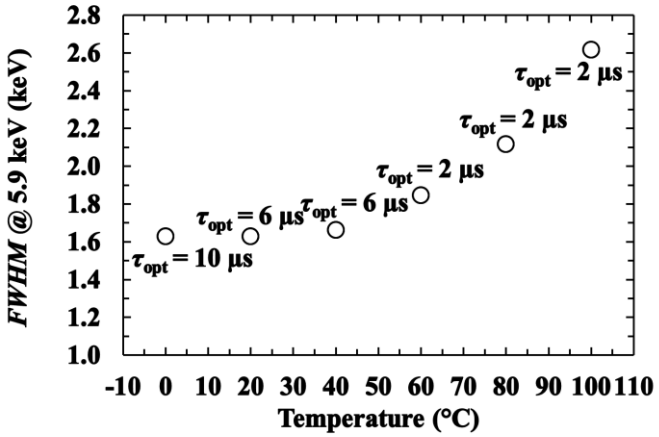

Figure 3.17. The measured best energy resolution of the 0.06 mm^2 photodiode as a function of temperature at 100 V reverse bias. The shaping time which gave the best energy resolution at each temperature, τ_{opt} is indicated.

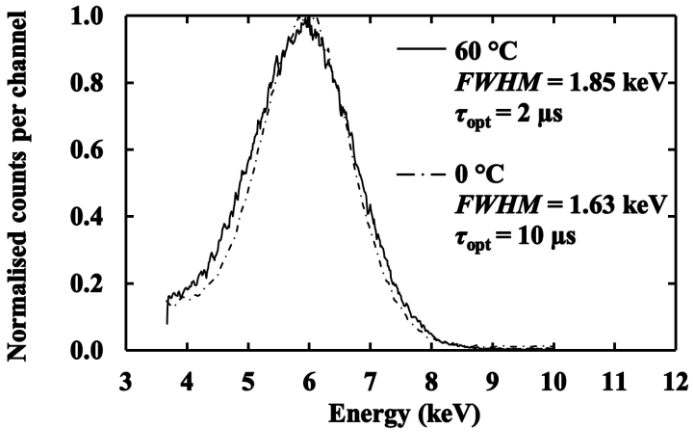

Figure 3.18. ^{55}Fe X-ray spectrum obtained with 0.06 mm^2 photodiode at 100 V reverse bias at 0 °C and 60 °C.

3.5.2.2 Noise analysis

The energy resolution (*FWHM*) of a photodiode X-ray spectrometer is generally limited by the electronic noise of the detector and preamplifier, by the incomplete charge collection noise, and by the Fano noise (Owens, 2012). The Fano noise is determined by the statistical fluctuations in the number of the electron-hole pairs created in the process of photon absorption (Owens, 2012). The expected Fano-limited resolution ($FWHM_{Fano}$) of the devices examined here can be calculated as 160 eV at 5.9 keV, assuming the average energy consumed in the generation an electron-hole pair was 7.8 eV (Bertuccio & Casiraghi, 2003), and the Fano factor was 0.1 (Bertuccio et al., 2011). Clearly, the Fano noise was not the dominant noise contributor in the energy resolution

of the system presented, rather the energy resolution was degraded by other noise sources.

The electronic noise arises from the series white noise including induced gate current noise, parallel white noise, 1/*f* series noise, and the dielectric noise. A detailed explanation of the origin of each electronic noise can be found in Bertuccio & Pullia (1993) and Lioliou & Barnett (2015). The series white noise is proportional to the total capacitance at the preamplifier input (including the capacitances of the photodiode, input JFET of the preamplifier, feedback capacitor, and stray capacitances), it is inversely proportional to the shaping time. The parallel white noise is proportional to the leakage current of the photodiode and the input JFET, and it is proportional to the shaping time. The 1/*f* series noise is proportional to the total capacitance at the preamplifier input (including the capacitances of the photodiode, input JFET of the preamplifier, feedback capacitor, and stray capacitances), it is independent of the shaping time. Using the method given by Bertuccio & Pullia (1993), the capacitance and the leakage current of the input JFET can be estimated across the temperature range. A constant dielectric dissipation factor (dielectric loss tangent) of 4H-SiC (3.4×10^{-5} (Jung et al., 2014)) and Si (0.2×10^{-3} (Lowe & Sareen, 2013)) through the temperature range was assumed (Hartnett et al., 2011) (Jung et al., 2014). According to the estimated the leakage current and the capacitance of the input JFET and the measured leakage current and capacitance of the detector, parts of the electronic noise can be calculated (parallel white noise, series white noise, 1/*f* series noise, and the known (i.e. readily calculable) dielectric noises of the 4H-SiC photodiode and the Si input JFET) at different temperatures. The calculated Fano noise, series white noise including induced gate current noise, parallel white noise and the 1/*f* series noise, the quadratic sum of known dielectric noise of the detector and the input JFET, and the quadratic sum of unknown dielectric noise and incomplete charge collection noise of the system are as shown in **Figure 3.19**.

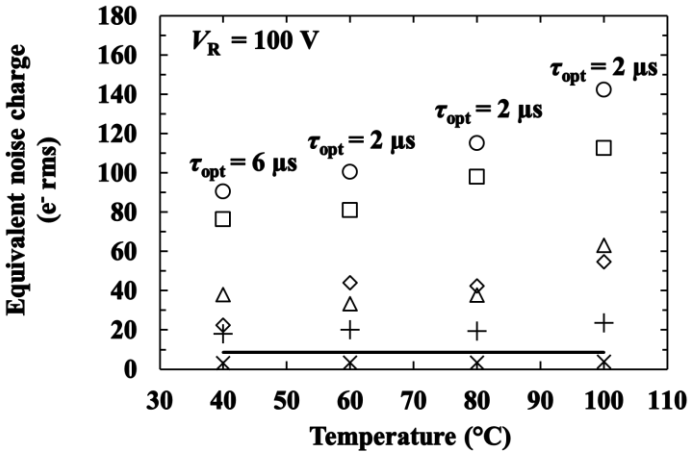

Figure 3.19. Calculated components of noise contribution for the 0.06 mm^2 photodiode connected to the custom low-noise charge-sensitive preamplifier, at the optimal shaping time at each temperature. Measured *FWHM* at 5.9 keV (open circles), computed quadratic sum of known dielectric noise (4H-SiC photodiode and Si input JFET) (+ symbols), computed quadratic sum of unknown dielectric noise and incomplete charge collection noise (open squares), parallel white noise (open triangles), series white noise including induced gate drain current noise (open diamonds), Fano noise (solid line), and 1/*f* series noise (× symbols).

The unknown dielectric noise (and series white noise from unknown stray capacitances (Owens, 2012)) and any possible contribution from the incomplete charge collection noise cannot be directly calculated in this case. However, it is clear that the combined contributions of the unknown dielectric noise, noise from any unknown stray capacitances, and from any incomplete charge collection noise (where incomplete charge collection arises solely from carriers created in the substrate, not the epitaxial layers) are in combination the dominant noise for this system. The dielectric noise (and noise from stray capacitances) is thought to arise from dielectric materials of the capacitances and packages, by using a bare die JFET directly wire-bonded to the detector could be expected to descent the noise significantly (Bertuccio et al., 1996). The incomplete charge collection noise is related to the detector's charge diffusion and collection properties as well as to the trap density distribution in the detector (Owens, 2012).

The variation with temperature of the capacitance and the leakage current of the device in part determines the series white noise, 1/*f* series noise, parallel white noise at each temperature. By changing the shaping time, the optimal energy resolution (within the limits of the range of shaping times available with the shaping amplifier used), that could be achieved at each temperature (Bertuccio et al., 1996) (Barnett et al., 2012) was obtained. As shown in **Figure 3.17**, the longest shaping time (τ = 10 µs) was selected to achieve the optimal energy resolution (*FWHM* at 5.9 keV) at low temperature (< 20 °C) because the leakage current (and hence parallel white noise) was

small compared with the series white noise. On the contrary, shorter shaping times resulted in better energy resolutions at high temperature (> 40 °C) as the leakage current increased and the balance between the parallel white noise and series white noise changed.

3.6 Conclusions and discussion

Measurements characterising four commercial 4H-SiC photodiodes of two different areas (0.06 mm^2 and 0.5 mm^2) as well as the performance of these devices as X-ray detectors operated in a current mode and a photon counting spectroscopic mode at room temperature (24 °C) have been presented. Moreover, one of the 0.06 mm^2 photodiodes and one of the 0.5 mm^2 photodiodes were selected to investigate their electrical performance and the response to the soft X-ray source at high temperatures.

The measurements of capacitance as functions of applied reverse bias showed consistent characteristics between photodiodes of the same active area at room temperature. The depletion widths (2.5 μm and 4.5 μm, respectively) of the devices were calculated based on the capacitance measurements. The photodiodes were found to be fully depleted at $\geqslant$ 120 V reverse bias at room temperature. The results of measurements of the capacitance of one of the 0.06 mm^2 photodiodes and one of the 0.5 mm^2 photodiodes as functions of applied reverse bias at different temperatures showed the consistent capacitance in the investigated range of temperature at high reverse bias ($\geqslant$ 100 V) for both photodiodes. The depletion widths for both devices were found to be 2.34 μm ± 0.03 μm and 4.47 μm ± 0.02 μm at the maximum investigated bias of 120 V at a temperature of 140 °C. At room temperature, measurements of leakage current as a function of applied reverse bias showed low leakage currents among these photodiodes (< 10 pA) at 100 V reverse bias; the current densities were found between 300 pA/cm^2 and 900 pA/cm^2 with the 0.06 mm^2 photodiodes (at electric field strengths of 403 kV/cm) and 1.2 nA/cm^2 to 1.4 nA/cm^2 with 0.5 mm^2 photodiodes (at electric field strengths of 227 kV/cm). Measurements of leakage current as functions of applied reverse bias at varying temperature showed the low leakage currents among these devices (< 10 pA) at 120 V reverse bias at the temperatures lower than 60 °C. The measured leakage currents of both devices were found to be < 2 nA at 120 V reverse bias (electric field strengths of 514 kV/cm and 269 kV/cm for 0.06 mm^2 photodiode and 0.5 mm^2 photodiode, respectively) at the highest investigated temperature (140 °C).

The performance of the four 4H-SiC photodiodes as X-ray detectors was investigated by the measuring the photocurrent generated when the devices were illuminated by an ^{55}Fe radioisotope

X-ray source, and by connecting the photodiodes to a custom low-noise charge-sensitive preamplifier and investigating their performance as detectors for photon counting X-ray spectroscopy. The photocurrents were found to be 5 pA with the 0.06 mm^2 photodiodes and 7 pA – 19 pA with 0.5 mm^2 photodiodes at room temperature. Besides, the largest photocurrents were found to be 4 pA with one of the 0.06 mm^2 photodiodes and 28 pA with one of the 0.5 mm^2 photodiodes at the highest investigated temperature (80 °C) and reverse bias (120 V). Four detectors functioned as photon counting spectroscopic X-rays detectors with modest energy resolution (the *FWHM* at 5.9 keV of the 0.06 mm^2 and 0.5 mm^2 photodiodes were 1.8 keV and 3.3 keV at 100 V reverse bias, respectively). Although the energy resolutions were not as good as many custom X-ray detectors, the results indicated these photodiodes can be used for photon counting X-ray spectroscopy at room temperature albeit with modest energy resolution. Noise analysis of this system was also presented. It showed that dielectric noise and series white noise from stray capacitances were the dominant noise sources in the system. If the noise, which was a consequence of the non-optimal design of the connection of the detectors to the preamplifier, could be entirely eliminated the energy resolution would be expected to improve to 1.1 keV. One of the 0.06 mm^2 detectors functioned as photon counting spectroscopic X-rays detector with modest energy resolution (the *FWHM* at 5.9 keV was 2.6 keV at 100 V reverse bias) at 100 °C. Although the energy resolution was not as good as many custom X-ray detectors, the results showed that the commercial off-the-shelf photodiode could be used for photon counting X-ray spectroscopy at high temperature. Noise analysis of the system was also presented. It showed that the dielectric noise and possible partial charge collection from the substrate were the dominant noise sources in the system in the investigated range of temperatures.

The results presented here indicated these devices achieved a modest spectral resolution which can be a potential attractive option for future low-cost high temperature (> room temperature) X-ray detection applications such as university-led CubeSat missions.

Chapter 4 Further X-ray Spectroscopy and Electron Spectroscopy with a Commercial 4H-SiC UV Photodiode

4.1 Introduction

Whilst significant work developing SiC for photon counting X-ray spectroscopy has been conducted and reported with superb results (Bertuccio et al., 2004) (Bertuccio et al., 2011). SiC has also reported much attention as a particle detector with excellent results, including good properties such as 100% charge collection efficiency (Nava et al., 2004), and high energy resolution (e.g. 0.25% *FWHM* for 5.486 MeV of ^{241}Am (Zat'ko et al., 2015)). However, most work on SiC X-ray and particle detectors has concentrated on custom-made devices, as has already been discussed.

The previous chapter demonstrated that commercial 4H-SiC UV photodiodes could be used for X-ray detection at high temperature (> room temperature) without cooling, thus paving the way for these devices to be used for space science and other applications in future. In this chapter, one of the 0.06 mm^2 4H-SiC photodiodes has been further characterised across the energy range from 4.95 keV to 21.17 keV, using eight different high-purity metal foils fluoresced by an X-ray tube with a Mo cathode at a temperature of 33 °C (see **Section 4.3**). Moreover, the performance of this photodiode as a detector for electrons (β^- particles) detection over the temperature range 100 °C to 20 °C is also presented (see **Section 4.4**). Use of such detectors for electron spectroscopy extends their usefulness beyond X-ray astronomy and planetary science and into space plasma physics.

4.2 Electrical characterisation at 33 °C

4.2.1 Capacitance-voltage measurements

Measurements of the photodiode's capacitance as a function of applied reverse bias have been reported at temperatures from 140 °C to 0 °C, in 20 °C steps in **Section 3.4**. However, since the new X-ray characterisation reported in **Section 4.3** of the present chapter was conducted at 33 °C (a temperature at which capacitance measurements have not been previously reported for this photodiode), for completeness, the capacitance of the packaged 0.06 mm^2 4H-SiC UV photodiode was measured as a function of applied reverse bias at 33 °C. As per previous work, an HP 4275A

Multi Frequency LCR meter was used, in conjunction with a Keithley 6487 Picoammeter/Voltage Source to bias the device, and a TAS Micro MT climatic cabinet for temperature control (see **Section 2.9**). The device was installed inside the cabinet and left to stabilise at 33 °C for 30 min before starting the measurement. The AC test voltage signal magnitude and frequency of the LCR meter were set at 60 mV rms and 1 MHz, respectively. National Instruments Labview software was used to automate the capacitance measurements.

In order to extract the capacitance of the photodiode itself, and separate it from the capacitance of the package (the photodiode and package were considered to be connected in parallel), a sacrificial device of the same type but with its bond wires removed was also measured to yield the packaging capacitance. The capacitance of the photodiode was calculated by subtracting the packaging capacitance (0.75 pF ± 0.01 pF) from the measured total capacitance of the packaged device. The depletion width of the photodiode can be calculated based on the **Equation 2.3**. The measured capacitance, the calculated depletion width and the C^{-2} of the photodiode as functions of applied reverse bias at 33 °C are shown in **Figure 2.1**, respectively. The photodiode appeared to be fully depleted at reverse biases ≥ 100 V, with the implied thickness of the depletion width = 2.69 μm ± 0.05 μm at 100 V reverse bias. The uncertainties associated with the calculated depletion widths were computed taking into account the uncertainties in the capacitance measurements and the Debye length.

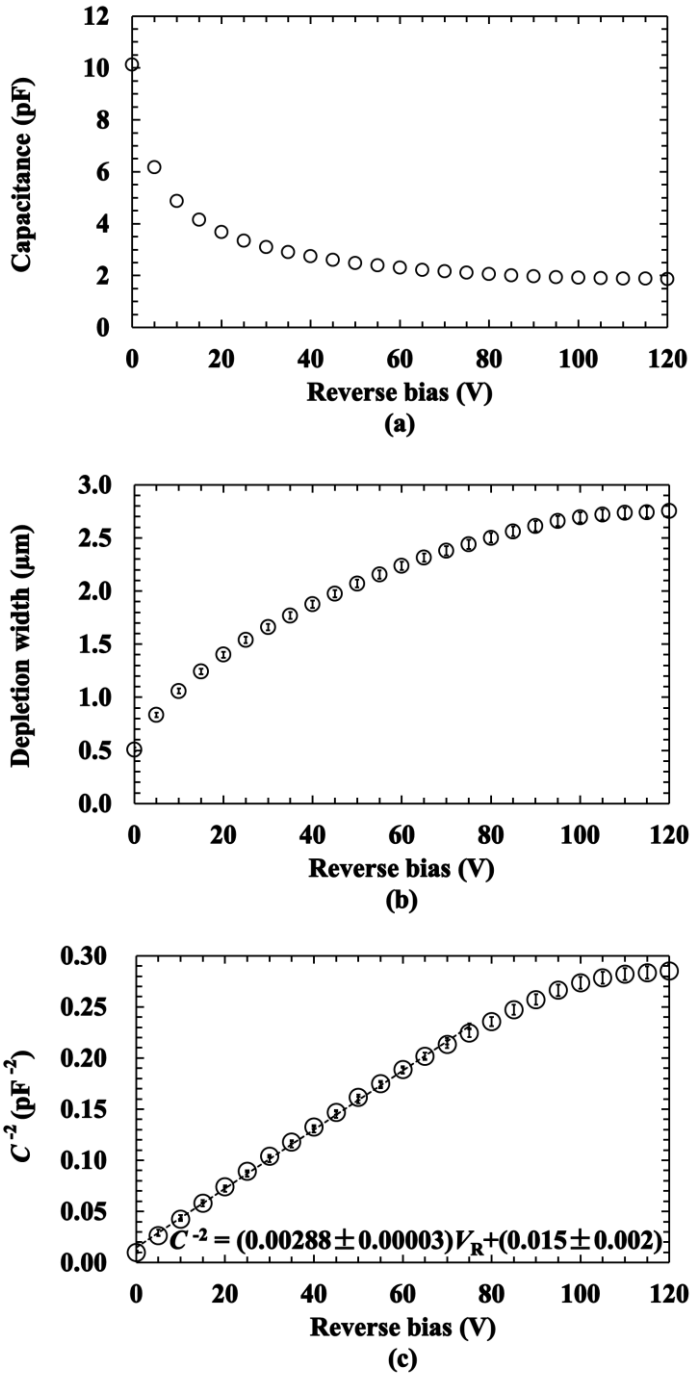

Figure 4.1. The measured capacitance, *C*, (a), calculated apparent depletion width (b), and C^{-2} (c) of the 0.06 mm^2 4H-SiC photodiode as functions of applied reverse bias at 33 °C. The line of best fit was found from 0 V to 75 V as determined by linear least squares fitting is also presented.

Whilst a depletion layer thickness of only 2.69 μm suggests that the quantum efficiency of such a detector would be very low at X-ray energies, previous investigation of these devices showed substantially greater photocurrents than would be expected if the active region of the photodiodes

was simply limited to the apparent depletion width (see **Sections 3.3.1** and **3.5.1**). Previous photocurrent measurements using an ^{55}Fe radioisotope X-ray source to illuminate the detector suggested that the thickness of the active region was 34.5 μm (see **Section 3.5.1**). In addition to the epitaxial layer, part of the substrate was also considered to constitute the active region of the device; the larger than expected photocurrent that was previously measured may be attributed to the collection of the charge carriers generated around the edge of the depletion region (see **Section 3.5.1**). Because the contact of the photodiode has an optical window, and assuming the top layer of the photodiode was active, the quantum detection efficiency, assuming complete collection of the charge created by the X-rays absorbed in the active region, (i.e. active region thicknesses of 2.69 μm and 34.5 μm) was computed using **Equation 2.9**. The calculated quantum detection efficiencies of different thickness of the active regions of the diode are presented in **Figure 4.2** at X-ray energies up to 24 keV.

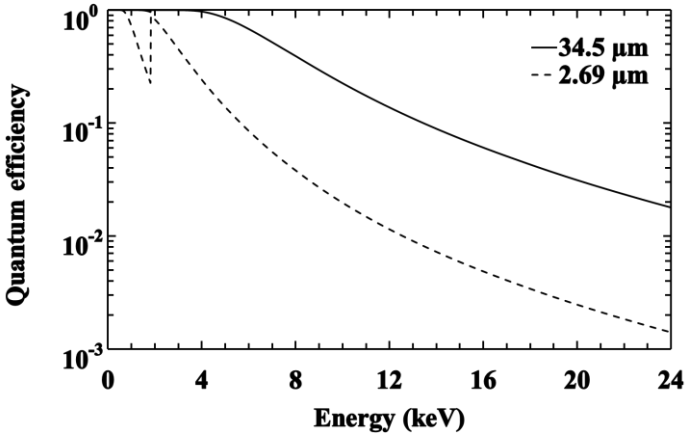

Figure 4.2. The calculated quantum detection efficiencies of the 0.06 mm^2 4H-SiC photodiode based on two different thicknesses of active layer (2.69 μm, dashed line; 34.5 μm solid line) as a function of X-ray energy. The discontinuity at 1.8 keV is the Si K absorption edge.

4.2.2 Current-voltage measurements

Previous measurements of the device's current-voltage characteristics showed that its leakage current at temperatures < 40 °C was too small to be measured with the available experimental set up, even when the detector was operated at high reverse bias (100 V) (see **Section 3.4.2**). However, because the new X-ray measurements reported in **Sections 4.3** of this chapter used long accumulation times (14,000 s and 6 h, respectively) with the device kept reverse biased for these periods, measurements were conducted to determine the time stability of the leakage current. Using a Keithley 6487 Picoammeter/Voltage Source, a TAS Micro MT climatic cabinet, and National Instruments Labview software to automate the measurements (see **Section 2.8**), the

photodiode's leakage current was measured as a function of time when reverse biased at 100 V for 6 h at 33 °C (the temperature at which the X-ray measurements were conducted). The measurements showed that the leakage current remained constant and low (< 0.2 pA) throughout the 6 h period.

4.3 X-ray energy calibration at 33 °C

4.3.1 X-ray fluorescence measurements

In order to accumulate X-ray fluorescence spectra for the eight different high-purity (≥ 98.7%) metal foils (the details of which are shown in **Table 2.1**), the photodiode was connected to a custom-made low-noise charge-sensitive preamplifier with a 2N4416 Si input JFET (capacitance = 2 pF). The detector and preamplifier were housed in a light-tight die cast box, with a 4 μm thick Al X-ray window. The detector was well centred in the middle of the window. An ORTEC 572A shaping amplifier and an ORTEC EASY-MCA 8k multi-channel analyser (MCA) were connected to the preamplifier. The preamplifier and photodiode were installed within a LD Didactic X-ray apparatus (LD Didactic 554 800) with a Mo X-ray tube (LD Didactic 554 861) and a sample stand goniometer (LD Didactic 554 831) which was used to hold each high-purity foil in turn. A custom-made aluminium-PTFE collimator (20 mm central open diameter) was used to collimate the X-rays from the X-ray tube. The sample stand goniometer was set at 45 ° with respect to the collimator. The detector was positioned at 135 ° with respect to the collimator, with the detector facing towards the focus of the circle of rotation (see **Section 2.11)**. The distance between the centre of the Mo target tube and the collimator was 40 mm ± 3 mm, the length of the collimator was 105.00 mm ± 0.02 mm, the distance between the collimator and the target stand goniometer was 43 mm ± 1 mm, the distance between the target stand goniometer and the spectrometer was 57 mm ± 1 mm, and the solid angle subtended by the detector from the position of the target stand goniometer was 0.015 π sr ± 0.001 π sr. This geometry minimised the detection of X-rays directly from the tube whilst ensuring good detection of the fluorescence X-rays from the foils. The PTFE inner of the collimator ensured complete absorption of any fluorescence X-rays from the aluminium of the collimator. In order to eliminate any influence of humidity effects upon the detector, dry N_2 gas was flowed through the detector-preamplifier assembly throughout the accumulation of the spectra. The preamplifier was powered continuously throughout the accumulation of the spectra of the foils. The photodiode was reverse biased at 100 V to accumulate each spectrum and was only powered off when the high-purity fluorescence foil was changed. The shaping time of the shaping amplifier was set to the longest available (10 μs) due

to the large capacitance and low leakage current of the detector in order to minimise total electronic noise and thus achieve better energy resolution (Bertuccio et al., 1996) (Barnett et al., 2012).

Each foil was fluoresced by X-rays from the Mo X-ray tube, which was operated at a potential difference of 35 kV and a current of 1 mA. X-ray fluorescence spectra were accumulated for each foil using the SiC detector. The accumulation time for each spectrum was 14,000 s. To ensure the temperatures of the detector, preamplifier, and X-ray tube were constant, the X-ray tube was switched on and allowed to warm up for three hours prior to the start of spectrum accumulation in each case; this brought the environment of the detector and preamplifier to a constant temperature of 33 °C (Barnett et al., 2013b). The MCA's charge scale was energy calibrated using the measurement described in **Section 4.3.3**; the equation relating photon energy to MCA channel number is given as **Equation 4.1** in **Section 4.3.3**.

4.3.2 Spectrometer energy resolution

The Fano-limited energy resolution as quantified by the full width at half maximum of a photopeak ($FWHM_{\mathrm{Fano}}$) of a non-avalanche photodiode X-ray spectrometer is given by the **Equation 2.12**. However, the energy resolution of a photodiode spectrometer is further affected by noise from incomplete charge collection and electronic noise (including parallel white, series white, 1/*f* series, and dielectric noise) from the detector and preamplifier system, and the shaping amplifier characteristics. Thus the total noise limiting the energy resolution of the spectrometer arises not only from the Fano noise of the detector but also these other sources (see **Equation 2.13**). aE^b is the incomplete charge collection noise (see **Equation 2.13**) from the detector with *a* and *b* being semi-empirical constants determined by best-fitting (Owens, 2012). A detailed electronic noise analysis for the detector at room temperature was presented in **Section 3.3.2.2**.

For each foil X-ray spectrum obtained, the *FWHM* of the foil's primary X-ray fluorescence line was measured and is shown in **Figure 4.3**. An example X-ray fluorescence spectrum obtained with the Ge (Kα = 9.88 keV and Kβ = 10.98 keV (Sánchez del Rio et al., 2003)) foil is presented in **Figure 4.4**. The expected Fano-limited *FWHM* at 9.88 keV for a SiC detector is 207 eV.

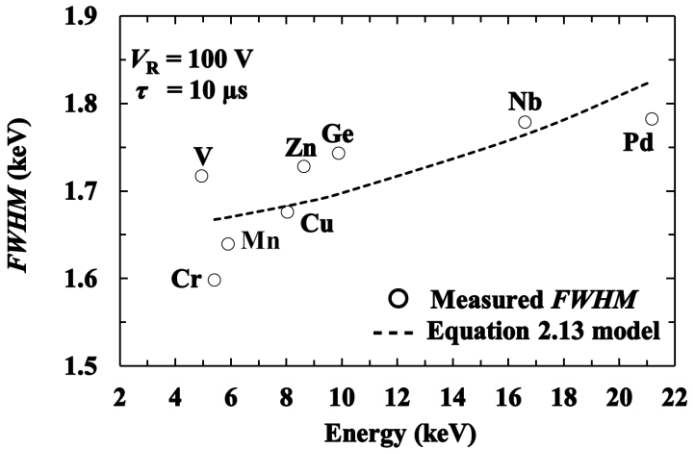

Figure 4.3. Measured *FWHM* of the primary X-ray fluorescence lines of eight different materials with the detector operated at 100 V reverse bias (V_R) and using a 10 µs shaping time (τ). The expected *FWHM* from **Equation 2.13** model is also presented.

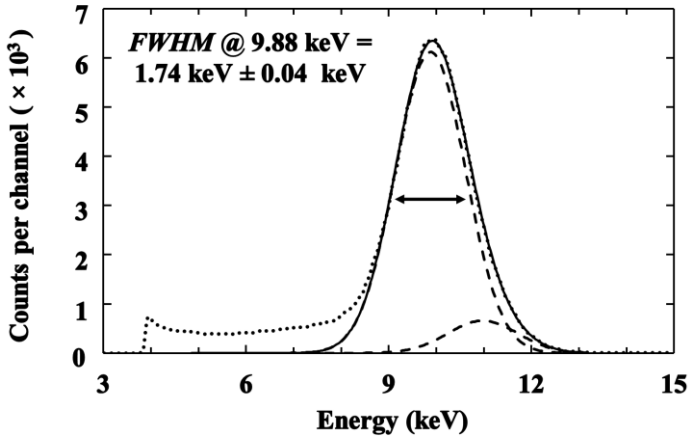

Figure 4.4. Ge X-ray fluorescence spectrum accumulated with the 0.06 mm^2 4H-SiC photodiode at 100 V reverse bias. The dotted line is the obtained Ge spectrum, the dashed lines are the fitted Ge Kα and Kβ peaks, and the solid line is the combination of the fitted Ge Kα and Kβ peaks.

The results in **Figure 4.3** show that a *FWHM* of 1.6 keV – 1.8 keV was achieved across the energy range 4.95 keV – 21.17 keV. In each case, the *FWHM* was substantially larger than the expected $FWHM_{Fano}$ due to the influence of the additional noise components in **Equation 2.13** cf. **Equation 2.12**. At the softest investigated energy V $K\alpha_1$ (4.95 keV), the low energy tail of the photopeak was also partly overlapped by the tail of the zero energy noise peak which broadened the apparent *FWHM* of the V Kα photopeak.

Excluding V, the measured *FWHM* of the primary fluorescence line of each foil was found to be

a function of photon energy. Interestingly, even though the $FWHM_{Fano}$ was calculated to increase with increasing photon energy, the experimentally observed *FWHM* increase could not be explained solely by the increasing Fano noise. The greater than anticipated increase in the measured *FWHM* with increased photon energy may be attributable to incomplete charge collection noise; electronic noise is independent of photon energy but incomplete charge collection noise is energy dependent (Owens et al., 2001). As discussed in **Section 4.2.1**, it appeared that the active region of the photodiode was not restricted to the apparent depletion layer thickness (i.e. the epilayer) but more likely also included a portion of the device's substrate. Charge transport in high-quality 4H-SiC epilayers is such that significant incomplete charge collection is improbable in such an epilayer, especially at the field strengths investigated. However, the same is not necessarily true for the substrate on which the epilayer was grown, particularly because the substrate will have a lower electric field strength within it compared to the epilayer, even when the photodiode is operated at high reverse bias. Given this, it is hypothesised that any apparent incomplete charge collection noise from the detector results from charge carriers created in the substrate as a result of photons absorbed there, rather than from charge carriers created by photons absorbed in the epilayer (see **Section 3.5.1**). Furthermore, generally speaking, lower energy X-ray photons have larger linear attenuation coefficients than higher energy X-ray photons. Thus, given the relative thinness of the detector's epilayer, the energy dependence of the apparent incomplete charge collection noise may have been further enhanced by positional effects: proportionally more photons of higher energy (cf. those of lower energy) will have been absorbed in the possibly lossy substrate compared with the high-quality epilayer. Thus, the significance of incomplete charge collection noise from the substrate may have been augmented by this at higher photon energies. The claim of a 34.5 μm active layer was based on the assumption of the active region of the substrate having the same quantum efficiency as the epilayer. The thickness of the active layer may be different if the quantum efficiency of the substrate deviates significantly from that of the epilayer as a result of charge trapping or other loss mechanisms in the substrate.

The apparent contribution to the measured *FWHM* from incomplete charge collection noise was calculated by fitting the data at energies ≥ 5.41 keV (Cr $K\alpha_1$) and assuming a form aE^b (as per **Equation 2.13**). It was found that a = 0.03 and b = 1, with the electronic noise (M in **Equation 2.13**) = 1650 eV ± 15 eV. The incomplete charge collection noise of the detector at Cr $K\alpha_1$ (5.41 keV) was found to be 162 eV. At the highest investigated energy (Pd $K\alpha_1$ = 21.17 keV) the incomplete charge collection noise was 635 eV. These apparent noise contributions were larger than the Fano noise at each energy (e.g. 153 eV at 5.41 keV; 303 eV at 21.17 keV) but much smaller than the electronic noise.

The energy resolutions achieved were modest compared with the highest quality custom SiC X-ray photodiodes (*FWHM* = 196 eV at 5.9 keV (Bertuccio et al., 2011)) and high quality GaAs X-ray photodiodes (*FWHM* = 625 eV at 5.9 keV (Lioliou & Barnett, 2016); and *FWHM* = 380 eV at 5.9 keV (Owens et al., 2002)). However, they were comparable to some custom SiC X-ray detectors (*FWHM* = 1.6 keV at 5.9 keV (Barnett, 2011) and *FWHM* = 1.36 keV to 1.68 keV at 17.4 keV (Lioliou et al., 2016c)) and better than has been achieved using other SiC UV photodiodes repurposed as X-ray detectors (*FWHM* = 3 keV at 5.9 keV (Lees et al., 2012)).

4.3.3 Energy response linearity

In addition to other characteristics, such as energy resolution and quantum efficiency, an important characteristic of detectors for X-ray spectrometers for photon counting spectroscopy is their energy response linearity; this is the degree to which the charge output by the detector is linearly proportional to the energy of the incident photon. It has been previously shown that high energy linearity is achievable with compound semiconductor detectors (Bertuccio et al., 1997). Good understanding of the detector's performance in this regard is essential in order to achieve accurate calibration of the energy scale of X-ray spectra obtained with the device. The energy response linearity of an X-ray photodiode is influenced by factors including polarization effects, charge trapping, and charge collection efficiency (Knoll, 2010). In order to characterise the energy linearity of the SiC detector X-ray spectrometer, the spectra obtained of the eight high-purity fluorescence foils were fitted with Gaussians in order to determine in each case the multi-channel analyser (MCA) channel number at which the centroid of the primary X-ray fluorescence peak (see **Table 2.1**) was located. The positions of the photopeak centroids in terms of MCA channel number were then plotted as a function of photopeak energy in order to produce **Figure 4.5**. In cases of multiple overlapping peaks (e.g. for the Kα and Kβ peaks of Ge, as shown in **Figure 4.4**) the primary emission line peak was deconvolved from the detected combined photopeak to enable the position and energy of the primary photopeak to be used.

Linear least squares fitting showed that the relationship between the incident photon energy, E (in units of keV), and the MCA channel number, Y (in units of adu), was represented by the equation,

$$Y = (32.55 \pm 0.04)E + (2.07 \pm 0.45). \quad (4.1)$$

The fitting error bars (± 0.61 channels) associated with each data point were determined using the gradient and the y-axis intercept of the linear least squares fitting, which can be expressed as

$$S = \sqrt{\left(\frac{\sum \left(Y_i - \left(\left(\frac{n\sum(E_i Y_i) - \sum E_i \sum Y_i}{n\sum {E_i}^2 - \left(\sum E_i\right)^2} \right) E_i + \frac{\sum {E_i}^2 \sum Y_i - \sum E_i \sum (E_i Y_i)}{n\sum {E_i}^2 - \left(\sum E_i\right)^2} \right) \right)^2}{n-2} \right)} \quad (4.2)$$

where, n is the number of data points, E_i (in units of keV) is the photon energy, and Y_i (in units of adu) is the MCA channel number, of the ith data point. This error bar was smaller than the analytical uncertainty associated with the determination of the centroid for each peak, and thus the data in **Figure 4.5** were appropriately fitted by a linear equation. The results show that despite the possible presence of some incomplete charge collection from photons absorbed in the device's substrate, the spectrometer's energy scale is still linear over the investigated range.

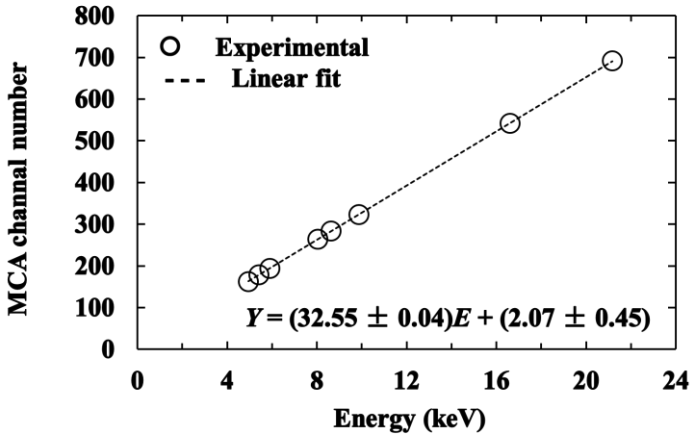

Figure 4.5. The energy response linearity of the 0.06 mm^2 4H-SiC photodiode over the range 5 keV - 21 keV. To determine the relationship between the incident photon energy, E, and the MCA channel number, Y, the positions of the centroids of the primary X-ray emission lines of the obtained spectra (in term of MCA channel number) were plotted as a function of the accepted energies of these emissions. The linearity error (evaluated by residuals of the fit in percentage terms) was found to be less than ± 0.7%.

4.3.4 X-ray intensity measurements

Even the brightest cosmic X-ray sources provide relatively low X-ray fluxes at the Earth's orbit (e.g. 150 photons cm^{-2} s^{-1} for Sco X-1 (Paradijs & Bleeker, 1999)). Consequently, detectors for such applications have to be high efficiency and are commonly accompanied by X-ray optics to improve detected count rates. However, the Sun is a significantly brighter X-ray source, and there is the opportunity to make interesting X-ray heliophysics observations using simple and compact X-ray instrumentation carried on board CubeSats which do not benefit from X-ray optics

(Woods et al., 2017). X-ray observations of solar flares are one such area of interest, not least due to the significant impact solar flares can have on the geospace environment, including disrupting communications and navigation technologies, and damaging space hardware. As instrumentation which would be exposed to solar flares, the use of SiC rather than Si detectors in solar flare monitoring spacecraft is of interest due to the improved radiation-hardness of SiC. Solar flares can give rise to typical X-ray fluxes at the Earth's orbit of ~10^5 to 10^6 photons s^{-1} cm^{-2} keV^{-1} at X-ray photon energies $\lesssim$ 10 keV (Benz et al., 2012), and reduced, but still significant, fluxes at harder energies. For a 0.06 mm^2 detector as characterised in this article, this suggests detector incident fluxes ~60 to 600 photons s^{-1} keV^{-1} at energies $\lesssim$ 10 keV.

In order to investigate the detector's response to illumination with different intensities (fluxes) of X-rays, the count rate of the detector was investigated by fluorescing the Ge (Kα = 9.88 keV and Kβ = 10.98 keV) foil sample at five different X-ray tube currents from 0.2 mA to 1.0 mA, in 0.2 mA steps. The potential difference of the X-ray tube was kept at 35 kV throughout the measurements. To extend the range of fluxes investigated, the experiment was conducted using two custom Al-PTFE X-ray collimators of different internal open diameters (8 mm ± 0.02 mm and 20 mm ± 0.02 mm) at each X-ray tube current, in turn. The collimators were designed such that all X-ray fluorescence from the Al cladding of the collimators was absorbed by the PTFE inners. The live time limit for the accumulation of each spectrum was 6 hours. The equipment was otherwise configured as per **Section 4.3.2**. The results of X-ray intensity measurements are shown in **Figure 4.6**. To verify that the X-ray tube's emission flux was linearly proportional to the X-ray tube's current, the X-ray tube's emissions were measured at each investigated tube current with a reference Si detector (LD Didactic 559 938) prior to the measurements of the Ge X-ray fluorescence with the SiC detector. The measurements with the Si reference detector confirmed the X-ray tube's linear proportionality.

A linear relationship was found between X-ray tube current and the SiC photodiode's detected count rate, ρ, (as defined by the number of counts contained within the Gaussian fitted to the deconvolved Ge Kα peak for each tube current and collimator combination, divided by the spectrum's live limit accumulation time i.e. 6 hours). By linear least squares fitting, the relationships were found to be described by the equations,

$$\rho_{8\mathrm{mm}} = (6.50 \pm 0.09)I + (0.09 \pm 0.06) \tag{4.3}$$

and

$$\rho_{20\mathrm{mm}} = (31.98 \pm 0.37)I - (0.07 \pm 0.25), \tag{4.4}$$

where ρ_{8mm} and ρ_{20mm} are the number of counts per second that contributed to the detected Ge Kα peak when the 8 mm and 20 mm collimators were used respectively, and I is the X-ray tube current in units of mA. The error bars associated with each data point as determined by **Equation 4.2** were ± 0.06 counts s^{-1} and ± 0.24 counts s^{-1}, respectively. This is smaller than the analytical uncertainty associated with the determination of the number of counts in each fitted Gaussian and thus confirmed the appropriateness of a linear fit and hence that the response of the SiC spectrometer was linear at detected count rates from 1.4 counts s^{-1} to 31.7 counts s^{-1} at 9.88 keV. If the quantum efficiency of the detector at this energy was 0.02 (i.e. assuming a 2.69 µm active layer), these detected count rates correspond to incident 9.88 keV photon fluxes of 70 photons s^{-1} to 1585 photons s^{-1} on the detector. If the quantum efficiency of the detector was 0.23 (i.e. assuming a 34.5 µm active layer) the count rates correspond to incident 9.88 keV photon fluxes of 6 photons s^{-1} to 138 photons s^{-1} on the detector. Whilst it should be noted that solar flare X-ray spectra are not monochromatic, and thus the total energy deposited per second in a detector of this type when monitoring a flare will be greater than that investigated here, the results do provide an initial indication of the detector's potential suitability for this application in terms of count rate linearity near 10 keV.

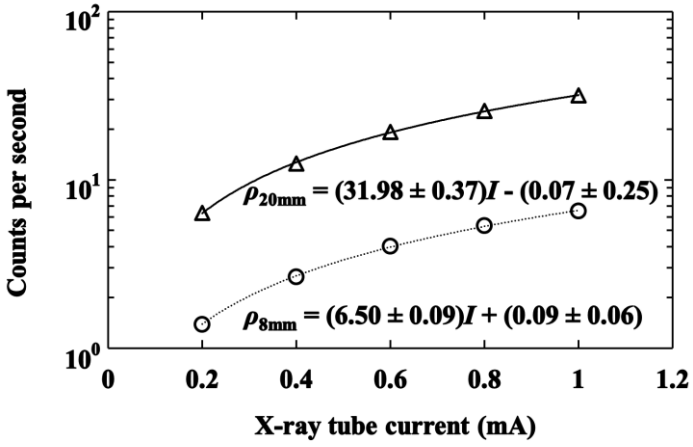

Figure 4.6. X-ray intensity response of the 0.06 mm^2 photodiode, showing the number of detected counts per second (defined as the number of counts contained within the Gaussian fitted to the Ge Kα X-ray fluorescence peak divided by the spectrum accumulation time) as a function of X-ray tube current. Count rates are shown when using collimators with 8 mm (open circles) and 20 mm (open triangles) diameter apertures. The linearity error (evaluated by residuals of the fit in percentage terms) was less than ± 2%.

4.4 Electron spectroscopy experiments

4.4.1 Leakage currents as functions of applied reverse bias measurement

The leakage current of the photodiode was measured as a function of applied reverse bias from 0 V to 100 V in 1 V increments, at temperatures from 100 °C to 20 °C in steps of 20 °C. To do this, the detector was installed inside a light-tight electromagnetically-shielded box inside a TAS Micro MT Environmental Test Chamber. A dry N_2 environment (relative humidity < 5%) was maintained inside the chamber in order to eliminate any humidity related effects. A Keithley 6487 Picoammeter/Voltage Source was used to bias the detector. National Instruments Labview software was used to automate the measurements (see **Section 2.8**). To ensure thermal equilibrium, the detector was allowed 30 min to stabilise at each temperature before measurements were started. The results are presented in **Figure 4.7**. The leakage current of the detector at 100 V reverse bias and the highest investigated temperature (100 °C) was found to be 44.9 pA ± 0.5 pA (corresponding to leakage current density of 74.9 nA/cm^2 ± 0.9 nA/cm^2). The leakage currents of the device were < 1 pA at temperatures ≤ 40 °C. It should be emphasised that the measured currents include the leakage current of the TO-18 can. The Keithley 6487 Picoammeter/Voltage Source had a measurement uncertainty of ± 0.4 pA; as such, the measurements at 40 °C and 20 °C shown in **Figure 4.7** are considered to be below the noise floor of the picoammeter.

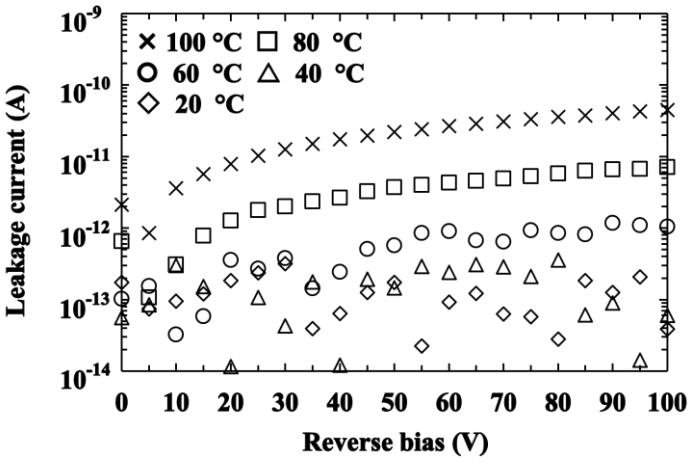

Figure 4.7. Leakage currents as functions of applied reverse bias for the 0.06 mm^2 photodiode in the range of temperature from 100 °C to 20 °C.

4.4.2 Current mode β^- particle measurements

A ^{63}Ni radioisotope β^- particle source (consisting of a 3 μm thick ^{63}Ni layer electroplated onto an ~50 μm thick inactive Ni foil substrate and then covered with a protective 1 μm thick inactive

electroplated Ni overlayer) was placed 4.5 mm ± 1.0 mm above the photodiode to investigate the β^- particle response of the photodiode (see **Section 2.8**). The ^{63}Ni radioisotope β^- particle source had an active face area of 49 mm^2 and an apparent activity of 136 MBq. The resultant current was measured using the same method as was used for the leakage current measurements (see **Section 2.8**). The apparent measured β^- particle created current (i.e. the current measured with each device illuminated with the ^{63}Ni radioisotope β^- particle source with the previously measured leakage current subtracted) as a function of applied reverse bias for the device at temperatures from 100 °C to 20 °C is presented in **Figure 4.8**.

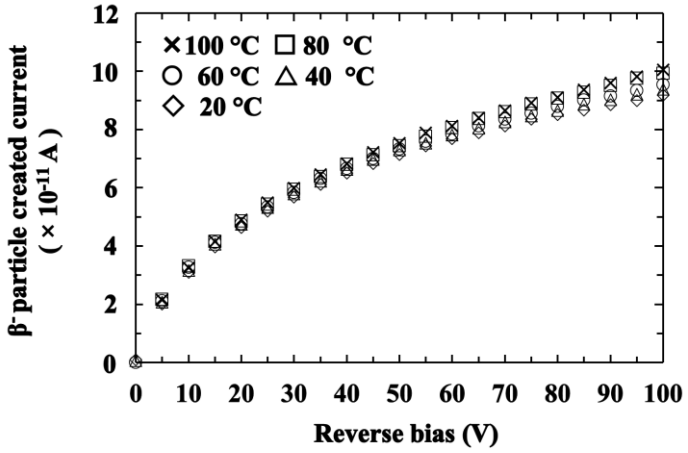

Figure 4.8. Measured apparent β^- particle created currents as functions of reverse bias for the 0.06 mm^2 photodiode in the range of temperature from 100 °C to 20 °C.

Previous X-ray measurements with the photodiode suggested that despite the detector having a stated epilayer thickness of 5.15 µm (see **Section 1.9.1**) and a depletion region thickness of 2.37 µm (assuming a parallel plate capacitance) (see **Section 3.4.1**), collection of charge carriers created by X-rays absorbed substrate may have contributed significantly to the detected signal. These previous measurements suggested that the detector appeared to have an active region which was 34.5 µm thick (see **Section 3.5.1**). Therefore, to compare with the experimental results, calculations were performed to predict the β^- particle created current expected to be detected under the circumstances that the active region thickness was (a) 5.15 µm, (b) 2.37 µm, and (c) 34.5 µm. The expected β^- particle created current was calculated using **Equation 2.7**.

The predicted β^- particle created current of the 0.06 mm^2 photodiode at room temperature was calculated to be 12.5 pA assuming a 5.15 µm thick active region, 9.2 pA assuming a 2.37 µm active region, and 13.8 pA assuming a 34.5 µm thick active region. However, the experimentally measured β^- particle created current of the 0.06 mm^2 photodiode was found to be 92 pA ± 1 pA at 100 V reverse bias and 20 °C.

The explanation of the difference in the predicted β^- particle created currents and the experimental β^- particle created currents of the 0.06 mm^2 photodiode is still not known with absolute certainty. However, the experimentally measured β^- particle created currents were found to be greater at higher temperatures (see **Figure 4.8**). In part, this may be explained by the average energy consumed in the generation of an electron-hole pair (the quantity commonly called the electron-hole pair creation energy) reducing with increasing temperature (Alig & Bloom, 1975) (Levinshtein et al., 2001). Assuming Si, GaAs, and 4H-SiC have a linear relationship between the electron-hole pair creation energy and the bandgap energy at 100 °C, the electron-hole pair creation energy of 4H-SiC at this temperature can be estimated to be 7.24 eV. Therefore, at 100 °C, the predicted β^- particle created current for the 0.06 mm^2 photodiode (active region thickness = 5.15 µm) would increase to 13.5 pA from 12.5 pA at 20 °C. However, the apparent β^- particle created currents in the detector showed a much more significant increase at reverse biases > 60 V at temperatures > 40 °C. As such, this effect may be due to the variation of the leakage component of the current which may have varied between measurement in dark condition and measurement when illuminated with the ^{63}Ni radioisotope β^- particle source. If the leakage component of the current was greater in the measurement with the device illuminated than when the device was measured in a dark condition it would have produced an apparently (but not truly) greater β^- particle created current. However, a variation in leakage current of such size would be surprising. Use of a chopper wheel and lock-in amplifier apparatus to measure the response of the photodiode in both dark and illuminated condition within one experiment would have eliminated any effects from this, but as mentioned previously, we do not possess such equipment at our laboratory at present.

4.4.3 ^{63}Ni β^- particle spectroscopy

The detector was connected to a custom-made low-noise charge-sensitive preamplifier with a wire-ended packaged 2N4416A silicon input JFET (capacitance = 2 pF) and installed in a TAS Micro MT climatic cabinet for temperature control as per the current-mode measurements. The preamplifier was of feedback resistorless design similar to Bertuccio et al. (1993). An ORTEC 572A shaping amplifier and an ORTEC EASY-MCA 8k multi-channel analyser (MCA) were connected to the preamplifier's output (see **Section 2.11**).

The distance between the ^{63}Ni radioisotope β^- particle source and the photodiode's top surface was 4.5 mm ± 1.0 mm. The accumulation live time for each ^{63}Ni β^- particle spectrum was 720 s. The β^- particle spectra were accumulated at the temperatures from 100 °C to 20 °C with 20 °C decrements. Since the accumulated spectra at each temperature were relatively similar, for clarity only the spectra accumulated at 100 °C and 20 °C are presented in **Figure 4.9**. The shaping time

of the shaping amplifier was set at 1 μs for the spectrum accumulated at 100 °C and at 2 μs for 20 °C. The results demonstrated that these detectors can be used as detectors for particle counting β^- (electron) spectroscopy at temperatures up to 100 °C.

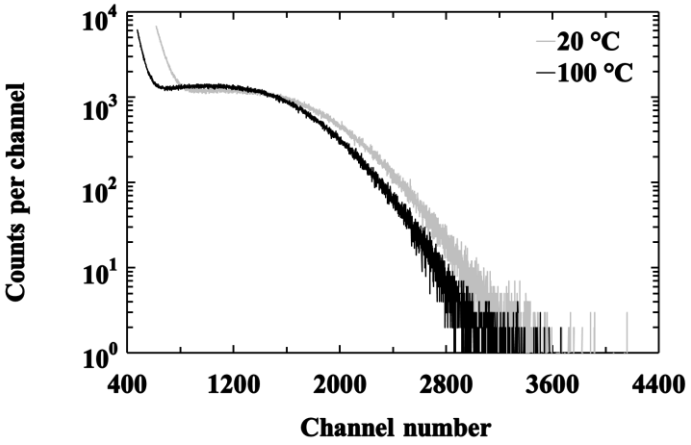

Figure 4.9. ^{63}Ni β^- spectra obtained with the 0.06 mm^2 photodiode at 100 V reverse bias at 20 °C (grey line) and 100 °C (black line).

Effects such as the change in electron-hole pair creation energy with temperature, and the change in preamplifier conversion factor with temperature will have been responsible in part for the change in apparent end point channel between temperatures. A degradation in the energy resolution of the spectrometer at higher temperatures (as was reported for the devices when used for photon counting X-ray spectroscopy (see **Section 3.5.2.1**), will have blurred the end point channel more at higher temperatures than at lower temperatures. Furthermore, changing the shaping time of the shaping amplifier will have also effectively changed the width of the MCA channels in terms of eV per channel. The variation with temperature of the densities of the ^{63}Ni radioisotope β^- particle source, the N_2 atmosphere, and the detector will also have had some small effects (e.g. the lower density of the N_2 atmosphere at higher temperatures will have resulted in reduced energy losses in the N_2) but they are expected to have been less significant in effect than the changes in the other aspects outlined above.

In **Section 4.6**, the experimentally obtained ^{63}Ni β^- particle spectrum at 20 °C is compared with the spectrum predicted from the Monte Carlo modelling in **Section 4.5**.

4.5 CASINO simulations

The trajectories of electrons (β^- particles) passing through materials can be simulated using the

CASINO computer program (Drouin et al., 1997) (Hovington et al., 1997). Such simulations can be used to give an indication of how the structure of the photodiode (e.g. thickness of dead layers and active layers) affected the total energy deposited in the active layer of the device and hence what charge was detected. Electron energy losses in the photodiode's contact were negligible because it had an optical window. However, the β^- particles did lose energy as they travelled between the atom from which they were emitted and the photodiode. These energy losses occurred through self-absorption in the ^{63}Ni radioisotope β^- particle source (Sims & Juhnke, 1967), in the 1 μm thick protective inactive nickel overlayer of the source (density = 8.908 g/cm^3 at room temperature (Greenwood & Earnshaw, 1997)), and in the dry N_2 atmosphere (density = 0.0012 g/cm^3 at room temperature (Younglove & Olien, 1985)). Simulations were conducted to model these effects.

The aims of the simulations were to predict (a) the electron spectrum incident on the photodiode (i.e. taking into account energy losses from self-absorption, the inactive Ni overlayer, and the dry N_2 atmosphere), and (b) the electron spectrum detected by the photodiode to account for the fact that the remaining energy of the electrons may not have been fully absorbed by the relatively thin photodiode. The simulations tracked the path of each simulated electron through the various media and recorded the quantities and locations of the deposited energy along each track. The simulations were parallelised across 10 computers with Intel Core i7-6700 CPUs. Each computer had 32 GB of random access memory. As per **Section 4.4.2**, since there was doubt about the thickness of the detector's active region simulations were conducted to model three different active region thickness: (a) 5.15 μm, (b) 2.37 μm, and (c) 34.5 μm.

The simulations were conducted in three stages. Firstly, the electron (β^- particle) quantum efficiency of the photodiode in each case was computed. Secondly, the electron (β^- particle) spectrum expected to reach the detector was computed. Thirdly, the first and second stages were combined to predict the detected spectrum (excluding the noise processes known to broaden the energy resolution of photodiode radiation detectors i.e. Fano noise, electronic noise, and incomplete charge collection noise (Owens, 2012).

In the first stage, for electron energies from 1 keV to 66 keV, in 1 keV steps, 4000 electrons at each energy were simulated to be incident on the face of the photodiode. The quantum efficiency of the photodiode at each energy, defined as the ratio between the energy deposited in the active region and the energy incident on the photodiode, was computed. The results are presented in **Figure 4.10** for the active region thicknesses outlined above. The quantum efficiency in each case was found to be similar at energies < 20 keV. At these energies, the quantum efficiency in all three cases was > 90%. At energies > 20 keV and > 30 keV, the quantum efficiencies

associated with the 2.37 μm and 5.15 μm active region thicknesses, respectively, were reduced.

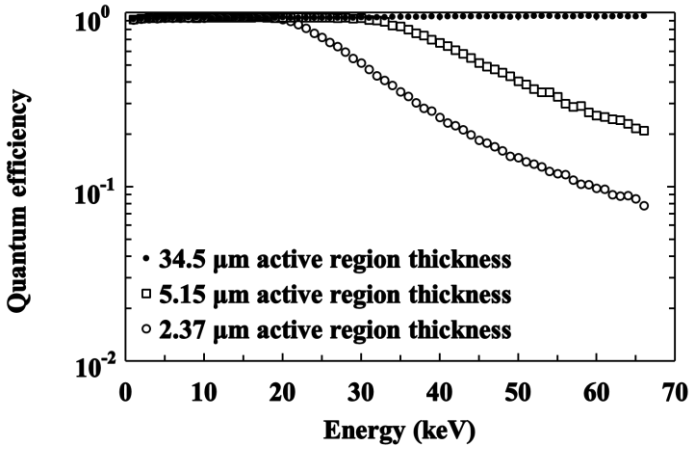

Figure 4.10. Electron (β^- particle) quantum efficiency computed for the detector assuming active region thicknesses of 34.5 μm (filled circles), 5.15 μm (open squares), and 2.37 μm (open circles).

In the second stage, the spectrum of electron energies incident on the detector from the ^{63}Ni radioisotope β^- particle source was simulated. Electrons were simulated to be emitted from the ^{63}Ni at energies from 1 keV to 66 keV in 1 keV steps in the relative emission ratios for ^{63}Ni and taking account of self-absorption (Liu et al., 2015). A total of 1.84×10^7 electrons were simulated to be emitted. Passage of the electrons through the 1 μm thick inactive Ni overlayer and the 4.5 mm thick N_2 atmosphere was simulated. For every electron which was not entirely absorbed in the Ni overlayer or the N_2 atmosphere, the energy remaining after the transmission was stored in the computer. The dataset was then binned into energy channels of 1 keV width to produce a histogram showing the distribution of remaining electron energies. This histogram is the spectrum of electron energies predicted to be incident on the detector. It is shown in **Figure 4.11** together with the ^{63}Ni emission spectrum taking into account the self-absorption of the source.

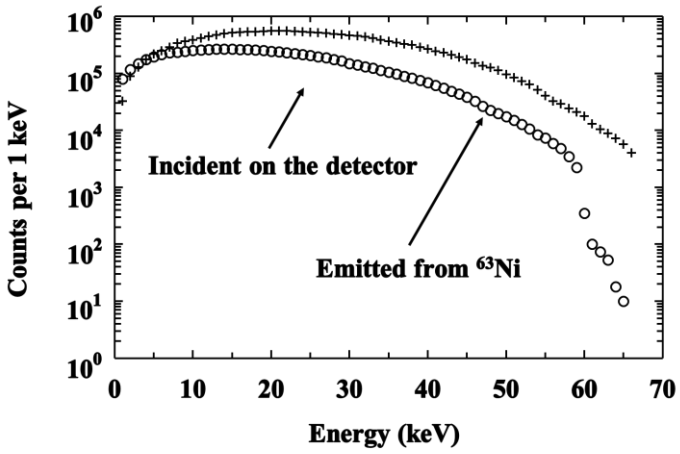

Figure 4.11. Comparison between the β^- particle spectra emitted from the ^{63}Ni radioisotope β^- particle source including self-absorption but excluding attenuation in the 1 μm inactive overlayer (+ symbols) and incident on the top of the photodiode taking into account losses in the 1 μm inactive overlayer and the N_2 atmosphere (open circles).

In the third (and final) stage, the results of the first two stages were combined to produce the spectra predicted to be detected by the spectrometer for each simulated photodiode active layer thicknesses. The predicted spectra exclude effects such as pulse pile-up, noise processes, and detector edge effects. The spectra are shown in **Figure 4.12**.

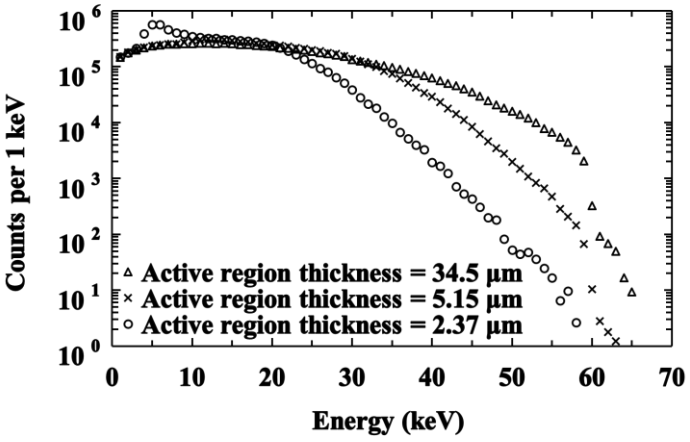

Figure 4.12. Comparison of the β^- particle spectra predicted to be detected by the spectrometer in the case that the detectors active region thickness is 34.5 μm (open triangles), 5.15 μm (× symbols), and 2.37 μm (open circles). The spectra do not include effects such as pulse pile-up, noise processes, and detector edge effects.

For the simulations of the 34.5 μm and 5.15 μm active region thickness, the spectra had smooth shapes at detected energies up to 59 keV. However, the 2.37 μm active region thickness

simulations predicted an increased number of counts around 5 keV. This is a consequence of the thinner active region detecting only a portion of the energy of electrons with greater total energy; that is to say that there is an increased likelihood that the β^- particles in this case deposit only ~5 keV in the detector before leaving the active region in this case. A further interesting feature of the spectra corresponding to the 34.5 μm and 5.15 μm cases is the rapid decrease in detected counts at energies > 59 keV. Whilst the emission spectrum of ^{63}Ni does rapidly reduce at energies close to its endpoint energy, a further effect is at work in the spectra shown in **Figure 4.12**. Here, the natural rapid drop is enhanced by the low and compounding probabilities of electrons retaining such large amounts of energy after their passage through the source's inactive overlayer and the 4.5 mm thick N_2 layer, and then depositing such large amounts of energy in the detector.

4.6 Comparison of simulation and experimental results

The simulated detected β^- spectrum was then compared with the experimentally accumulated spectrum at 20 °C. The heights of the simulated spectra have been normalised to the experimental spectrum by the same factor to take account of the accumulation time of the experimental spectrum and the ^{63}Ni radioisotope β^- particle source's activity. The comparison is presented in **Figure 4.13**.

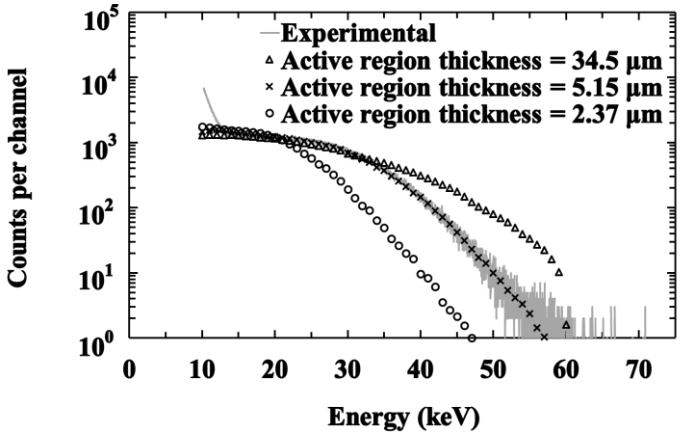

Figure 4.13. Comparison between the experimentally detected ^{63}Ni β^- particle spectrum at 20 °C (grey solid line), and the simulated spectra assuming active region thicknesses of: 34.5 μm (open triangles), 5.15 μm (× symbols), and 2.37 μm (open circles).

Comparing the shapes of the β^- spectra simulated using the CASINO simulations and the spectrum experimentally obtained at a temperature of 20 °C, it can be seen that the simulation using an active region thickness of 5.15 μm produces a good agreement with experimental β^- particle

spectrum. In contrast, the simulations using active region thicknesses of 2.37 µm and 34.5 µm do not match the experimental spectrum. As such, this is an indication that the thickness of the active region of the detector was 5.15 µm, which is the thickness of the epilayer as stated by the manufacturer. The few detected counts seen in the spectrum above 57 keV may be due to the statistical effects of pulse pile-up and other noise contributions.

4.7 Conclusions and discussion

A 0.06 mm^2 commercial 4H-SiC UV p-n photodiode has been investigated for its performance as a detector for photon counting X-ray spectroscopy at photon energies from 4.95 keV to 21.17 keV. This photodiode was also investigated as current mode and pulse mode detector of β^- particles over the temperature range 100 °C to 20 °C.

The X-ray performance of the detector when connected to a custom-made low-noise charge-sensitive preamplifier was investigated by illuminating the detector with fluorescence X-rays (of energy 4.95 keV - 21.17 keV) from eight different high-purity metal foils which were fluoresced by a Mo cathode X-ray tube operated at 35 kV and 1 mA. The detector and preamplifier were operated uncooled at a temperature of 33 °C. The results showed that the spectrometer had an energy resolution (*FWHM*) of 1.6 keV - 1.8 keV across the energy range when operated at +33 °C. The charge detected (and hence the spectrometer's output) was found to be a linear function of the photon energy, despite some possible incomplete charge collection noise from photons absorbed in the substrate of the detector. The number of counts per second detected by the spectrometer was also found to be linearly dependent on the incident X-ray flux over the count rate range investigated. Although the energy resolutions achieved with this detector were not as good as some custom X-ray detectors (Bertuccio et al., 2011), its low cost and wide commercial availability, together with its ability to operate uncooled, and the visible blindness and radiation hardness of SiC, make it an interesting and potentially useful detector for numerous applications, including solar flare monitoring on board CubeSats.

The performance of the device as temperature tolerant electron detector was investigated by measuring the β^- generated current whilst the device was illuminated by a ^{63}Ni radioisotope β^- particle source. At the highest investigated reverse bias (100 V), the apparent β^- particle generated current in the 0.06 mm^2 photodiode was found to be 92 pA ± 1 pA at a temperature of 20 °C. However, doubt exists whether the extra current measured with the photodiode illuminated can be entirely attributed to the β^- particles, or if there was some increase in the leakage current component as well. The photodiode was connected to a custom-made low-noise charge-sensitive

preamplifier and found to function as electron spectrometer under the illumination of a ^{63}Ni radioisotope β^- particle source across the temperature range of 100 °C to 20 °C. The CASINO computer program was used to calculate the quantum efficiency of the photodiode assuming three different active region thicknesses (5.15 μm, 2.37 μm, and 34.5 μm). CASINO was also used to simulate the β^- particle spectra incident upon, and detected by, the photodiode. Agreement was found between the experimentally measured and simulated ^{63}Ni β^- particle spectra when a detector active region thickness of 5.15 μm was simulated. This suggests that the entire 5.15 μm thick epilayer is sensitive to β^- particles, but that β^- particles absorbed in the substrate are lost.

The results demonstrate that this type of low-cost COTS SiC photodiode can be coupled to a low-noise charge-sensitive preamplifier and standard signal processing electronics (a shaping amplifier and an MCA), to produce spectrometer which can detect electrons of energy up to 57 keV. This lays the foundations for university groups and other cost-sensitive organisations to use such devices as detectors for CubeSat space plasma physics missions.

Chapter 5 Soft X-ray Detection with $Al_{0.52}In_{0.48}P$ Mesa p^+-i-n^+ Photodiodes

5.1 Introduction

Chapters 3 and **4** demonstrated the capability of the commercially available 4H-SiC UV photodiodes repurposed as X-ray detectors. However, the limitations of this kind of COTS 4H-SiC UV photodiode repurposed as X-ray detectors are clear: they are thin (~5.15 μm epitaxial layer), 4H-SiC has relatively poor linear absorption coefficients, a relatively large electron-hole pair creation energy, and are only available as single pixels. As such, for space missions which have more financial and technical resources than are typically available for CubeSats, custom made detectors are desirable. Indeed, detectors better than those reported in **Chapters 3** and **4**, are not just desirable but necessary to achieve the science objective of some space missions, e.g. monitoring cosmic X-ray sources which with low X-ray fluxes (even the very bright X-ray source Sco X-1 provides only 150 photons cm^{-2} s^{-1} at the Earth's orbit (Paradijs & Bleeker, 1999)), and cutting-edge planetary geology performed via X-ray fluorescence spectroscopy (which can require energy resolutions $\approx$ 160 eV *FWHM* at 5.9 keV (Fraser, 2008)).

Recently, the wide bandgap semiconductor $Al_{0.52}In_{0.48}P$ (E_g = 2.31 eV at room temperature (Cheong et al., 2014)) has started to receive interest for use in X-ray spectroscopy. Auckloo et al. (2016) first reported using $Al_{0.52}In_{0.48}P$ avalanche photodiodes (1 μm thick avalanche layer) for soft X-ray spectroscopy and achieved an energy resolution (*FWHM* at 5.9 keV) of 682 eV at room temperature. A non-avalanche $Al_{0.52}In_{0.48}P$ detector (2 μm thick i layer) photon counting X-ray spectrometer was reported at room temperature soon after (Butera et al., 2016a), and then across the temperature range 100 °C to -20 °C (Butera et al., 2016a). Energy resolutions (*FWHM* at 5.9 keV) of 0.90 keV at 20°C and 1.57 keV at 100 °C were achieved with the non-avalanche detectors. Prior to the work reported in this thesis these 2 μm thick detectors were the thickest $Al_{0.52}In_{0.48}P$ structures reported for X-ray spectroscopy.

In this chapter, in contrast to the high technology readiness level 4H-SiC detectors investigated in **Chapters 3** and **4**, new work is reported from the very cutting-edge of semiconductor materials development for future X-ray detectors. For four $Al_{0.52}In_{0.48}P$ mesa p^+-i-n^+ photodiodes with i layer thicknesses of 6 μm and diameters of 217 μm ± 15 μm (D1 and D2) and 409 μm ± 28 μm (D3 and D4) (see **Sections 5.2** and **5.3**) at room temperature. The detectors were electrically characterised and then investigated for their soft X-ray detection performance. One of the

217 µm ± 15 µm diameter photodiodes (D2) and one of the 409 µm ± 28 µm diameter photodiodes (D4) were then further characterised at the temperatures up to 100 °C (see **Sections 5.4** and **5.5**).

Whilst it is of lower technology readiness level than 4H-SiC, $Al_{0.52}In_{0.48}P$ has a higher quantum detection efficiency for a given detector thickness due to its greater linear absorption coefficients (e.g. 1302 cm^{-1} for $Al_{0.52}In_{0.48}P$ cf. 346 cm^{-1} for 4H-SiC, at 5.9 keV) and an ultimately better Fano-limited energy resolution (see **Equation 2.12**) as a consequence of its smaller electron-hole pair creation energy (5.34 eV for $Al_{0.52}In_{0.48}P$ cf. 7.8 eV for 4H-SiC, at room temperature) (Bertuccio et al., 2011) (Butera et al., 2018b). The lower electron-hole pair creation energy also places less stringent demands on the spectrometer charge-sensitive preamplifier electronics because the average signal charge for a photon of given X-ray energy will be greater in $Al_{0.52}In_{0.48}P$ than 4H-SiC (e.g. 1104 electron-hole pairs in $Al_{0.52}In_{0.48}P$ cf. 756 electron-hole pairs in 4H-SiC, for a 5.9 keV X-ray). Furthermore, since the $Al_{0.52}In_{0.48}P$ photodiodes are custom-made, in principle the thickness of the epilayers can also be increased as material technology improves, and monolithic pixel arrays can also be produced.

5.2 Electrical characterisation at room temperature

5.2.1 Capacitance-voltage measurements

The capacitances of $Al_{0.52}In_{0.48}P$ photodiodes D1 and D2 (217 µm ± 15 µm diameter) and D3 and D4 (409 µm ± 28 µm diameter) were measured in a dry N_2 environment (relative humidity < 5%) at room temperature (24 °C) (see **Section 2.9**). Each photodiode was reverse biased up to 100 V, with increments of 1 V. The capacitance of the device's package was estimated by measuring the capacitances between the empty pins on the package (pins without photodiodes connected to them) and the common pin of the package, it was found to be 0.84 pF ± 0.05 pF. In order to find the capacitance of the device itself, the capacitance of the device's package was subtracted from the measured capacitance of the packaged device. The depletion width of each photodiode was considered to be given by **Equation 2.3**.

The capacitances and the associated depletion widths of the photodiodes as functions of applied reverse bias are shown in **Figures 5.1** and **5.2**, respectively. The capacitance densities of these photodiodes were found to be similar across the investigated biases and to become relatively constant (5 pF/mm^2 ± 1 pF/mm^2) at high reverse biases (> 80 V). At 100 V reverse bias, the capacitances of the 217 µm diameter photodiodes (D1 and D2) were found to be 0.71 pF ± 0.07 pF

and 0.66 pF ± 0.07 pF, respectively; and the capacitances of the 409 µm diameter photodiodes (D3 and D4) were found to be 2.48 pF ± 0.09 pF and 2.49 pF ± 0.09 pF, respectively.

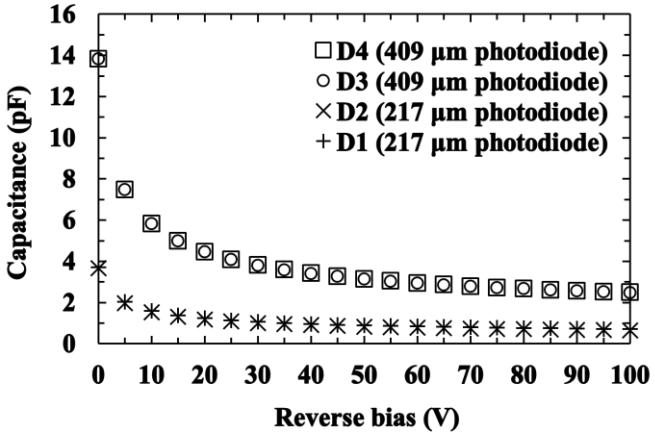

Figure 5.1. Measured capacitances of the $Al_{0.52}In_{0.48}P$ p^+-i-n^+ mesa photodiodes, 217 µm diameter photodiode (D1, + symbols; D2, × symbols); 409 µm diameter photodiode (D3, open circles; D4, open squares), as functions of applied reverse bias at room temperature (24 °C).

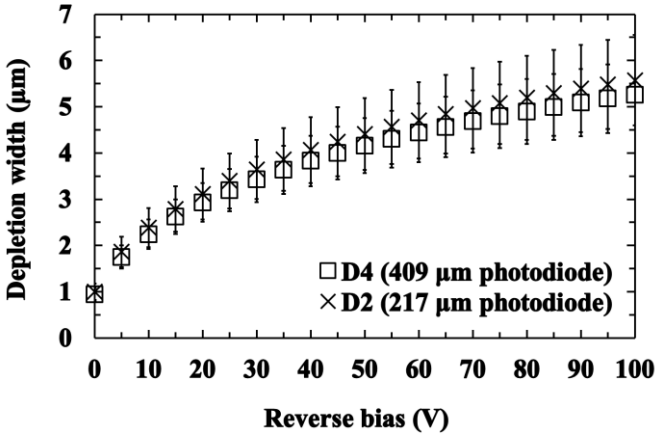

Figure 5.2. Calculated depletion width of the $Al_{0.52}In_{0.48}P$ p^+-i-n^+ mesa photodiodes as functions of applied reverse bias at room temperature (24 °C). 217 µm diameter photodiode D2 (× symbols); 409 µm diameter photodiode D4 (open squares). For clarity, only data for one photodiode of each size are shown, but comparable results were obtained for the other devices.

At the highest investigated reverse bias (100 V), the calculated depletion widths and associated uncertainties (including the error in the diameter of these photodiodes, the uncertainties in the capacitance measurements, and the Debye length) of the photodiodes were found to be 5.13 µm ± 0.87 µm and 5.57 µm ± 0.98 µm for the 217 µm diameter photodiodes (D1 and D2), and 5.26 µm ± 0.75 µm and 5.26 µm ± 0.75 µm for the 409 µm diameter photodiodes (D3 and

D4). Reduction of capacitance with increasing reverse bias became insignificant at reverse biases > 80 V. These devices have a thicker depletion region than previously reported $Al_{0.52}In_{0.48}P$ X-ray detectors which had i layer thicknesses of 0.5 µm with an avalanche layer thickness of 1 µm (Auckloo et al., 2016), and i layer thicknesses of 2 µm (Butera et al., 2016a).

Since the surfaces of the photodiodes were partially covered by the Ohmic annular contacts (see **Section 1.9.2**), the weighted quantum efficiency (considering the areas covered and uncovered by the contacts) for the devices were calculated using the Beer-Lambert law, and assuming 100% charge collection in the epitaxial p and i layers. The weighted quantum efficiencies as functions of incident X-ray energy for D1 and D2 (217 µm diameter photodiodes) and D3 and D4 (409 µm diameter photodiodes) are presented in **Figure 5.3**. The weighted quantum efficiencies of the photodiodes were calculated to be 0.529 at 5.9 keV and 0.450 at 6.49 keV for D1 and D2, and 0.535 at 5.9 keV and 0.454 at 6.49 keV for D3 and D4.

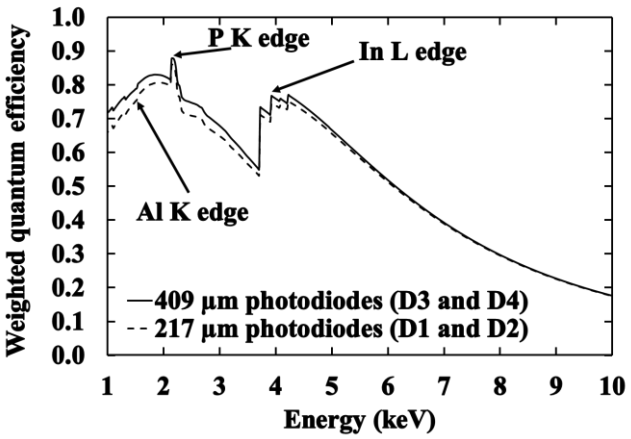

Figure 5.3. Calculated weighted quantum efficiencies of the $Al_{0.52}In_{0.48}P$ p^+-i-n^+ mesa photodiodes as functions of X-ray photon energy: D1 and D2 (217 µm diameter photodiodes, dashed line); D3 and D4 (409 µm diameter photodiodes, solid line). The discontinuities are the Al K, P K, and In L X-ray absorption edges.

5.2.2 Current-voltage measurements

Leakage currents as functions of applied reverse bias for D1 – D4 were measured in dark condition in a dry N_2 environment (relative humidity < 5%) at room temperature (24 °C) (see **Section 2.8**). Each photodiode was reverse biased from 0 V to 100 V, in increments of 1 V. Low leakage currents (< 3.0 pA ± 0.4 pA) (including the package's leakage current) were found for all the photodiodes even at high reverse bias (100 V), as shown in **Figure 5.4**. The leakage current associated with the package itself was estimated by measuring the leakage current of an empty

pin on the same package and common pin of the package. The package's leakage current was found to be less than the picoammeter's uncertainty (0.4 pA). Hence, the package's leakage current was considered to be negligible.

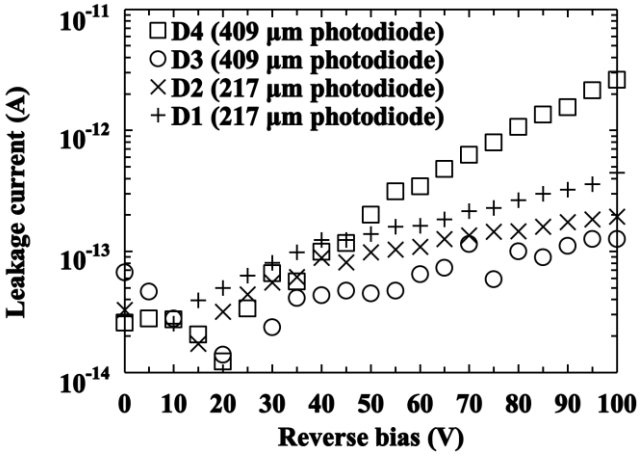

Figure 5.4. Leakage currents as functions of applied reverse bias for the $Al_{0.52}In_{0.48}P$ p^+-i-n^+ mesa photodiodes, 217 µm diameter photodiodes (D1, + symbols; D2, × symbols); 409 µm diameter photodiodes (D3, open circles; D4, open squares), at room temperature (24 °C).

At 40 V reverse bias (electric field strength ≈ 105 kV/cm), the leakage current densities of the $Al_{0.52}In_{0.48}P$ photodiodes (217 µm diameter devices, D1 = 0.34 nA/cm^2, D2 = 0.24 nA/cm^2; 409 µm diameter devices, D3 = 0.03 nA/cm^2, D4 = 0.08 nA/cm^2) were greater than has been reported with custom-made SiC X-ray detectors (e.g. 1 pA/cm^2 at an electric field strength of 103 kV/cm at room temperature (Bertuccio et al., 2011) but comparable to the leakage current densities reported with commercially available SiC UV detectors (1.2 nA/cm^2 at electric field strength of 227 kV/cm at room temperature (see **Section 3.2.2**). In contrast, the leakage currents of the $Al_{0.52}In_{0.48}P$ photodiodes were lower than has been reported for semi-insulating SiC X-ray photodiodes (65 nA/cm^2 with internal electric field of 28 kV/cm at room temperature (Bertuccio et al., 2013b)) and $Al_{0.8}Ga_{0.2}As$ photodiodes (4.72 nA/cm^2 with an electric field of 29 kV/cm at room temperature (Barnett et al., 2015).

5.3 X-ray spectroscopy and noise analysis at room temperature

5.3.1 Photon counting spectroscopy with ^{55}Fe radioisotope X-ray source

The photodiodes D1 – D4 were each in turn soldered to a wire-ended packaged silicon input JFET (2N4416A, capacitance = 2 pF) which was the first transistor of a custom-made low-noise

charge-sensitive preamplifier of feedback resistorless design (Bertuccio et al., 1993). An ORTEC 572A shaping amplifier and an ORTEC EASY-MCA 8k multi-channel analyser (MCA) were connected to the preamplifier (see **Section 2.11**). The photodiodes were each in turn illuminated with an ^{55}Fe radioisotope X-ray source (Mn Kα = 5.9 keV; Mn Kβ = 6.49 keV; activity = 175 MBq). The ^{55}Fe radioisotope X-ray source was placed 4 mm above the 217 μm diameter photodiodes and 10 mm above the 409 μm diameter photodiodes. In each case, the system was investigated at six different shaping times (0.5 μs, 1 μs, 2 μs, 3 μs, 6 μs, and 10 μs) with each photodiode reverse biased at 0 V, 10 V, 20 V, 30 V, 40 V, 60 V, 80 V, and 100 V. Each spectrum was accumulated for 240 s. The photodiodes and the preamplifier were operated at room temperature (24 °C) in a dry N_2 environment (relative humidity < 5%).

The resulting spectra were calibrated in energy terms by using the positions of the zero energy noise peak and the fitted Mn Kα peak at 5.9 keV for each spectrum as points of known energies on MCA's charge scale, and assuming a linear variation of detected charge with energy. The energy resolutions (*FWHM* at 5.9 keV) of the systems as functions of shaping times are shown for a detector reverse bias of 100 V in **Figure 5.5**. The best energy resolutions of the 217 μm diameter photodiode (D2) and 409 μm diameter photodiodes (D4) at each reverse bias are presented in **Figure 5.6**. *FWHM* at 5.9 keV as good as 0.89 keV ± 0.04 keV and 1.05 keV ± 0.08 keV were found for the 217 μm diameter photodiode (D2) and the 409 μm diameter photodiode (D4), respectively, at 100 V reverse bias. **Figure 5.7** shows the spectra obtained with each photodiode at the best shaping time when reverse biased 10 V, 20 V, 40 V, and 100 V.

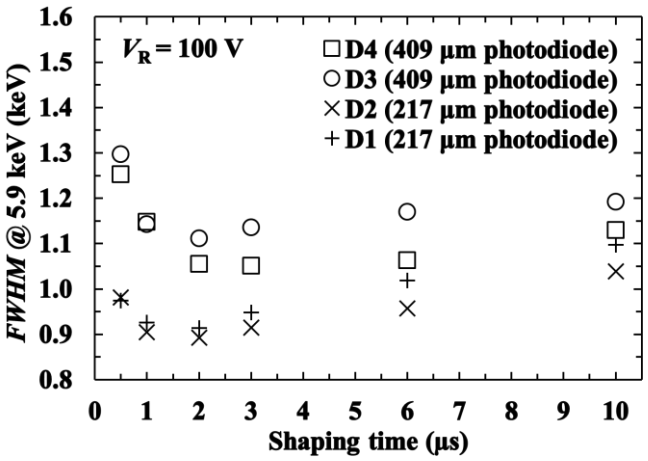

Figure 5.5. Measured *FWHM* at 5.9 keV as a function of shaping time when the photodiodes were operated at an applied reverse bias of 100 V: 217 µm diameter photodiodes D1 (+ symbols) and D2 (× symbols); 409 µm diameter photodiodes D3 (open circles) and D4 (open squares).

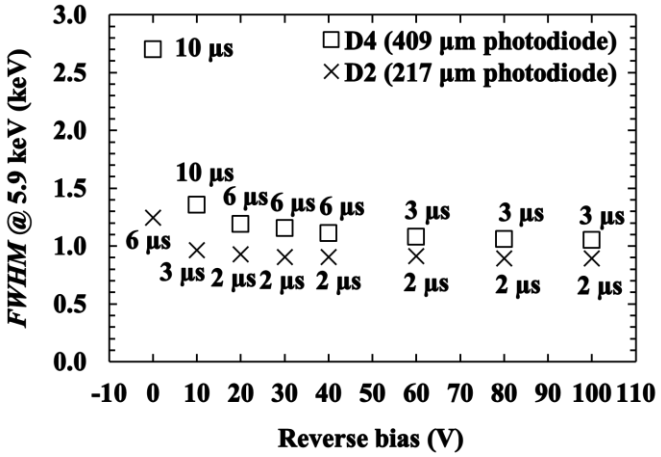

Figure 5.6. Measured *FWHM* at 5.9 keV of one of the 217 µm diameter photodiodes (D2, × symbols), and one of the 409 µm diameter photodiodes (D4, open squares), as functions of applied reverse bias at the optimum shaping time.

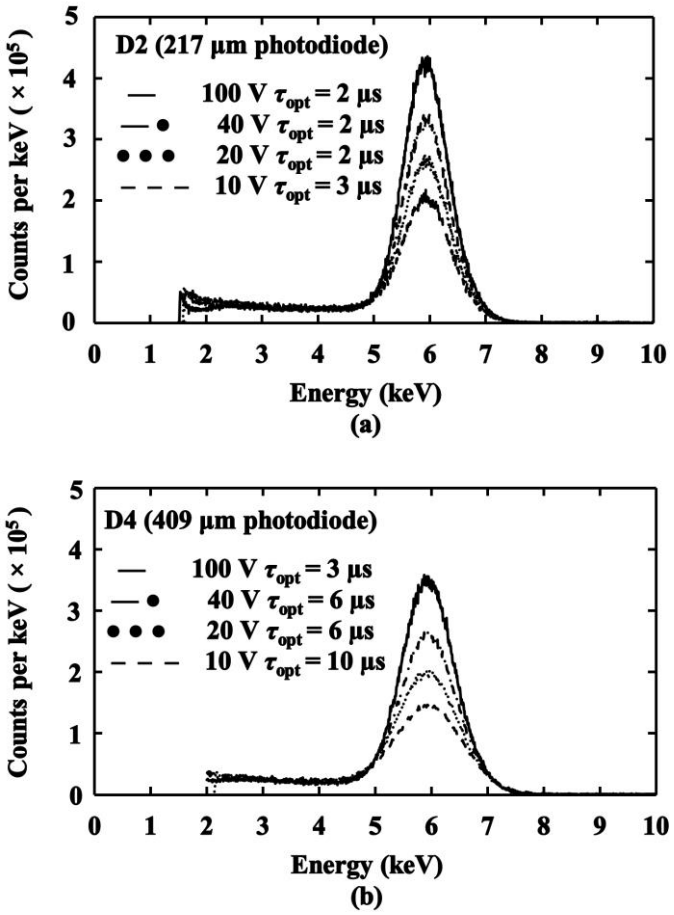

Figure 5.7. ^{55}Fe X-ray spectra obtained with (a) one of 217 µm diameter photodiodes (D2), (b) one of 409 µm diameter photodiodes (D4), at varying reverse biases (for clarity only 10 V, dash line; 20 V, dot line; 40 V, dash dot line; 100 V, solid line, are shown). The shaping time which gave the best energy resolution was selected at each reverse bias. The *FWHM* at 5.9 keV of D2 were 0.89 keV, 0.91 keV, 0.93 keV, and 0.97 keV at the reverse bias of 100 V, 40 V, 20 V, and 10 V, respectively. The *FWHM* at 5.9 keV of D4 were 1.05 keV, 1.11 keV, 1.19 keV, and 1.36 keV at the reverse bias of 100 V, 40 V, 20 V, and 10 V, respectively.

The energy resolutions obtained (0.89 keV and 1.05 keV at 5.9 keV, for the 217 µm and 409 µm diameter detectors, respectively) were not as good as some of those obtained using other wide bandgap X-ray photodiodes at room temperature. For example, a 200 µm diameter GaAs mesa photodiode spectrometer had a *FWHM* at 5.9 keV of 745 eV (Lioliou et al., 2016a), and a 200 µm × 200 µm SiC X-ray pixel detector had a *FHWM* at 5.9 keV of 196 eV at 30 °C when coupled to lower noise readout electronics (Bertuccio et al., 2011). However, the energy resolutions achieved with these AlInP devices are better than those previously reported for 2 µm i layer AlInP mesa devices (0.93 keV for a 200 µm diameter photodiode; 1.2 keV for a 400 µm diameter photodiodes (Butera et al., 2016a). They are also better than has been reported with

some other custom wide bandgap photodiodes, e.g. AlGaAs (1.07 keV at 20 °C for a 200 µm diameter diode (Barnett et al., 2010), 1.06 keV at 20 °C for a 200 µm diameter photodiode (Whitaker et al., 2017)). A shaping time noise analysis is presented in **Section 5.3.2**.

The valley-to-peak (V/P) ratio (as defined as the ratio between the number of counts at 4.1 keV and 5.9 keV) at the optimum shaping time and the greatest investigated reverse bias (100 V) were 0.048 and 0.058 for the 217 µm diameter photodiode (D2) and the 409 µm diameter photodiode (D4), respectively. These are not as good as those reported for cooled silicon DEPFET detectors (V/P = ~0.0001) (Lutz, 2006) and GaAs detectors (V/P = 0.03) (Lioliou & Barnett, 2016), but better than those of some AlGaAs photodiodes (V/P = 0.08 (Barnett et al., 2015) (Whitaker et al., 2017)). The low energy tail of the photopeak which gives rise to the valley is a consequence of the partial collection of charge created by X-ray photons absorbed in the semiconductor layers often assumed to be inactive (e.g. substrate) (Barnett et al., 2015). The V/P ratio is therefore expected to improve as AlInP detectors with thicker i layers are grown.

Figure 5.8 shows how the number of counts in the 5.9 keV photopeak changed as the reverse bias was increased. The number of counts was found to increase from 5.79×10^6 at 0 V reverse bias to 5.94×10^7 at 100 V reverse bias for the 217 µm diameter photodiode (D2), and from 3.40×10^6 at 0 V reverse bias to 4.39×10^7 at 100 V reverse bias for the 409 µm diameter photodiode (D4).

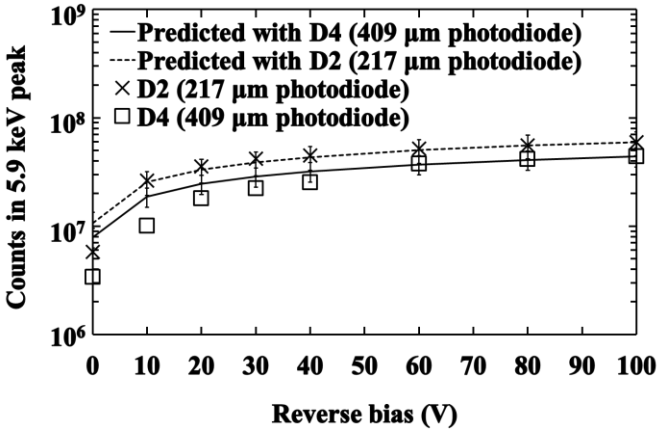

Figure 5.8. Number of counts in the 5.9 keV photopeak for one of 217 µm diameter photodiodes (D2, × symbols) and one of 409 µm diameter photodiodes (D4, open squares) at different reverse biases as a function of reverse bias, and at the optimum shaping time in each case. Also shown are the predicted numbers of counts expected to be detected where that prediction is based on the measured width of the deletion region as a function of applied bias and the implied relative detection efficiency compared to that at 100 V (D2, dashed line; D4, solid line).

The relative number of counts predicted to be detected at each applied reverse bias (as defined by the number of counts in the 5.9 keV photopeak, and relative to the number of counts experimentally detected in the peak at an applied reverse bias of 100 V) was calculated for both photodiodes, in order to explore the cause of the observed change in the number of detected counts as a function of applied reverse bias (see **Figure 5.8**). The predictions of numbers of detected counts were made assuming that there was complete charge collection across the bias range, and that the measured variation in the thickness of each photodiode's depletion region as function of reverse bias was the sole contributing factor to variation in numbers of detected counts for that photodiode. The results of this work can be seen in **Figure 5.8** where the predictions are presented for comparison with the experimental data. The uncertainties (error bars) in the predictions shown in the figure reflect the uncertainties in the photodiodes' calculated depletion widths at each reverse bias. Agreement was found between the experimental and predicted numbers of counts at high reverse biases ($\geqslant$ 10 V for D2; $\geqslant$ 60 V for D4). Therefore, it is interpreted from this that at these reverse biases, the change in number of experimentally detected counts as a function of applied bias for each photodiode was a result of the changes in the depletion width as a function of reverse bias. At low reverse biases (< 10 V for D2 and < 60 V for D4), the disagreement between the experimental and predicted numbers of counts may be due to incomplete charge collection as a consequence of the low internal electric fields present in these bias conditions.

5.3.2 Noise analysis

The energy resolution of a photodiode X-ray spectrometer is the result of contributions from three noise components: Fano noise; electronic noise from the detector and the preamplifier; and incomplete charge collection noise (Owens, 2012). The Fano noise is determined by the statistical fluctuations in the number of the electron-hole pairs created in the process of photon absorption (Owens, 2012). The expected Fano-limited resolution ($FWHM_{Fano}$) of the $Al_{0.52}In_{0.48}P$ photodiode can be estimated to be 145 eV at 5.9 keV, assuming an electron-hole pair creation energy of 5.34 eV (Butera et al., 2018b), and a Fano factor of 0.12 (it should be noted that there has been no reported measurement of the Fano factor in $Al_{0.52}In_{0.48}P$ to date). The electronic noise includes the series white noise, induced gate drain current noise, parallel white noise, 1/*f* series noise, and dielectric noise (Owens, 2012); explanations of the origin of each electronic noise component can be found in Bertuccio et al. (1996) and Lioliou & Barnett (2015). The noise components were calculated as per Bertuccio et al. (1996). Incomplete charge collection is related to the trap density distribution and the charge diffusion and collection properties of the detector (Owens, 2012).

The series white noise including induced gate current noise, 1/*f* series noise, and dielectric noise are related to the total capacitance at the input of the preamplifier. The parallel white noise is related to the leakage current of the detector and the leakage current of the input JFET. A longer shaping time can reduce the series white noise including induced gate current noise and increase the parallel white noise. The 1/*f* series noise and dielectric noise are independent of shaping time (Bertuccio et al., 1996). The quadratic sum of the dielectric noise and incomplete charge collection noise can be estimated by subtracting (in quadrature) the calculated series white noise (including induced gate current noise), parallel white noise, 1/*f* series noise, and the predicted Fano noise in quadrature from the measured *FWHM* at 5.9 keV. The calculated noise contributions for one of the 217 µm diameter devices (D2) and one of the 409 µm diameter devices (D4) as functions of shaping time at 100 V reverse bias are shown in **Figure 5.9**. **Figure 5.9** also shows the quadratic sum of the dielectric noise and incomplete charge collection noise; this combination is the dominant contributor to the total noise of the systems, and it is relatively constant at all the investigated shaping times. At 100 V reverse bias, the best *FWHM* for the 217 µm diameter photodiode (D2) and the 409 µm diameter photodiode (D4) were found at with shaping time of 2 µs and 3 µs, respectively. For the 217 µm diameter photodiodes, the series white noise dominates all other noise components except the combination of the dielectric and incomplete charge collection noise; at shaping time > 2 µs the same can be said for the parallel white noise. For the 409 µm photodiodes, 3 µs is the shaping time at which dominance shifts

between the white series and white parallel noise components.

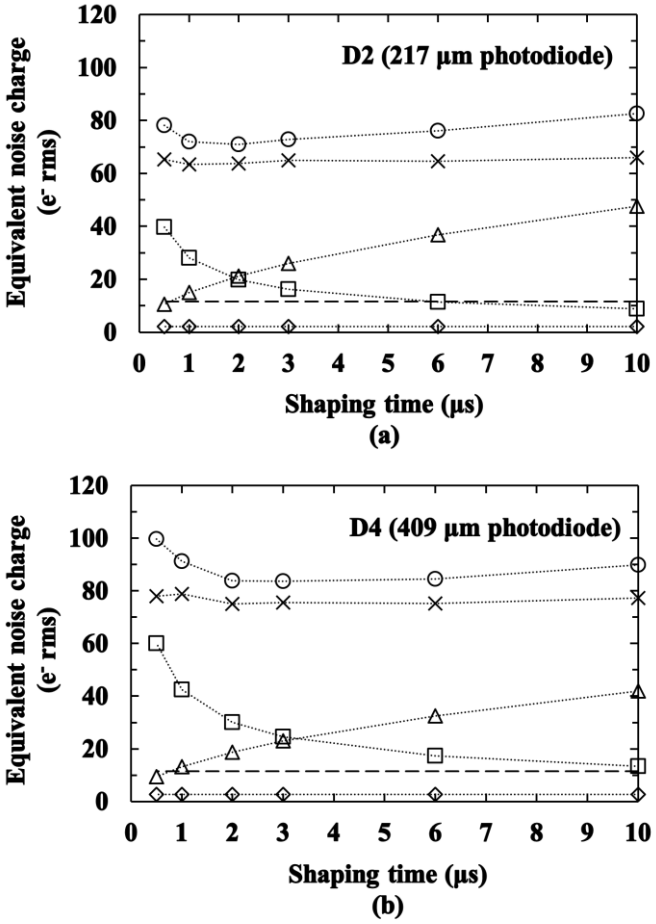

Figure 5.9. Equivalent noise charge at 5.9 keV for (a) a 217 µm diameter photodiode (D2) and (b) a 409 µm diameter photodiode (D4) as a function of shaping time at 100 V reverse bias at 24 °C. The measured *FWHM* at 5.9 keV (circles), the quadratic sum of the dielectric noise and incomplete charge collection noise (× symbols), the series white noise including induced gate current noise (squares), the parallel white noise (triangles), the Fano noise (dash line), and the 1/*f* series noise (diamonds). The dotted lines are guides for the eyes only.

It is interesting to further consider the dielectric noise and the incomplete charge collection noise such that their respective contributions can be established. As such, the quadratic sum of dielectric noise and incomplete charge collection noise of a 217 µm diameter device (D2) and a 409 µm diameter device (D4) were analysed as a function of applied reverse bias at a fixed shaping time of 3 µs, as shown in **Figure 5.10**. A reduction in this equivalent noise charge with increased detector bias can be due to the either a reduction of the system capacitance or a reduction in the incomplete charge collection noise as a consequence of improved charge transport at higher electric field, or both.

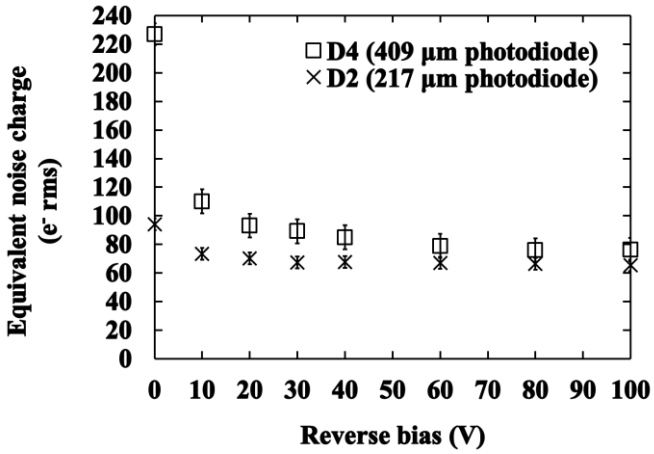

Figure 5.10. Computed quadratic sum of dielectric noise and incomplete charge collection noise for the 217 µm diameter photodiode spectrometer D2 (× symbol) and the 409 µm diameter photodiode spectrometer (D4) (open squares) as functions of applied reverse bias at a shaping time of 3 µs.

At high reverse biases (≥ 80 V), the change in the capacitances and the associated depletion widths of these devices were insignificant (see **Figures 5.1** and **5.2**), hence, the dielectric noise of each device is expected to be constant since the dielectric noise is related to the capacitance (see **Equation 2.19**). From **Figure 5.10**, the constant equivalent noise charge at ≥ 80 V demonstrates that was no significant contribution from incomplete charge collection noise in this bias condition because there was no reduction in the combination as the bias was increased beyond 80 V. As such, the quadratic sum in these conditions can be said to be solely composed of dielectric noise, which is independent of bias and shaping time.

Given these statements, for each spectrometer separately, it is possible to consider any small apparent variations in dielectric noise which may occur with varied shaping time, as arising from repetition in measurement of the same physical quantity rather than real physical differences in dielectric noise – so long as each detector is reverse biased at ≥ 80 V. This then provides six measurements at each reverse bias ≥ 80 V of the same dielectric noise for each spectrometer. There are six measurements because six shaping times were used. These six measurements, the computed dielectric noises, for a 217 µm diameter photodiode spectrometer (D2) and a 409 µm diameter photodiode spectrometer (D4) at reverse bias of 80 V and 100 V, respectively, are shown in **Figure 5.11**.

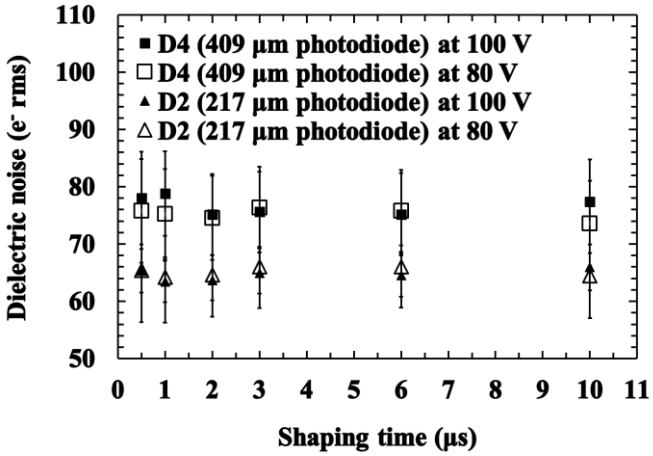

Figure 5.11. Computed dielectric noises as a function of shaping time for the 217 µm diameter photodiode spectrometer D2 (solid triangles and open triangles at reverse bias of 100 V and 80 V, respectively) and 409 µm diameter photodiode spectrometer D4 (solid squares and open squares at reverse bias of 100 V and 80 V, respectively).

Since the dielectric noises of D2 spectrometer, ENC_{DT217}, and D4 spectrometer, ENC_{DT409}, each consists of the dielectric noises of their respective detectors (ENC_{D217} for 217 µm diameter photodiode and ENC_{D409} for 409 µm diameter photodiode), and some other system dielectric noise which is common between both spectrometers, the dielectric dissipation factor (see **Equation 2.19**) of $Al_{0.52}In_{0.48}P$ can be estimated. First the common system dielectric noise, ENC_{Dx}, must be considered, it is given by,

$$ENC_{Dx}{}^2 = ENC_{DT217}{}^2 - ENC_{D217}{}^2 = ENC_{DT409}{}^2 - ENC_{D409}{}^2 \quad (5.1)$$

where all terms have been previously defined.

Following this, since the variation in the dielectric noise between the detectors themselves is solely due to the difference in their capacitances (**Equation 2.19**), the relationship between ENC_{D217} and ENC_{D409} can be expressed as,

$$\frac{ENC_{D217}}{ENC_{D409}} = \sqrt{\frac{C_{217}}{C_{409}}} \quad (5.2)$$

where C_{217} and C_{409} are the capacitances of the 217 µm diameter photodiode (0.72 pF and 0.67 pF at reverse bias of 80 V and 100 V, respectively) and 409 µm diameter photodiode (2.68 pF and 2.50 pF at reverse bias of 80 V and 100 V, respectively).

Thus, by combining **Equation 2.19**, **Equation 5.1**, and **Equation 5.2**, and considering all the data at 80 V and 100 V, the dielectric dissipation factor of $Al_{0.52}In_{0.48}P$ was estimated to be

$(2.2 \pm 1.1) \times 10^{-3}$. This value is smaller than that reported for $In_{0.5}Ga_{0.5}P$ (6.5×10^{-3}) (Butera et al., 2017) but larger than Si (0.8×10^{-3}) (Bertuccio & Casiraghi, 2003), GaAs (0.1×10^{-3}) (Krupka et al., 2008), and 4H-SiC (3.4×10^{-5}) (Jung et al., 2014).

In a feedback resistorless charge-sensitive preamplifier the current of the detector in part sets the bias of the forward biased input JFET (Bertuccio et al., 1993), which in turn influences the JFET's capacitance. The above determination is predicated on the assumption that the variation in detector leakage current between the 217 µm and 409 µm diameter photodiodes and in operating the detectors at biases of 80 V and 100 V, is sufficiently small that the capacitance of the JFET is not substantially changed. Given the low leakage currents of the detectors (< 3 pA), it is believed that the assumption is valid.

5.4 Electrical characterisation at high temperature

5.4.1 Capacitance-voltage measurements

The capacitances of D2 (217 µm diameter) and D4 (409 µm diameter) as functions of applied reverse were measured at different temperatures, using an HP 4275A Multi Frequency LCR meter and a Keithley 6487 Picoammeter/Voltage Source (see **Section 2.9**). Before starting the measurements at each temperature, each device was allowed to stabilise for 30 min to achieve thermal equilibrium. The devices' capacitances as functions of applied reverse bias were measured from 100 °C to 0 °C, with a decrement step of 20 °C. Because the photodiodes were packaged in a TO-5 can, the capacitance between an empty pin on the package (a pin without a wire-bonded device) and the common pin of the package was used to estimate the capacitance contribution of the packaging. The package capacitance was found to be temperature independent within the investigated temperature range. The capacitance of each photodiode was calculated by subtracting the capacitance of the package (0.80 pF ± 0.05 pF) from the total measured capacitance of the packaged device. The devices' capacitances (packaging subtracted), and the calculated depletion widths of the photodiodes as functions of applied reverse bias at 100 °C and 0 °C, are presented in **Figure 5.12**. At the highest investigated temperature (100 °C) and reverse bias (100 V), the capacitances of D2 (217 µm diameter) and D4 (409 µm diameter) were found to be 0.67 pF ± 0.07 pF (corresponding capacitance density of 2.2 nF/cm^2 ± 0.3 nF/cm^2) and 2.54 pF ± 0.09 pF (corresponding capacitance density of 1.9 nF/cm^2 ± 0.2 nF/cm^2), respectively. The uncertainties reflect an experimental repeatability uncertainty (± 0.07 pF) and the measurement uncertainty (~0.1%) of the LCR meter. At high reverse biases (≥ 80 V), the

reduction in the capacitance with increased applied reverse bias was found to be negligible within the uncertainties. Therefore, the photodiodes were considered to be fully depleted at 80 V reverse bias. The calculated depletion widths of the 217 µm diameter photodiode at 100 V reverse bias were found to be 5.5 µm ± 0.7 µm at 100 °C and 5.7 µm ± 0.8 µm at 0 °C, respectively. At 100 V reverse bias, the calculated depletion widths of the 409 µm diameter photodiode were respectively found to be 5.1 µm ± 0.5 µm at 100 °C and 5.2 µm ± 0.5 µm at 0 °C. The uncertainties in the depletion widths were calculated by taking into account the uncertainties in the diameters, the uncertainties in the capacitance measurements, and the Debye length (Sze & Ng, 2007). The capacitances of each photodiode as functions of temperature at different reverse biases (0 V, 1 V, 2 V, 3 V, 4 V, 5 V, 10 V, 20 V, 40 V, 60 V, and 100 V) are presented in **Figure 5.13**. This figure shows that the temperature dependence of each photodiode's capacitance became insignificant at reverse biases > 5 V.

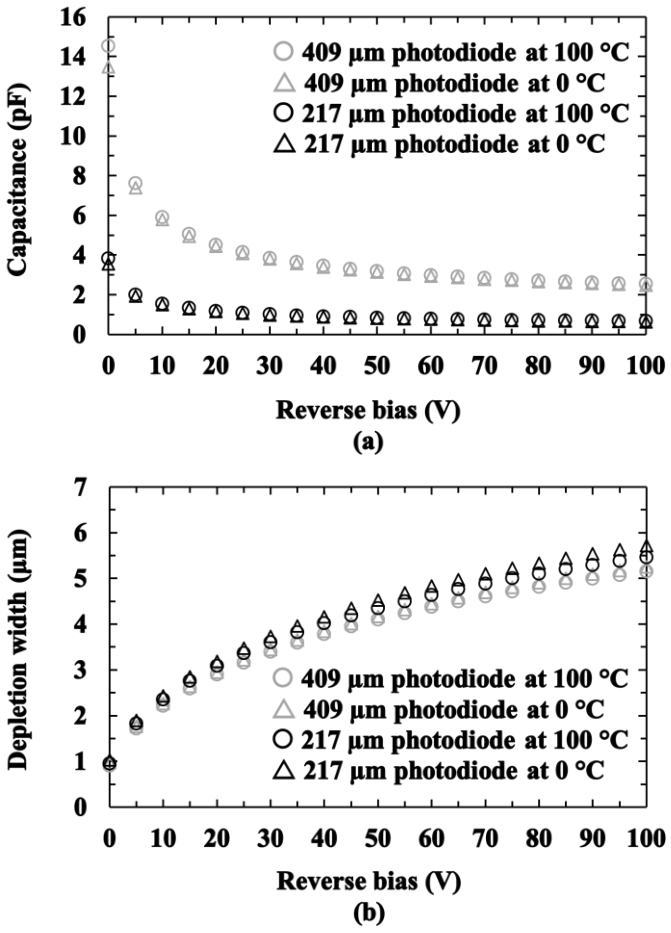

Figure 5.12. (a) Measured capacitances and (b) calculated depletion widths as functions of applied reverse bias for D2 (217 µm diameter photodiode) (100 °C, black open circles; 0 °C, black open triangles) and D4 (409 µm diameter photodiode) (100 °C, grey open circles; 0 °C, grey open triangles).

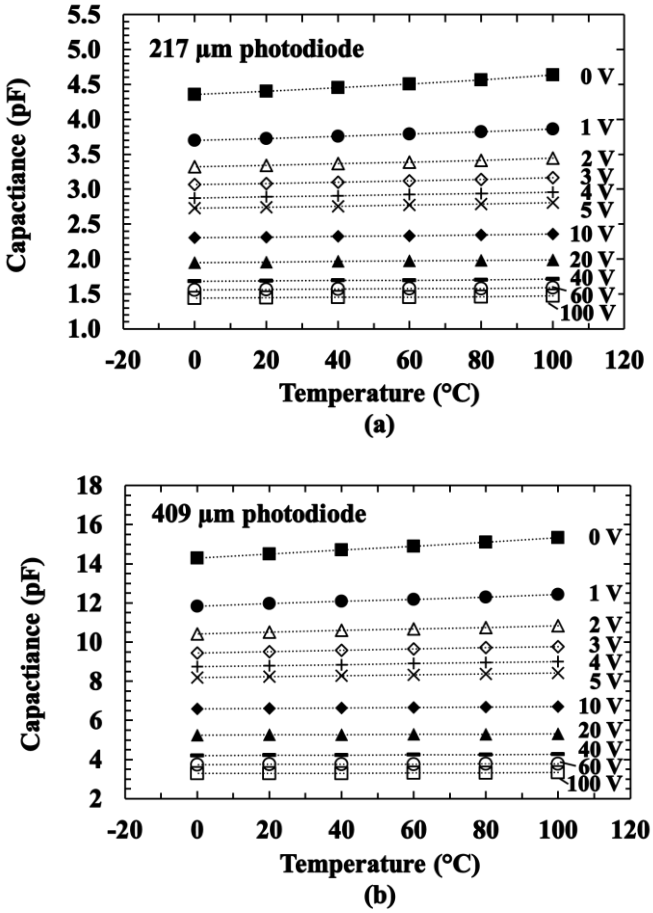

Figure 5.13. Capacitances as functions of temperature for (a) D2 (217 µm diameter photodiode) and (b) D4 (409 µm diameter photodiode) in the temperature range of 0 °C to 100 °C at varying applied reverse biases, 0 V (dark squares), 1 V (dark circles), 2 V (open triangles), 3 V (open diamonds), 4 V (+ symbols), 5 V (× symbols), 10 V (dark diamonds), 20 V (dark triangles), 40 V (dashes), 60 V (open circles), 100 V (open squares). The lines between the experimental data points (dotted lines) are guides for the eyes only.

5.4.2 Current-voltage measurements

The leakage currents of the two detectors were measured as functions of applied reverse bias across the temperatures range 100 °C to 0 °C using the same climatic procedure as was employed for the capacitance measurements. A Keithley 6487 Picoammeter/Voltage Source was used to reverse bias the devices from 0 V to 100 V, in steps of 1 V, and measure the resultant current (see **Section 2.8**). The leakage current of the package, i.e. the leakage current between an empty pin (a pin without a wire-bonded device) and the common pin of the package, was also measured. The results showed that the leakage currents of the package itself and the packaged devices (including the leakage current of the package and the photodiodes) increased with increasing

temperature, as presented in **Figure 5.14**. The leakage current of the package was found to be the dominant contributor to the leakage currents for both packaged devices. As such, comparable leakage currents were measured for both devices, at each applied reverse bias and temperature. At the highest investigated temperature (100 °C) and 100 V reverse bias (electric field strength = 167 kV/cm), the leakage currents of the packaged 217 µm diameter device, D2, (including package leakage), and the packaged 409 µm diameter device, D4, (including package leakage) were found to be 8.3 pA ± 0.4 pA and 10.5 pA ± 0.4 pA, respectively. The leakage current contribution to these values from the package was 6.1 pA ± 0.4 pA. At temperatures < 60 °C the leakage currents were smaller than the uncertainty of the measuring system (± 0.4 pA).

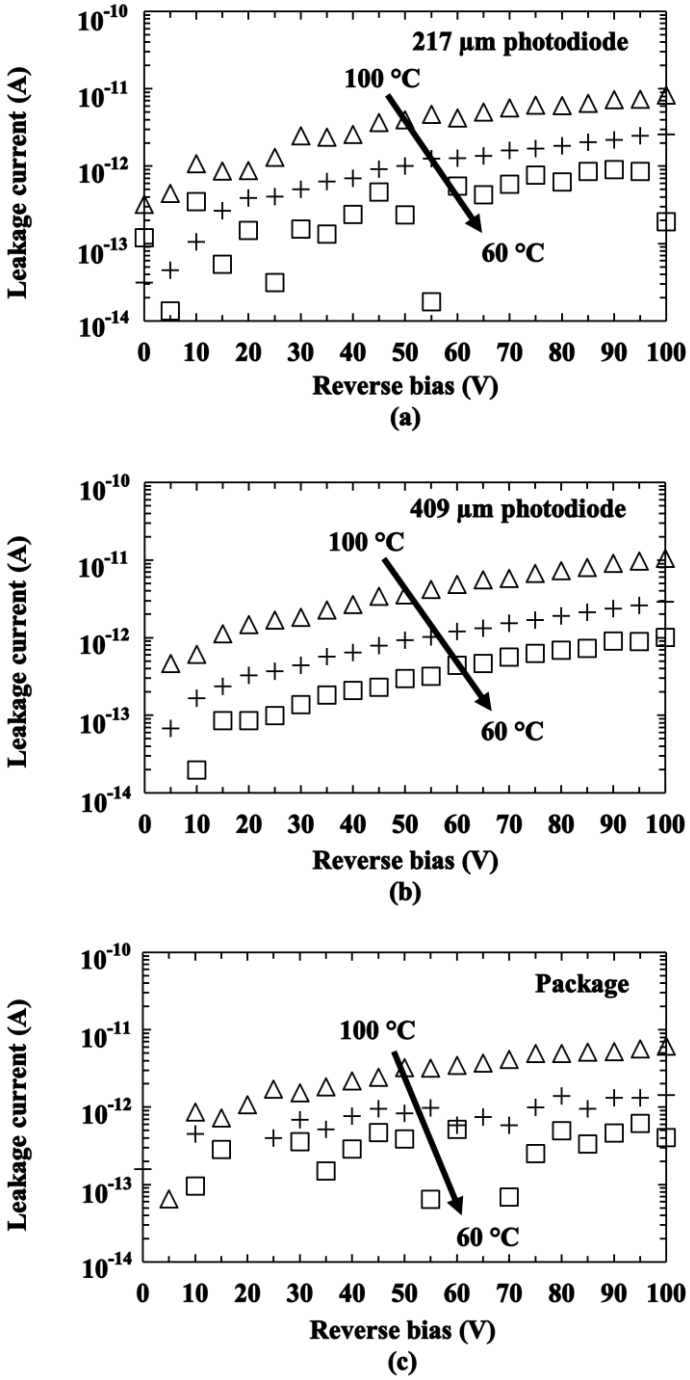

Figure 5.14. Leakage currents as functions of reverse bias for (a) packaged 217 µm diameter detector, D2, (including package leakage), (b) packaged 409 µm diameter detector, D4, (including package leakage), and (c) the measured leakage current contribution in (a) and (b) from the package itself (as measured using a package pin without a wire bonded device). In each case the measurements are shown at temperatures of 100 °C, 80 °C, and 60 °C. At temperatures < 60 °C, the currents were too small to be reliable measured using the available experimental set up.

5.5 X-ray spectroscopy and noise analysis at high temperature

5.5.1 Photon counting spectroscopy with an ^{55}Fe radioisotope X-ray source

To characterise the detectors' responses to illumination with X-rays, each of the detectors was in turn coupled to a custom-made low-noise charge-sensitive feedback resistorless preamplifier (similar to that reported in Bertuccio et al. (1993)) and illuminated with an ^{55}Fe radioisotope X-ray source (Mn Kα = 5.9 keV; Mn Kβ = 6.49 keV; activity = 171 MBq; active area = 28.27 mm^2) (see **Section 2.11**). The ^{55}Fe radioisotope X-ray source was placed on a PTFE custom holder 5 mm above the detectors. To reduce the count rate seen with the 409 µm diameter photodiode so that it was approximately equal to that seen with the 217 µm diameter photodiode, a 0.23 mm thick polytetrafluoroethylene (PTFE) attenuator was inserted into the 5 mm gap for those measurements. In order to ensure thermal equilibrium at each temperature, the systems were allowed to stabilise for 30 min at each temperature prior to commencing accumulation of the spectra. Different shaping times (0.5 µs, 1 µs, 2 µs, 3 µs, 6 µs, and 10 µs) and reverse biases (0 V, 20 V, 40 V, 60 V, and 100 V) were used across the temperature range (100 °C to 0 °C), to investigate the performances of the systems. Each spectrum had a live time limit of 240 s.

The obtained spectra were energy calibrated using the position of the zero energy noise peak and the centroid channel number of the fitted Mn Kα at 5.9 keV for each spectrum, as points of known energies on MCA's charge scale. The energy resolution (as quantified by the *FWHM* at 5.9 keV) of the system as a function of applied reverse bias, at the highest (100 °C) and lowest (0 °C) investigated temperatures is shown in **Figure 5.15**. The ^{55}Fe X-ray photopeak of the spectrum accumulated using D4 (the 409 µm diameter photodiode) could not be resolved from the zero noise peak, at 100 °C, due to the relatively large capacitance of the photodiode, when no reverse bias was applied (15 pF at 0 V at 100 °C). The *FWHM* at 5.9 keV of both spectrometers were found to be decreased with increasing reverse bias. This may be explained due to the reduced capacitance of the photodiodes (see **Figure 5.12**) and the improved charge collection, with increasing reverse bias. At the highest investigated reverse bias (100 V) and the highest investigated temperature (100 °C), the best energy resolutions achieved with D2 (217 µm diameter photodiode) (active area of 0.04 mm^2) and D4 (409 µm diameter photodiode) (active area of 0.13 mm^2) were found to be 1.31 keV ± 0.04 keV and 1.64 keV ± 0.08 keV, respectively.

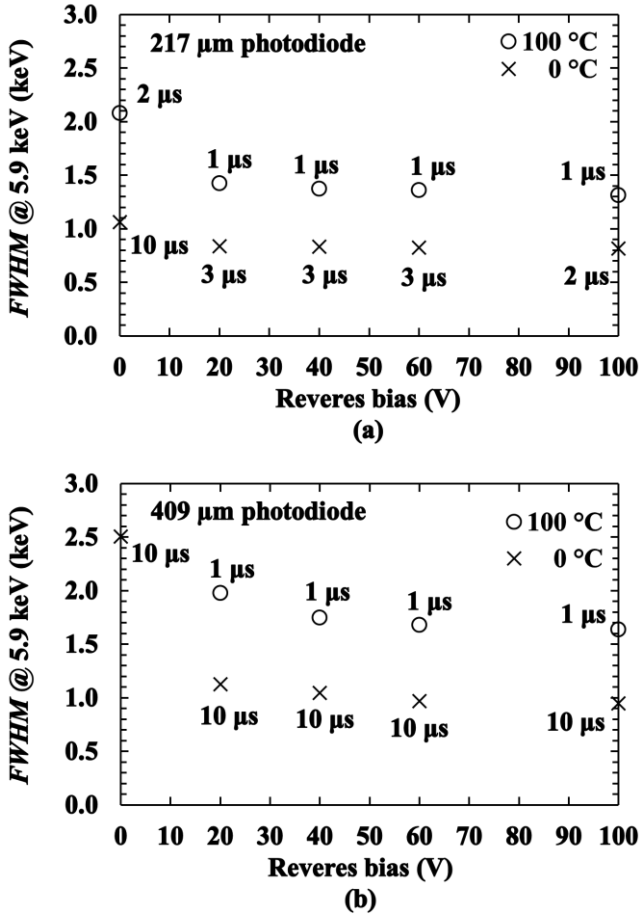

Figure 5.15. Measured best energy resolution (*FWHM* at 5.9 keV) achieved using (a) D2 (217 µm diameter photodiode) and (b) D4 (409 µm diameter photodiode) as functions of applied reverse bias at each investigated temperature and at the optimum shaping time, 100 °C (open circles), and 0 °C (× symbols).

The spectra obtained with the spectrometers at 100 °C and 0 °C, with the detectors reverse biased at the 100 V are shown in **Figure 5.16**. The number of counts is not comparable between the different diameter photodiodes on an area normalised basis because of the presence of the 0.23 mm thick PTFE absorber in the case of the 409 µm diameter photodiode. The energy resolutions (*FWHM* at 5.9 keV) achieved with these $Al_{0.52}In_{0.48}P$ detector X-ray spectrometers were not as good as those achieved using high-quality 4H-SiC detectors (70 µm thick epitaxial layer; area of 0.04 mm^2) and ultra-low-noise preamplifier electronics (233 eV *FWHM* at 5.9 keV at 100 °C) (Bertuccio et al., 2011). However, they are better than has been previously reported at 100 °C with other $Al_{0.52}In_{0.48}P$ detectors (comparing the 217 µm diameter detector with a previously reported 2 µm thick 200 µm diameter $Al_{0.52}In_{0.48}P$ device) (1.31 keV cf. 1.57 keV *FWHM* at 5.9 keV) (Butera et al., 2016a), and comparable to the results obtained with $In_{0.5}Ga_{0.5}P$ photodiodes at 100 °C (5 µm thick i layer; 200 µm diameter; 1.27 keV *FWHM* at 5.9 keV)

(Butera et al., 2018a). They also have better energy resolution than the best reported $Al_{0.8}Ga_{0.2}As$ photodiodes (1 µm thick i layer; 200 µm diameter; 2.2 keV *FWHM* at 5.9 keV) at 90 °C (Barnett et al., 2010).

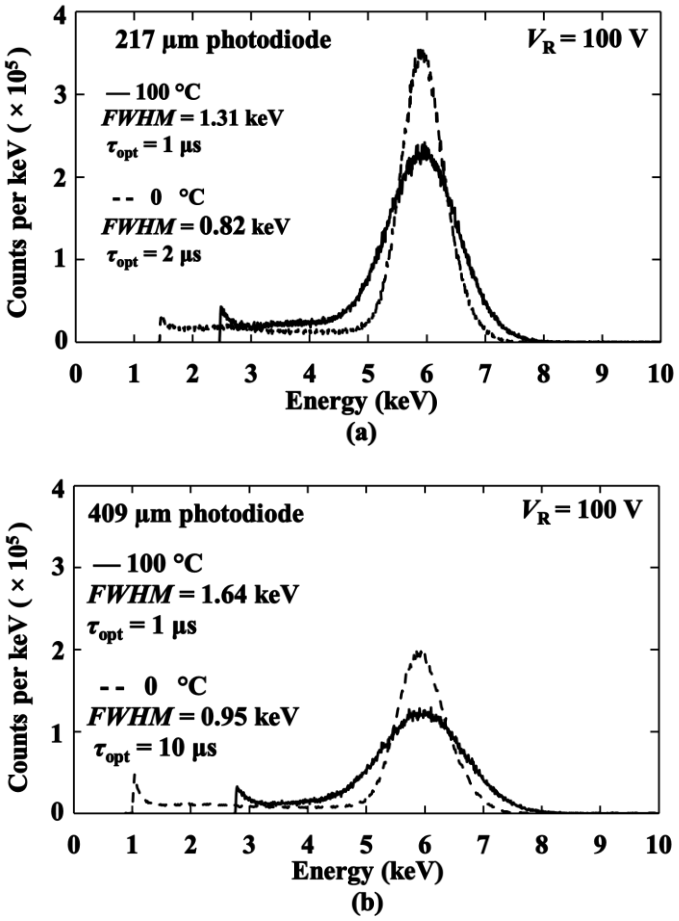

Figure 5.16. ^{55}Fe X-ray spectrum obtained with (a) 217 µm diameter photodiode, D2, and (b) 409 µm diameter photodiode, D4, based X-ray spectrometers at 100 V reverse bias, at a temperature of 100 °C (solid line) and 0 °C (dashed line), at the optimum shaping time.

5.5.2 Noise analysis

The measured *FWHM* at 5.9 keV of the $Al_{0.52}In_{0.48}P$ X-ray spectrometers as functions of shaping time at each investigated temperature at 100 V reverse bias, are shown in **Figure 5.17**. In this figure, an improvement can be seen in *FWHM* at 5.9 keV for both X-ray spectrometers at each investigated shaping time when the temperature decreased from 100 °C to 40 °C. The improvement in *FWHM* for both X-ray spectrometers was comparatively slight when the temperature decreased from 40 °C to 0 °C.

In order to achieve the best energy resolution at each investigated temperature, it was necessary to select different shaping times at different temperatures. For the spectrometer with D2 (217 μm diameter detector), the best available shaping times were 2 μs for temperatures of 0 °C to 40 °C, and 1 μs for 60 °C to 100 °C. For the spectrometer with D4 (409 μm diameter detector), the best available shaping times were 10 μs for temperatures of 0 °C and 20 °C, 3 μs for 40 °C, 2 μs for 60 °C, and 1 μs for 80 °C and 100 °C.

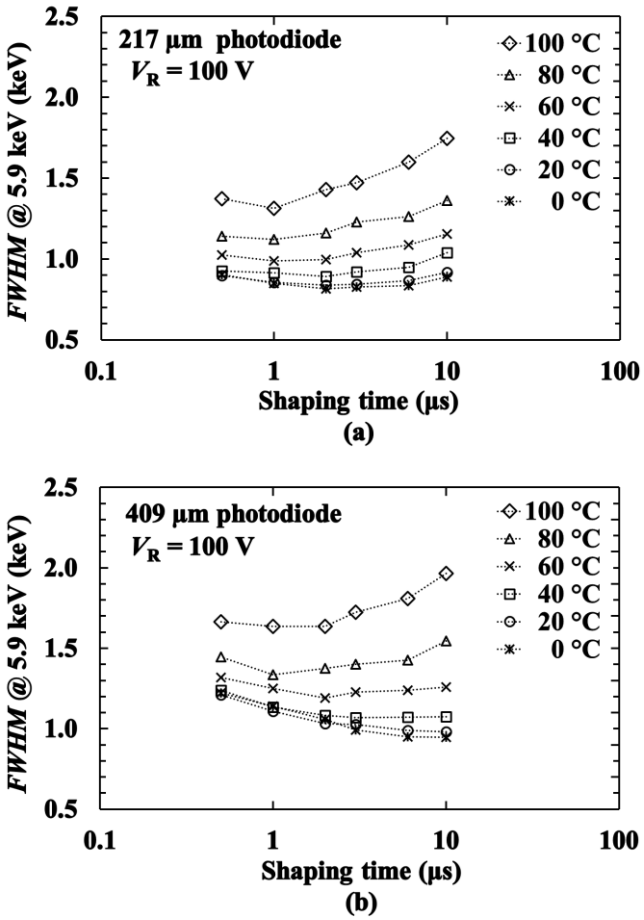

Figure 5.17. Measured *FWHM* at 5.9 keV as functions of shaping time for the $Al_{0.52}In_{0.48}P$ photodiodes based spectrometers (a) 217 μm diameter photodiode, D2, (b) 409 μm diameter photodiode, D4, based spectrometers across the temperature range of 100 °C to 0 °C. The dotted lines are guides for the eyes only.

At each investigated temperature, the total leakage current and the total capacitance at the input of the preamplifier can be estimated by applying a multidimensional unconstrained nonlinear minimisation to the measured *FWHM* at 5.9 keV as a function of shaping time for both X-ray spectrometer at 100 V reverse bias (see **Figure 5.17**), the details are described in Bertuccio & Pullia (1993). The series white noise (including induced gate current), parallel white

noise, and 1/*f* series noise were calculated as described in Lioliou & Barnett (2015) using the estimated total leakage current and the total capacitance at the input of the preamplifier at each temperature. The calculated noise contributions of the series white noise (including induced gate current), parallel white noise, 1/*f* series noise, along with the estimated Fano noise as functions of shaping time for both X-ray spectrometers, at 100 V reverse bias, at the highest investigated temperature (100 °C) and the lowest investigated temperature (0 °C), are shown in **Figures 5.18** and **5.19**.

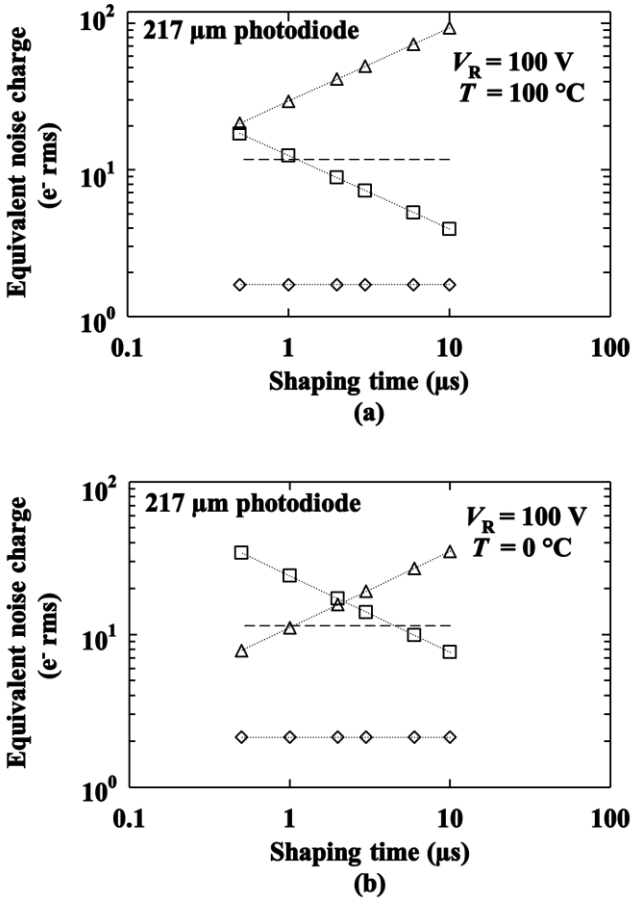

Figure 5.18. Equivalent noise charge as a function of shaping time for the 217 µm diameter $Al_{0.52}In_{0.48}P$ photodiode (D2) connected to the custom low-noise charge-sensitive preamplifier at 100 V reverse bias, at (a)100 °C and (b) 0 °C. Series white noise including induced gate current noise (open squares), parallel white noise (open triangles), Fano noise (dash line), and 1/*f* series noise (open diamonds). The dotted lines are guides for the eyes only.

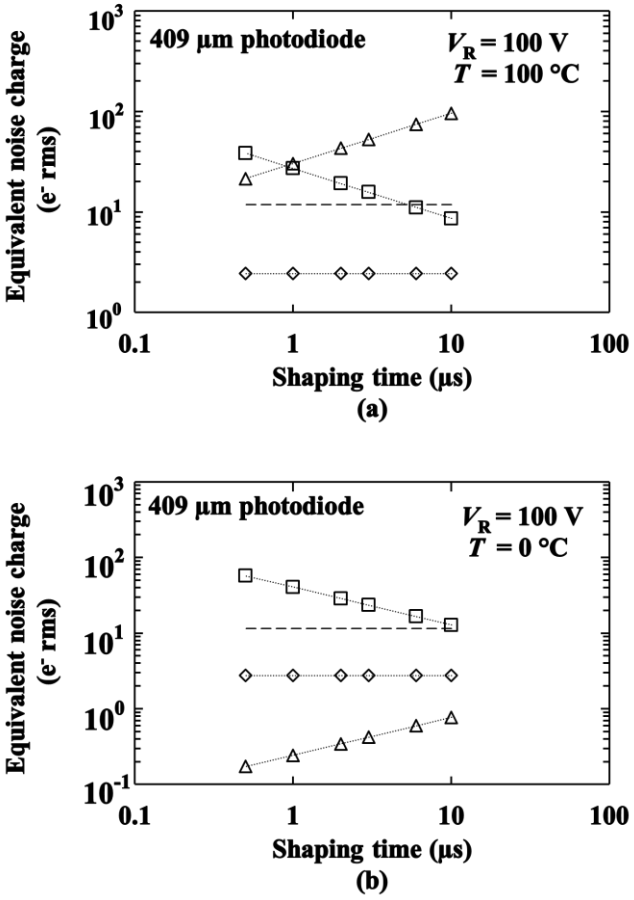

Figure 5.19. Equivalent noise charge as a function of shaping time for the 409 μm diameter $Al_{0.52}In_{0.48}P$ photodiode (D4) connected to the custom low-noise charge-sensitive preamplifier at 100 V reverse bias, (a)100 °C and (b) 0 °C. Series white noise including induced gate current noise (open squares), parallel white noise (open triangles), Fano noise (dash line), and 1/*f* series noise (open diamonds). The dotted lines are guides for the eyes only.

At the highest investigated bias (100 V), at the available optimum shaping time at each temperature, the energy resolutions of both photodiodes spectrometers were found to be improved with decreasing temperature (see **Figure 5.17**), e.g. *FWHM* at 5.9 keV of 1.31 keV at 100 °C cf. 0.82 keV at 0 °C for the 217 μm diameter photodiode spectrometer; *FWHM* at 5.9 keV of 1.64 keV at 100 °C cf. 0.95 keV at 0 °C for the 409 μm diameter photodiode spectrometer. Comparing 100 °C with 0 °C, the parallel white noise was significantly reduced, as shown in **Figures 5.18** and **5.19**. Therefore, much of the improvement in energy resolution at low temperatures stemmed from the reduced parallel white noise (e.g. 93 e^- rms at 100 °C cf. 35 e^- rms at 0 °C for 217 μm diameter photodiode spectrometer at a shaping time of 10 μs; compared with 96 e^- rms at 100 °C and 1 e^- rms at 0 °C for 409 μm diameter photodiode spectrometer at the same shaping time). The majority of the parallel white noise at high temperature came from the leakage

current of the preamplifier input JFET (88 e^- rms, at 100 °C) rather than the detectors. This emphasises the importance of developing new high temperature tolerant preamplifier electronics based on wide bandgap semiconductors Lioliou & Barnett (2015).

The energy resolution of a photodiode X-ray spectrometer may also be affected by incomplete charge collection noise. However, according to results reported in **Section 5.3.2**, the incomplete charge collection noise of these particular photodiodes was negligible at high reverse biases ($\geq$ 80 V). Therefore, at such detector reverse biases, the dielectric noise of the spectrometer can be calculated by subtracting in quadrature the calculated series white noise (including induced gate current noise), parallel white noise, 1/*f* series noise, and the predicted Fano noise, from the measured *FWHM* at 5.9 keV. This calculation was performed and the results are presented in **Figure 5.20**.

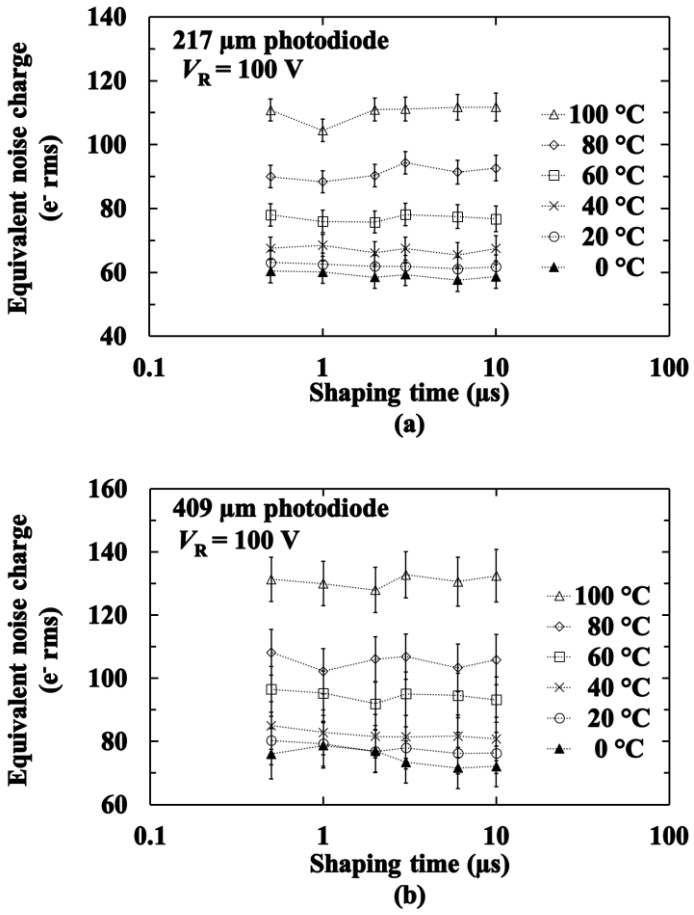

Figure 5.20. Equivalent noise charge of dielectric noise as a function of shaping time for $Al_{0.52}In_{0.48}P$ photodiodes based X-ray spectrometers, (a) D2, 217 µm and (b) D4, 409 µm diameter photodiodes, at 100 V reverse bias, at different temperatures (100 °C, open triangles); (80 °C, open diamonds); (60 °C, open squares); (40 °C, × symbols); (20 °C, open circles); (0 °C, dark triangles). The dotted lines are guides for the eyes only.

The dielectric noise's equivalent noise charge is given by **Equation 2.19**. Each lossy dielectric in close proximity to the input of the preamplifier has its own dielectric noise which is dependent on its own dielectric dissipation factor and capacitance, but it is common to combine all the dielectric noise sources and state an apparent overall dielectric dissipation factor and capacitance. Nevertheless, assuming that the overall dielectric noises for the two spectrometers were identical except for the different contributions from the photodiodes themselves (i.e. arising from their different capacitances) the dielectric dissipation factor of $Al_{0.52}In_{0.48}P$ itself can be estimated using **Equation 2.19** and the procedure as described in **Section 5.3.2**. As such, the dielectric dissipation factor of $Al_{0.52}In_{0.48}P$ was estimated at different temperatures for the first time, and is presented in **Figure 5.21**. The uncertainties (error bars) in the dielectric dissipation factor shown in

Figure 5.21 reflect the uncertainties in the capacitances of the detectors and the uncertainties in the dielectric noise which were propagated from the uncertainties in the energy resolution.

At 100 °C, the dielectric dissipation factor of the $Al_{0.52}In_{0.48}P$ was estimated to be $5.4 \times 10^{-3} \pm 0.8 \times 10^{-3}$. At 0 °C was $2.4 \times 10^{-3} \pm 0.5 \times 10^{-3}$. The dielectric dissipation factor at 20 °C ($2.5 \times 10^{-3} \pm 0.5 \times 10^{-3}$) was found to be similar to the previously reported measurement of the $Al_{0.52}In_{0.48}P$ dielectric dissipation factor of at room temperature ($2.2 \times 10^{-3} \pm 1.1 \times 10^{-3}$) (see **Section 5.3.2**).

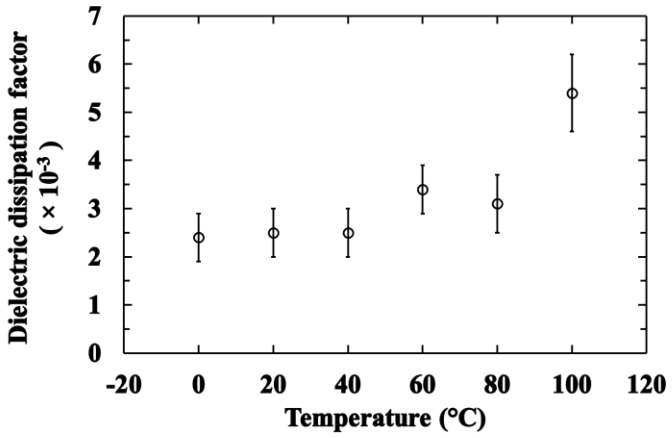

Figure 5.21. The estimated dielectric dissipation factor of $Al_{0.52}In_{0.48}P$ over the temperature range of 0 °C to 100 °C.

5.6 Conclusions and discussion

The results of the electrical characterisation of four custom-made $Al_{0.52}In_{0.48}P$ mesa p^+-i-n^+ X-ray photodiodes (D1 – D4) with 6 μm thick i layers and two different diameters (217 μm ± 15 μm for D1 and D2; 409 μm ± 28 μm for D3 and D4) have been reported. The detectors are the thickest $Al_{0.52}In_{0.48}P$ photodiodes so far reported for X-ray spectroscopy.

The photodiodes were initially operated at room temperature (24 °C). Measurements of capacitance as functions of applied reverse bias showed similar capacitances between photodiodes of the same diameter. The capacitances of the four photodiodes were found decreased with the increased applied reverse bias. At the highest investigated bias (100 V), the capacitances of the 217 μm diameter photodiodes (D1 and D2) and the 409 μm diameter photodiodes (D3 and D4) were found to be 0.7 pF and 2.5 pF, respectively. The measured leakage currents of both diameters' photodiodes were found to be < 3 pA (corresponding to leakage

current densities < 2 nA/cm^2) at 100 V reverse bias (corresponding to electric field strengths of 167 kV/cm). The performance of these photodiodes as photon counting spectroscopic X-ray detectors was investigated by connecting the photodiodes to a custom-made low-noise charge-sensitive preamplifier and illuminating them with an ^{55}Fe radioisotope X-ray source. The best energy resolutions (*FWHM* at 5.9 keV) obtained with the 217 μm diameter device (D2) and 409 μm diameter device (D4) were 0.89 keV and 1.05 keV, respectively. To achieve this both detectors were reverse biased at 100 V. The detectors and readout electronics were operated at room temperature. The noise contribution from the incomplete charge collection noise was found insignificant when the detectors were reverse biased $\geqslant$ 80 V. At the highest investigated reverse bias (100 V), the limiting noise source affecting in the energy resolution of both spectrometers was mainly due to the dielectric noise. Assuming the difference in the dielectric noise between the two spectrometers was solely due to the different capacitances of the photodiodes, the dielectric dissipation factor of $Al_{0.52}In_{0.48}P$ was estimated for the first time; a value of $2.2 \times 10^{-3} \pm 1.1 \times 10^{-3}$ was found.

Following the room temperature measurements, the electrical characteristics and photon counting spectroscopic X-ray detection performance of two of the detectors (D2, 217 μm ± 15 μm diameter; D4, 409 μm ± 28 μm diameter) were studied as functions of temperature, T (0 °C $\leqslant T \leqslant$ 100 °C). Thus, these detectors became the thickest $Al_{0.52}In_{0.48}P$ X-ray photodiodes to be characterised for their high temperature (> 24 °C) performance so far.

Measurements of the detectors' capacitances as functions of applied reverse bias and temperature showed that the capacitances of both photodiodes were broadly consistent across the investigated temperature range when the detectors were reverse biased at > 5 V. Measurements of the detectors' leakage current as functions of applied reverse bias and temperature showed that the devices had low leakage currents (< 5 pA) even at the maximum investigated reverse bias (100 V) and temperature (100 °C).

With the detectors connected to a custom-made low-noise charge-sensitive preamplifier, ^{55}Fe radioisotope X-ray source spectra were accumulated across the temperature range. At the highest investigated temperature (100 °C) and greatest reverse bias (100 V), the best energy resolutions (*FWHM* at 5.9 keV) achieved with the 217 μm diameter detector (D2) and 409 μm diameter detector (D4) were 1.31 keV and 1.64 keV, respectively. At the lowest investigated temperature (0 °C), the energy resolution of 217 μm diameter detector (D2) and 409 μm diameter detector (D4) had improved to 0.82 keV and 0.95 keV, respectively. The different noise contributors to the energy resolutions (*FWHM* at 5.9 keV) were computed as functions of shaping time and temperature. The improvement in energy resolution as the temperature was reduced was largely

due to decreased leakage current of the spectrometers with reduced temperatures; the leakage current of the Si JFET is a significant contributor at high temperatures. For the first time, the temperature dependence of dielectric dissipation factor of $Al_{0.52}In_{0.48}P$ was estimated, a value of $5.4 \times 10^{-3} \pm 0.8 \times 10^{-3}$ was found at 100 °C.

The work presented here shows the current state of art for custom compound semiconductor X-ray detectors specifically designed for soft X-ray spectroscopy in high temperature environments. Compared with other 200 µm diameter $Al_{0.52}In_{0.48}P$ X-ray photodiodes (2 µm thick i layer) that were reported previously (Butera et al., 2016a) (Butera et al., 2016b), the 217 µm diameter $Al_{0.52}In_{0.48}P$ X-ray photodiodes reported in this thesis have a thicker i layer which results in a higher quantum efficiency at a given energy (e.g. 0.56 for the 6 µm thick devices cf. 0.26 for the 2 µm thick devices, at 5.9 keV). The 217 µm diameter $Al_{0.52}In_{0.48}P$ X-ray photodiode reported here had a comparable leakage current (e.g. at 100 °C, 2.1 pA for the 6 µm thick device cf. ~1 pA for the 2 µm thick device) and a lower capacitance (e.g. at 100 °C, 0.7 pF for the 6 µm thick device cf. 1.4 pF for the 2 µm thick device), which results in a slightly improvement in energy resolution (*FWHM* at 5.9 keV) when both devices coupled to a similar preamplifier electronics (e.g. 1.31 keV for the 6 µm i layer $Al_{0.52}In_{0.48}P$ device cf. 1.57 keV for 2 µm i layer $Al_{0.52}In_{0.48}P$ device, at 100 °C) (Butera et al., 2016b).

Even though the commercial 4H-SiC photodiodes (**Chapters 3** and **4**) were able to be operated as photon counting spectroscopy detectors of soft X-ray at high temperature (> room temperature) without cooling, the limitations of these devices (e.g. relatively low quantum efficiency and relatively poor energy resolution), limits their utility for some space science applications. Thus motivating the development of custom detectors.

Compared with the commercial 4H-SiC photodiodes (epitaxial layer thickness = ~5.15 µm) reported in **Chapters 3** and **4**, the $Al_{0.52}In_{0.48}P$ X-ray photodiodes (i layer thickness = 6 µm) reported here have a much higher quantum efficiency (e.g. 0.56 for the $Al_{0.52}In_{0.48}P$ devices cf. 0.16 for the 4H-SiC devices, at 5.9 keV) mainly as a result of the larger linear absorption coefficient of $Al_{0.52}In_{0.48}P$ (1302 cm^{-1} at 5.9 keV) cf. 4H-SiC (346 cm^{-1} at 5.9 keV).

Whilst the custom-made $Al_{0.52}In_{0.48}P$ devices reported here had a smaller area (0.13 mm^2 for the largest device) than the commercial 4H-SiC devices (0.5 mm^2 for the largest device), larger custom $Al_{0.52}In_{0.48}P$ detectors could be fabricated. However, for the currently reported photodiodes, it should be noted that for 5.9 keV X-ray photons, despite the better quantum efficiency of the $Al_{0.52}In_{0.48}P$ detectors (0.56) cf. the 4H-SiC detectors (0.16), assuming a uniform illumination, more photons would be detected per second with the 0.5 mm^2 4H-SiC detector than

the 0.13 mm^2 $Al_{0.52}In_{0.48}P$ detector (the product of the area and quantum efficiency is greater for the 4H-SiC device (0.08) than the $Al_{0.52}In_{0.48}P$ device (0.07)).

$Al_{0.52}In_{0.48}P$ has a better expected Fano-limited energy resolution than 4H-SiC due to the smaller electron-hole pair creation energy of $Al_{0.52}In_{0.48}P$ ($FWHM_{Fano}$ = 145 eV for $Al_{0.52}In_{0.48}P$ assuming F = 0.12, cf. $FWHM_{Fano}$ = 160 eV for 4H-SiC, at 5.9 keV, both at room temperature) (see **Table 1.1**) (see **Equation 2.12**). The incomplete charge collection noise of the custom-made $Al_{0.52}In_{0.48}P$ devices was negligible at high reverse biases (≥ 80 V) at 5.9 keV, thus indicating that if the detectors were connected to ultra-low noise readout electronics with negligible noise, the Fano noise would dominate in $Al_{0.52}In_{0.48}P$, and thus the practically achievable energy resolution would be better with $Al_{0.52}In_{0.48}P$ than 4H-SiC.

In the currently reported measurements, the custom-made $Al_{0.52}In_{0.48}P$ photodiode (area of 0.04 mm^2) had a better energy resolution (*FWHM* at 5.9 keV) than the commercial 4H-SiC photodiode (area of 0.06 mm^2) when both devices coupled to a similar preamplifier electronics (e.g. *FWHM* at 5.9 keV = 1.3 keV for the $Al_{0.52}In_{0.48}P$ detector cf. 2.6 keV for the commercial 4H-SiC detector, at 100 °C). In both cases a significant contribution to the noise at high temperatures came from the Si input JFET of the charge sensitive preamplifier. Use of a SiC input JFET (Lioliou & Barnett, 2015) would substantially improve the achievable high-temperature energy resolutions. With such an improvement made, the instrumentation would be highly attractive for use in missions to the surfaces of the planets and comets close to the Sun (e.g. temperatures of 70 °C at the polar region of Mercury (Novara, 2001); ~87 °C at the surface of comet Halley at 0.8 AU (Emerich et al., 1988)), where it could be used for X-ray fluorescence spectroscopy of the surface materials.

Chapter 6 Conclusions, Discussion, and Future Work

6.1 Conclusions and discussion

Commercial-off-the-shelf (COTS) 4H-SiC and custom-made $Al_{0.52}In_{0.48}P$ photodiodes have been studied for their suitability as radiation detectors at high temperature.

Commercial 4H-SiC UV p-n photodiodes with two different active areas (0.06 mm^2 and 0.5 mm^2) have been demonstrated to function as X-ray photon counting spectroscopy detectors, with a modest energy resolution (*FWHM* at 5.9 keV) (1.8 keV for 0.06 mm^2 photodiodes; 3.3 keV for 0.5 mm^2 photodiodes) at room temperature (24 °C). The dielectric noise and series white noise were found to be the dominant noise sources in the system (see **Figure 3.8**). One of the 0.06 mm^2 detectors was selected to be further investigated across the temperature range 100 °C to 0 °C. At the highest investigate temperature (100 °C), the measured energy resolution (*FWHM* at 5.9 keV) was found to be 2.6 keV. The dielectric noise and possibly incomplete charge collection noise (from charge created in the substrate) were found be to the dominant noise contributors to the system across the investigated range of temperatures (see **Figure 3.19**). The X-ray characterisation of the selected 0.06 mm^2 detector was then extended with study of its response to higher energy (< 25 keV) X-rays, the energy resolutions (*FWHM*) achieved with the detector were 1.6 keV – 1.8 keV across the investigated energy range. The energy-charge linearity and the count rate linearity were investigated and found to be linear (see **Figures 4.5** and **4.6**).

The 0.06 mm^2 4H-SiC detector was then further investigated as an electron (β^- particle) detector experimentally using a ^{63}Ni radioisotope β^- particle source at temperatures from 20 °C to 100 °C, and theoretically via Monte Carlo simulations produced using the CASINO computer program. Comparison between the experimentally detected and simulated ^{63}Ni β^- particle spectra showed that the commercial 4H-SiC photodiode based spectrometer produced agreement, and resolved the outstanding question as to the thickness of the active region in the detectors, which arose in the measurements made with X-rays. The detectors were thus demonstrated to be capable of electron (β^- particle) spectroscopy.

Following extensive investigation of the COTS 4H-SiC detectors, custom-made $Al_{0.52}In_{0.48}P$ mesa p^+-i-n^+ X-ray photodiodes with 6 µm thick i layers and two different diameters (217 µm ± 15 µm and 409 µm ± 28 µm) were investigated as soft X-ray photon counting spectroscopy detectors at different temperatures, 0 °C $\leqslant T \leqslant$ 100 °C. $Al_{0.52}In_{0.48}P$ is a new material for this application

and such detectors are at the very cutting edge of modern X-ray detector research. At room temperature (24 °C), the best energy resolutions (*FWHM* at 5.9 keV) achieved with the 217 µm diameter photodiodes (D1 and D2) and the 409 µm diameter photodiodes (D3 and D4) were 0.9 keV and 1.1 keV, respectively. At the highest investigated temperature (100 °C), the best energy resolutions (*FWHM* at 5.9 keV) of one of the 217 µm diameter photodiodes (D2) and one of the 409 µm diameter photodiodes (D4) were respectively found to be 1.31 keV and 1.64 keV. Dielectric noise was found to be the dominant noise type in the system (see **Figure 5.9**). The measurements with $Al_{0.52}In_{0.48}P$ also enabled estimation of the material's dielectric dissipation factor for the first time; $2.2 \times 10^{-3} \pm 1.1 \times 10^{-3}$ at room temperature (24 °C), $5.4 \times 10^{-3} \pm 0.8 \times 10^{-3}$ at 100 °C.

The work presented in this thesis contains electrical characterisation of detectors made from two different materials (4H-SiC and $Al_{0.52}In_{0.48}P$) at different operating conditions (bias, temperature). All devices were studied under the illumination of an ^{55}Fe radioisotope X-ray source. Moreover, one of the commercial 4H-SiC photodiodes was further studied under the illumination of higher X-ray energies as well as ^{63}Ni radioisotope β^- particle source. The work was supported with calculations, simulations, and comparisons of the results with previously published works. The work conducted with the commercial 4H-SiC UV p-n photodiodes and custom-made $Al_{0.52}In_{0.48}P$ p^+-i-n^+ mesa photodiodes show the current state of the art for both commercial photodiodes and the custom-made compound semiconductor X-ray detectors for use at high temperatures. In both cases, the devices have been demonstrated to function as soft X-ray detectors at high temperatures. In addition, the commercial 4H-SiC photodiodes have been shown to operate as soft electron detectors for electron counting spectroscopy at high temperatures. The systematic study advances knowledge of compound semiconductor radiation spectrometers and improves understanding of these devices with a view to using them in future space missions.

For both types of detector, the X-ray energy resolutions (*FWHM* at 5.9 keV) reported with the detectors coupled to the present preamplifier electronics are currently not as good as with some other custom X-ray detectors, e.g. Si drift detectors (148 eV at 30 °C) (Bertuccio et al., 2015); $In_{0.5}Ga_{0.5}P$ p^+-i-n^+ mesa photodiodes (0.77 keV at 20 °C; 1.27 keV at 100 °C) (Butera et al., 2018a); custom 4H-SiC Schottky X-ray detectors (196 eV at 30 °C; 233 eV at 100 °C) (Bertuccio et al., 2011).

The $In_{0.5}Ga_{0.5}P$ devices derive their comparatively better energy resolution mainly as a consequence of that material's lower electron-hole pair creation energy (4.94 eV (Butera et al., 2018a) at 20 °C) cf. 4H-SiC and $Al_{0.52}In_{0.48}P$; those detectors were coupled to a preamplifier comparable to that used for the measurements reported in this thesis. The Si drift detector and

custom 4H-SiC Schottky X-ray detectors were coupled to ultra-low-noise readout electronics and the excellent energy resolutions reported reflect this. One significant technique used to reduce dielectric noise in such electronics is to directly wire-bond the detector to the gate of the input transistor. Whist this could be used for the custom $Al_{0.52}In_{0.48}P$ (and $In_{0.5}Ga_{0.5}P$) detectors since control over their packaging is possible, the COTS 4H-SiC detectors cannot benefit from this as they are supplied already packaged.

A further feature of the $Al_{0.52}In_{0.48}P$ devices which could be improved, but that cannot be changed for the COTS 4H-SiC devices, is their quantum efficiency. This could be improved by growing thicker absorption layers. The same is true for the detector areas; different area $Al_{0.52}In_{0.48}P$ devices could be fabricated, but areas of the COTS devices are fixed by the manufacturer. This exposes the inherent dichotomy between COTS and custom devices; custom devices can be tailored to improve performance or meet specific requirements, whereas COTS devices cannot.

Different space missions have different requirements for their associated space instruments; for example, the priority can be placed on low cost (suggesting COTS devices) or high performance (suggesting custom devices), hence a trade-off must be made in the design of instrumentation appropriate for the application.

Even with the limitations inherent to the commercial 4H-SiC detector, its benefits of low cost, commercial availability, ability to operate at uncooled at high temperature, visible blindness, and likely radiation hardness, make it an interesting and potentially useful detector for numerous cost-sensitive space applications. They could be used as X-ray detectors on CubeSats for heliophysics research, e.g. understanding the influences of solar soft X-rays on the ionosphere of Earth (Avakyan, 2008) (Richards, 2013) (Hayes et al., 2017). They could also be used to monitor the soft electron distribution in the near-Earth environment, or elsewhere in the solar system, for space plasma phenomenon research, e.g. understanding the mechanisms of sudden changes of electron fluxes in the outer radiation belt (Boynton et al., 2016). For missions with greater budgets, the use of custom made detectors is still expected.

$Al_{0.52}In_{0.48}P$ is one of the most interesting materials for X-ray detectors to have emerged in recent times. The work reported in this thesis follows on from the earlier proof of principle research that was conducted with thin (2 μm) layers. The performance demands placed on custom devices is typically greater than for COTS devices, in order to justify the increased financial costs associated with development. With refinements to the photodiode packaging and preamplifier electronics to improve the spectral resolution, along with the improvements in detection quantum efficiencies of the detectors brought by growing thicker absorption layer devices, the

custom-made $Al_{0.52}In_{0.48}P$ based spectrometers reported here are likely to find use in many future space applications, e.g. in situ/remote planetary X-ray fluorescence spectrometry in high temperature environments such as at Mercury and at comets close to the Sun. Moreover, since there can be control over the fabrication process, the opportunity exists to fabricate monolithic pixel arrays with $Al_{0.52}In_{0.48}P$, thus opening the possibility of imaging X-ray spectrometers.

6.2 Future work

Considering the results and the discussions reported in the thesis, there are many possibilities for future research both directly concerning the devices investigated, and in their application in space research. Here discussion is limited solely to the instrumentation rather than its applications.

With respect to work on the devices themselves, one critical aspect to investigate is their radiation hardness. Radiation doses in space environments can be substantial (e.g. 20 krad/day at the surface of Europa (Kolawa et al., 2007)), and the progressive changes in detector performance which occur as the cumulative dose increases must be understood in order to be able to understand changes in the detectors' performance over mission lifetimes. The effects of detector temperature and operating condition on radiation damaged experienced should be investigated as part of this.

Characterisation of the detectors at higher energies is also interesting and should be conducted. Investigation of the performance of the detectors as spectrometers for higher energy X-rays and γ-rays (e.g. from ^{241}Am and ^{109}Cd radioisotope X/γ-ray sources) would enable further study of energy dependent phenomena such as charge trapping and incomplete charge collection noise. It would also open up the possibility of using the detectors in nuclear research by virtue of demonstrating their potential for the detection of these high energy photons (e.g. 59.5 keV from ^{241}Am; 88 keV from ^{109}Cd).

For the 4H-SiC detectors, dark/illuminated current measurements made using a chopper wheel and lock-in amplifier would be beneficial to eliminate any effects from varying leakage currents (see **Sections 3.3.1**, **3.5.1**, and **4.4.2**). This may further clarify the origin of the apparently greater than expected illuminated currents observed with the detectors, if in fact the origin of such currents is a consequence of increased leakage rather than greater than expected photocurrents.

Future work on $Al_{0.52}In_{0.48}P$ photodiodes/spectrometers may include growing structures with thicker i layers to improve the quantum efficiency at high energies, and fabricating larger area devices. Systematic device fabrication studies should be carried out to optimise these processes;

the importance of this is evidenced by the change in etchant which was required for the 6 µm thick devices reported here in order to achieve an adequate vertical etch rate (see **Section 1.9.2**).

Even for the existing $Al_{0.52}In_{0.48}P$ structures, it would be of immediate benefit to redesign the front-end of the preamplifier and its interface with the detector (e.g. using a bare die JFET directly wire-bonded to the detector) (Bertuccio et al., 1995). This would reduce the dielectric noise and improve the achievable energy resolution. Development of a suitable preamplifier input JFET made from a wide bandgap material (e.g. SiC) (Lioliou & Barnett, 2015) would also be beneficial, particularly at high temperature, where the performance of the current spectrometers is limited more by the leakage current of the input JFET than the leakage currents of the detectors themselves.

References

Abbey, A.F., Bennie, P.J., Turner, M.J.L., Altieri, B., and Rives, S., 2003, *Cooling Out the Radiation Damage on the XMM-Newton EPIC MOS CCDs*, Nuclear Instruments and Methods in Physics Research A, Vol. 513, pp. 136-142.

Abdollahi, A., Golzan, M.M., and Aghayar, K., 2016, *First-principles Investigation of Electronic Properties of $Al_xIn_{1-x}P$ Semiconductor Alloy*, Journal of Materials Science, Vol. 51, pp. 7343-7354.

Abubakar, Y.M., Lohstroh, A., and Sellin, P.J., 2015, *Stability of Silicon Carbide Particle Detector Performance at Elevated Temperatures*, IEEE Transactions on Nuclear Science, Vol. 62, pp. 2360-2366.

Adachi, S., 2005, *Properties of Group-IV, III-V and II-VI Semiconductors*, John Wiley & Sons, England.

Alam, T.R., and Pierson, M.A., 2016, *Principles of Betavoltaic Battery Design*, Journal of Energy and Power Sources, Vol. 3, pp. 11-41.

Alig, R.C., and Bloom, S., 1975, *Electron-hole-pair Creation Energies in Semiconductors*, Physical Review Letters, Vol. 35, pp. 1522-1525.**American National standards Institute**, 1976, *An American National Standard IEEE Standard Test Procedures for Amplifiers and Preamplifiers for Semiconductor Radiation Detectors for Ionizing Radiation*, IEEE Std 301-1976.

Anon, N.D.a, *Broadband SiC based UV photodiode A = 0.06 mm^2, SG01S-18*, Rev.6.0, SGlux SolGel Technologies GmbH, Berlin, Germany.

Anon, N.D.b, *Broadband SiC based UV photodiode A = 0.50 mm^2, SG01D-18*, Rev.6.0, SGlux SolGel Technologies GmbH, Berlin, Germany.

Auckloo, A., Cheong, J.S., Meng, X., Tan, C.H., Ng, J.S., Krysa, A., Tozer, R.C., and David, J.P.R., 2016, *$Al_{0.52}In_{0.48}P$ Avalanche Photodiodes for Soft X-ray Spectroscopy*, Journal of Instrumentation, Vol. 11, Art. No. P03021.

Avakyan, S.V., 2008, *Physics of the Solar-terrestrial Coupling: Results, Problems, and New Approaches*, Geomagnetism and Aeronomy, Vol. 48, pp. 417-424.

Baganoff, F.K., Bautz, M.W., Brandt, W.N., Chartas, G., Feigelson, E.D., Garmire, G.P., Maeda, Y., Morris, M., Ricker, G.R., Townsley, L.K., and Walter, F., 2001, *Rapid X-ray Flaring from*

the Direction of the Supermassive Black Hole at the Galactic Centre, Nature, Vol. 413, pp. 45-48.

Barcons, X., Nandra, K., Barret, D., Den Herder, J.W., Fabian, A.C., Piro, L., Watson, M.G., 2015, *Athena: The X-ray Observatory to Study the Hot and Energetic Universe*, Journal of Physics: Conference Series, Vol. 610, Art. No. 012008.

Barnett, A.M., Bassford, D.J., Lees, J.E., Ng, J.S., Tan, C.H., and David, J.P.R., 2010, *Temperature Dependence of AlGaAs Soft X-ray Detectors*, Nuclear Instruments and Methods in Physics Research A, Vol. 621, pp. 453-455.

Barnett, A.M., 2011, *Wide Band Gap Compound Semiconductor Detectors for X-ray Spectroscopy in Harsh Environments*, PhD Thesis, Department of Physics and Astronomy, University of Leicester, Leicester, UK.

Barnett, A.M., Lees, J.E., Bassford, D.J., Ng, J.S., Tan, C.H., Babazadeh, N., and Gomes, R.B., 2011, *The Spectral Resolution of High Temperature GaAs Photon Counting Soft X-ray Photodiodes*, Nuclear Instruments and Methods in Physics Research A, Vol. 654, pp. 336-339.

Barnett, A.M., Lees, J.E., Bassford, D.J., and Ng, J.S., 2012, *A Varied Shaping Time Noise Analysis of $Al_{0.8}Ga_{0.2}As$ and GaAs Soft X-ray Photodiodes Coupled to A Low-noise Charge Sensitive Preamplifier*, Nuclear Instruments and Methods in Physics Research A, Vol. 673, pp. 10-15.

Barnett, A.M., Lees, J.E., and Bassford, D.J., 2013a, *First Spectroscopic X-ray and Beta Results from a 400 μm Diameter $Al_{0.8}Ga_{0.2}As$ Photodiode*, Journal of Instrumentation, Vol. 8, Art. No. P10014.

Barnett, A.M., Lees, J.E., and Bassford, D.J., 2013b, *A Multi-energy (2-60 keV) Calibration of 200 μm and 400 μm Diameter Spectroscopic GaAs X-ray Photodiodes*, Journal of Instrumentation, Vol. 8, Art. No. P09014.

Barnett, A.M., 2014, *Characterization of GaAs Mesa Photodiodes with X-ray and γ-ray Photons*, Nuclear Instruments and Methods in Physics Research A, Vol. 756, pp. 39-44.

Barnett, A.M., Lioliou, G., and Ng, J.S., 2015, *Characterization of Room Temperature AlGaAs Soft X-ray Mesa Photodiodes*, Nuclear Instruments and Methods in Physics Research A, Vol. 774, pp. 29-33.

Barthelmy, S.D., Barbier, L.M., Cummings, J.R., Fenimore, E.E., Gehrels, N., Hullinger, D., Krimm, H.A., Markwardt, C.B., Palmer, D.M., Parsons, A., Sato, G., Suzuki, M., Takahashi, T.,

Tashiro, M., and Tueller, J., 2005, *The Burst Alert Telescope (BAT) on the SWIFT MIDEX Mission*, Space Science Reviews, Vol. 120, pp. 143-164.

Benz, A.O., Krucker, S., Hurford, G.J., Arnold, N.G., Orleanski, P., Gröbelbauer, H.P., Klober, S., Iseli, L., Wiehl H.J., Csillaghy, A., Etesi, L., Hochmuth, N., Battaglia, M., Bednarzik, M., Resanovic, R., Grimm, O., Viertel, G., Commichau, V., Meuris, A., Limousin, O., Brun, S., Vilmer, N., Skup, K.R., Graczyk, R., Stolarski, M., Michalska, M., Nowosielski, W., Cichocki, A., Mosdorf, M., Seweryn, K., Przepiórka, A., Sylwester, J., Kowalinski, M., Mrozek, T., Podgorski, P., Mann, G., Aurass, H., Popow, E., Önel, H., Dionies, F., Bauer, S., Rendtel, J., Warmuth, A., Woche, M., Plüschke, D., Bittner, W., Paschke, J., Wolker, D., Van Beek, H.F., Farnik, F., Kasparova, J., Veronig, A.M., Kienreich, I.W., Gallagher, P.T., Bloomfield, D.S., Piana, M., Massone, A.M., Dennis, B.R., Schwarz, R.A., and Lin, R.P., 2012, *The Spectrometer Telescope for Imaging X-rays on Board the Solar Orbiter Mission*, SPIE proceedings, Space Telescopes and Instrumentation: Ultraviolet to Gamma Ray, Vol. 8443, Art. No. 84433L.

Benkhoff, J., van Casteren, J., Hayakawa, H., Fujimoto, M., Laakso, H., Novara, M., Ferri, P., Middleton, H.R., and Ziethe, R., 2010, *BepiColombo-Comprehensive Exploration of Mercury: Mission Overview and Science Goals*, Planetary and Space Science, Vol. 58, pp. 2-20.

Bertuccio, G., and Pullia, A., 1993, *A method for the determination of the noise parameters in preamplifying systems for semiconductor radiation detectors*, Review of Scientific Instruments, Vol. 64, pp. 3294-3298.

Bertuccio, G., Rehak, P., and Xi, D., 1993, *A Novel Charge Sensitive Preamplifier without the Feedback Resistor*, Nuclear Instruments and Methods in Physics Research A, Vol. 326, pp. 71-76.

Bertuccio, G., Fasoli, L., Fiorini, C., and Sampietro, M., 1995, *Spectroscopy Charge Amplifier for Detectors with Integrated Front-end FET*, IEEE Transactions on Nuclear Science, Vol. 42, pp. 1399-1405.

Bertuccio, G., Pullia, A., and De Geronimo, G., 1996, *Criteria of Choice of the Front-end Transistor for Low-noise Preamplification of Detector Signals at Sub-microsecond Shaping Times for X- and γ-ray Spectroscopy*, Nuclear Instruments and Methods in Physics Research A, Vol. 380, pp. 301-307.

Bertuccio, G., Pullia, A., Lauter, J., Forster, A., and Luth, H., 1997, *Pixel X-ray Detectors in Epitaxial Gallium Arsenide with High-energy Resolution Capabilities (Fano Factor Experimental Determination)*, IEEE Transactions on Nuclear Science, Vol. 44, pp. 1-5.

Bertuccio, G., Casiraghi, R., and Nava, F., 2001, *Epitaxial Silicon Carbide for X-ray Detection*, IEEE Transactions on Nuclear Science, Vol. 48, pp. 232-233.

Bertuccio, G., and Casiraghi, R., 2003, *Study of Silicon Carbide for X-ray Detection and Spectroscopy*, IEEE Transactions on Nuclear Science, Vol. 50, pp. 175-185.

Bertuccio, G., Casiraghi, R., Gatti, E., Maiocchi, D., Nava, F., Canali, C., Cetronio, A., and Lanzieri, C., 2003, *SiC X-ray Detectors for Spectroscopy and Imaging over a Wide Temperature Range*, Materials Science Forum, Vol. 433-436, pp. 941-944.

Bertuccio, G., Casiraghi, R., Cetronio, A., Lanzieri, C., and Nava, F., 2004, *Silicon Carbide for High Resolution X-ray Detectors Operating up to 100 °C*, Nuclear Instruments and Methods in Physics Research A, Vol. 522, pp. 413-419.

Bertuccio, G., Caccia, S., Casiraghi, R., and Lanzieri, C., 2006, *Possibility of Subelectron Noise with Room-temperature Silicon Carbide Pixel Detectors*, IEEE Transactions on Nuclear Science, Vol. 53, pp. 2421-2427.

Bertuccio, G., and Caccia, S., 2007, *Progress in Ultra-low-noise ASICs for Radiation Detectors*, Nuclear Instruments and Methods in Physics Research A, Vol. 579, pp. 243-246.

Bertuccio, G., 2010, *Silicon Carbide Radiation Microdetectors for Harsh Environments*, SPIE proceedings, Micro- and Nanotechnology Sensors, Systems, and Applications II, Vol. 7679, Art. No. 76790T.

Bertuccio, G., Caccia, S., Puglisi, D., and Macera, D., 2011, *Advances in Silicon Carbide X-ray Detectors*, Nuclear Instruments and Methods in Physics Research A, Vol. 652, pp. 193-196.

Bertuccio, G., Puglisi, D., Torrisi, L., and Lanzieri, C., 2013a, *Silicon Carbide Detector for Laser-generated Plasma Radiation*, Applied Surface Science, Vol. 272, pp. 128-131.

Bertuccio, G., Puglisi, D., Pullia, A., and Lanzieri, C., 2013b, *X-γ Ray Spectroscopy with Semi-Insulating 4H-Silicon Carbide*, IEEE Transactions on Nuclear Science, Vol. 60, pp. 1436-1441.

Bertuccio, G., Ahangarianabhari, M., Graziani, C., Macera, D., Shi, Y., Rachevski, A., Rashevskaya, I., Vacchi, A., Zampa, G., Zampa, N., Bellutti, P., Giacomini, G., Picciotto, A., and Piemonte, C., 2015, *A Silicon Drift Detector-CMOS Front-end System for High Resolution X-ray Spectroscopy up to Room Temperature*, Journal of Instrumentation, Vol. 10, Art. No. P01002.

Bolton, S.J., Lunine, J., Stevenson, D., Connerney, J.E.P., Levin, S., Owen, T.C., Bagenal, F., Gautier, D., Ingersoll, A.P., Orton, G.S., Guillot, T., Hubbard, W., Bloxham, J., Coradini, A., Stephens, S.K., Mokashi, P., Thorne, R., and Thorpe, R., 2017, *The Juno Mission*, Space Science Reviews, Vol. 213, pp. 5-37.

Borges, F.I.G.M., and Conde, C.A.N., 1996, *Experimental W-values in Gaseous Xe, Kr and Ar for Low Energy X-rays*, Nuclear Instruments and Methods in Physics Research A, Vol. 381, pp. 91-96.

Boynton, R.J., Mourenas, D., and Balikhin, M.A., 2016, *Electron Flux Dropouts at Geostationary Earth Orbit: Occurrences, Magnitudes, and Main Driving Factors*, Journal of Geophysical Research: Space Physics, Vol. 121, pp. 8448-8461.

Bruzzi, M., Lagomarsino, S., Nava, F., and Sciortino, S., 2003, *Characterisation of Epitaxial SiC Schottky Barriers as Particle Detectors*, Diamond and Related Materials, Vol. 12, pp. 1205-1208.

Burrows, D.N., Hill, J.E., Nousek, J.A., Kennea, J.A., Wells, A., Osborne, J.P., Abbey, A.F., Beardmore, A., Mukerjee, K., Short, A.D.T., Chincarini, G., Campana, S., Citterio, O., Moretti, A., Pagani, C., Tagliaferri, G., Giommi, P., Capalbi, M., Tamburelli, F., Angelini, L., Cusumano, G., Bräuninger, H.W., Burkert, W., and Hartner, G.D., 2005, *The Swift X-ray Telescope*, Space Science Reviews, Vol. 120, pp. 165-195.

Butera, S., Lioliou, G., Krysa, A.B., and Barnett, A.M., 2016a, *Characterisation of $Al_{0.52}In_{0.48}P$ Mesa p-i-n Photodiodes for X-ray Photon Counting Spectroscopy*, Journal of Applied Physics, Vol. 120, Art. No. 024502.

Butera, S., Gohil, T., Lioliou, G., Krysa, A.B., and Barnett, A.M., 2016b, *Temperature Study of $Al_{0.52}In_{0.48}P$ detector photon counting X-ray Spectrometer*, Journal of Applied Physics, Vol. 120, Art. No. 174503.

Butera, S., Lioliou, G., Krysa, A.B., and Barnett, A.M., 2017, *InGaP (GaInP) Mesa p-i-n Photodiodes for X-ray Photon Counting Spectroscopy*, Scientific Reports, Vol. 7, Art. No. 10206.

Butera, S., Lioliou, G., Krysa, A.B., and Barnett, A.M., 2018a, *Temperature Characterisation of Spectroscopic InGaP X-ray Photodiodes*, Nuclear Instruments and Methods in Physics Research A, Vol. 908, pp. 277-284.

Butera, S., Lioliou, G., Krysa, A.B., and Barnett, A.M., 2018b, *Measurement of the Electron-hole Pair Creation Energy in $Al_{0.52}In_{0.48}P$ Using X-ray Radiation*, Nuclear Instruments and Methods

in Physics Research A, Vol. 879, pp. 64–68.

Casadei, D., 2014, *Solar Flare Measurements with STIX and MiSolFA*, 2014 IEEE Nuclear Science Symposium and Medical Imaging Conference, 8-15 November, Seattle, USA.

Casadei, D., Jeffrey, N.L.S., and Kontar, E.P., 2017, *Measuring X-ray Anisotropy in Solar Flares. Prospective Stereoscopic Capabilities of STIX and MiSolFA*, Astronomy and Astrophysics, Vol. 606, Art. No. A2.

Cheong, J.S., Ong, J.S., Ng, J.S., Krysa, A.B., and David, J.P.R., 2014, *$Al_{0.52}In_{0.48}P$ SAM-APD as a Blue-Green Detector*, IEEE Journal on Selected Topics in Quantum Electronics, Vol. 20, Art. No. 3801305.

Cheong, J.S., Auckloo, A., Ng, J.S., Krysa, A.B., and David, J.P.R., 2015, *A High Sensitivity Detector for Underwater Communication Systems*, Proceedings of SPIE - The International Society for Optical Engineering, Vol. 9647, Art. No. 96470O.

Comerford, J.M., Pooley, D., Gerke, B.F., and Madejski, G.M., 2011, *Chandra Observations of A 1.9kpc Separation Double X-ray Source in a Candidate Dual Active Galactic Nucleus Galactic Nucleus Galaxy at z=0.16*, Astrophysical Journal Letters, Vol. 747, Art. No. L19.

Costa, E., Frontera, F., Heise, J., Feroci, M., In 'T Zand, J., Fiore, F., Cinti, M.N., Dal Fiume, D., Nicastro, L.b, Orlandini, M., Palazzi, E., Rapisarda, M., Zavattini, G., Jager, R., Parmar, A., Owens, A., Molendi, S., Cusumano, G., Maccarone, M.C., Giarrusso, S., Coletta, A., Antonelli, L.A., Giommi, P., Muller, J.M., Piro, L., and Butlers, R.C., 1997, *Discovery of an X-ray Afterglow Associated with the γ-ray Burst of 28 February 1997*, Nature, Vol. 387, pp. 783-785.

Cromer, D.T., and Liberman, D., 1970, *Relativistic Calculation of Anomalous Scattering Factors for X-rays*, The Journal of Chemical Physics, Vol. 53, pp. 1891-1898.

Culhane, J.L., Hiei, E., Doschek, G.A., Cruise, A.M., Ogawara, Y., Uchida, Y., Bentley, R.D., Brown, C.M., Lang, J., Watanabe, T., Bowles, J.A., Deslattes, R.D., Feldman, U., Fludra, A., Guttridge, P., Henins, A., Lapington, J., Magraw, J., Mariska, J.T., Payne, J., Phillips, K.J.H., Sheather, P., Slater, K., Tanaka, K., Towndrow, E., Trow, M.W., and Yamaguchi, A., 1991, *The Bragg Crystal Spectrometer for SOLAR-A*, Solar Physics, Vol. 136, pp. 89-104.

Drouin, D., Hovington, P., and Gauvin, R., 1997, *CASINO: A new Monte Carlo Code in C Language for Electron Beam |Interactions - Part II: Tabulated Values of the Mott Cross Section*, Scanning, Vol. 19, pp. 20-28.

Duvet, L., Bavdaz, M., Crouzet, P.E., Nelms, N., Nowicki-Bringuier, Y.R., Shortt, B., and Verhoeve, P., 2014, *European Space Agency Detector Development for Space Science: Present and Future Activities*, Proceedings of SPIE - The International Society for Optical Engineering, Vol. 9154, Art. No. 915403.

Elvis, M., Page, C.G., Pounds, K.A., Ricketts, M.J., and Turner, M.J.L., 1975, *Discovery of Powerful Transient X-ray Source A0620 - 00 with Ariel V Sky Survey Experiment*, Nature, Vol. 257, pp. 656-657.

Emerich, C., Lamarre, J.M., Moroz, V.I., Combes, M., Sanko, N.F., Nikolsky, Y.V., Rocard, F., Gispert, R., Coron, N., Bibring, J.P., Encrenaz, T., and Crovisier, J., 1988, *Temperature and Size of the Nucleus of Comet P/Halley Deduced from IKS Infrared Vega 1 Measurements*. In: Grewing M., Praderie F., and Reinhard R., (eds) *Exploration of Halley's Comet*, Springer – Verlag, Berlin, Germany, pp. 839-842.

Fano, U., 1947, *Ionization Yield of Radiations. II. the Fluctuations of the Number of Ions*, Physical Review, Vol. 72, pp. 26-29.

Feroci, M., Stella, L., van der Klis, M., Courvoisier, T.J.L., Hernanz, M., Hudec, R., Santangelo, A., Walton, D., Zdziarski, A., Barret, D., Belloni, T., Braga, J., Brandt, S., Budtz-Jørgensen, C., Campana, S., den Herder, J.W., Huovelin, J., Israel, G.L., Pohl, M., Ray, P., Vacchi, A., Zane, S., Argan, A., Attinà, P., Bertuccio, G., Bozzo, E., Campana, R., Chakrabarty, D., Costa, E., de Rosa, A., Del Monte, E., Di Cosimo, S., Donnarumma, I., Evangelista, Y., Haas, D., Jonker, P., Korpela, S., Labanti, C., Malcovati, P., Mignani, R., Muleri, F., Rapisarda, M., Rashevsky, A., Rea, N., Rubini, A., Tenzer, C., Wilson-Hodge, C., Winter, B., Wood, K., Zampa, G., Zampa, N., Abramowicz, M.A., Alpar, M.A., Altamirano, D., Alvarez, J.M., Amati, L., Amoros, C., Antonelli, L.A., Artigue, R., Azzarello, P., Bachetti, M., Baldazzi, G., Barbera, M., Barbieri, C., Basa, S., Baykal, A., Belmont, R., Boirin, L., Bonvicini, V., Burderi, L., Bursa, M., Cabanac, C., Cackett, E., Caliandro, G.A., Casella, P., Chaty, S., Chenevez, J., Coe, M.J., Collura, A., Corongiu, A., Covino, S., Cusumano, G., D'Amico, F., Dall'Osso, S., de Martino, D., de Paris, G., Di Persio, G., Di Salvo, T., Done, C., Dovčiak, M., Drago, A., Ertan, U., Fabiani, S., Falanga, M., Fender, R., Ferrando, P., della Monica Ferreira, D., Fraser, G., Frontera, F., Fuschino, F., Galvez, J.L., Gandhi, P., Giommi, P., Godet, O., Göğüş, E., Goldwurm, A., Götz, D., Grassi, M., Guttridge, P., Hakala, P., Henri, G., Hermsen, W., Horak, J., Hornstrup, A., in't Zand, J.J.M., Isern, J., Kalemci, E., Kanbach, G., Karas, V., Kataria, D., Kennedy, T., Klochkov, D., Kluźniak, W., Kokkotas, K., Kreykenbohm, I., Krolik, J., Kuiper, L., Kuvvetli, I., Kylafis, N., Lattimer, J.M., Lazzarotto, F., Leahy, D., Lebrun, F., Lin, D., Lund, N., Maccarone, T., Malzac, J., Marisaldi, M., Martindale, A., Mastropietro, M., McClintock, J., McHardy, I., Mendez, M., Mereghetti, S., Miller, M.C.,

Mineo, T., Morelli, E., Morsink, S., Motch, C., Motta, S., Muñoz-Darias, T., Naletto, G., Neustroev, V., Nevalainen, J., Olive, J.F., Orio, M., Orlandini, M., Orleanski, P., Ozel, F., Pacciani, L., Paltani, S., Papadakis, I., Papitto, A., Patruno, A., Pellizzoni, A., Petráček, V., Petri, J., Petrucci, P.O., Phlips, B., Picolli, L., Possenti, A., Psaltis, D., Rambaud, D., Reig, P., Remillard, R., Rodriguez, J., Romano, P., Romanova, M., Schanz, T., Schmid, C., Segreto, A., Shearer, A., Smith, A., Smith, P.J., Soffitta, P., Stergioulas, N., Stolarski, M., Stuchlik, Z., Tiengo, A., Torres, D., Török, G., Turolla, R., Uttley, P., Vaughan, S., Vercellone, S., Waters, R., Watts, A., Wawrzaszek, R., Webb, N., Wilms, J., Zampieri, L., Zezas, A., and Ziolkowski, J., 2012, *The Large Observatory for X-ray Timing (LOFT)*, Experimental Astronomy, Vol. 34, pp. 415-444.

Fioretti, V., Bulgarelli, A., Molendi, S., Lotti, S., Macculi, C., Barbera, M., Mineo, T., Piro, L., Cappi, M., Dadina, M., Meidinger, N., Von Kienlin, A., and Rau, A., 2018, *Magnetic Shielding of Soft Protons in Future X-Ray Telescopes: The Case of the ATHENA Wide Field Imager*, Astrophysical Journal, Vol. 867, Art. No. 9.

Flakus, F. N., 1981, *Radiation Detection: Detecting and Measuring Ionizing Radiation – A Short History*, IAEA Bulletin, Vol. 23, pp. 31–36.

Fraser, G.W., 1989, *X-ray Detectors in Astronomy*, Cambridge University Press, Cambridge, UK.

Fraser, G.W., Abbey, A.F., Holland, A., McCarthy, K., Owens, A., and Wells, A., 1994, *The X-ray Energy Response of Silicon Part A. Theory*, Nuclear Instruments and Methods in Physics Research A, Vol. 350, pp. 368-378.

Fraser, G.W., 2008, *Extraterrestrial Analysis: Planetary X-ray Fluorescence from Orbiting Spacecraft and Landers, in Portable X-ray Fluorescence Spectroscopy: Capabilities for In-situ Analysis*, RSC Publishing, Cambridge, UK.

Fraser, G.W., Carpenter, J.D., Rothery, D.A., Pearson, J.F., Martindale, A., Huovelin, J., Treis, J., Anand, M., Anttila, M., Ashcroft, M., Benkoff, J., Bland, P., Bowyer, A., Bradley, A., Bridges, J., Brown, C., Bulloch, C., Bunce, E.J., Christensen, U., Evans, M., Fairbend, R., Feasey, M., Giannini, F., Hermann, S., Hesse, M., Hilchenbach, M., Jorden, T., Joy, K., Kaipiainen, M., Kitchingman, I., Lechner, P., Lutz, G., Malkki, A., Muinonen, K., Näränen, J., Portin, P., Prydderch, M., Juan, J.S., Sclater, E., Schyns, E., Stevenson, T.J., Strüder, L., Syrjasuo, M., Talboys, D., Thomas, P., Whitford, C., and Whitehead, S., 2010, *The Mercury Imaging X-ray Spectrometer (MIXS) on Bepicolombo*, Planetary and Space Science, Vol. 58, pp. 79-95.

Gatti, E., Manfredi, P.F., Sampietro, M., and Speziali, V., 1990, *Suboptimal Filtering of 1/f-Noise in Detector Charge Measurements*, Nuclear Instruments and Methods in Physics Research A, Vol. 297, pp. 467-478.

Garmire, G.P., Bautz, M.W., Ford, P.G., Nousek, J.A., and Ricker Jr., G.R., 2002, *Advanced CCD Imaging Spectrometer (ACIS) Instrument on the Chandra X-ray Observatory*, Proceedings of SPIE - The International Society for Optical Engineering, Vol. 4851, pp. 28-44.

Gehrels, N., Chincarini, G., Giommi, P., Mason, K.O., Nousek, J.A., Wells, A.A., White, N.E., Barthelmy, S.D., Burrows, D.N., Cominsky, L.R., Hurley, K.C., Marshall, F.E., Mészáros, P., Roming, P.W.A., Angelini, L., Barbier, L.M., Belloni, T., Campana, S., Caraveo, P.A., Chester, M.M., Citterio, O., Cline, T.L., Cropper, M.S., Cummings, J.R., Dean, A.J., Feigelson, E.D., Fenimore, E.E., Frail, D.A., Fruchter, A.S., Garmire, G.P., Gendreau, K., Ghisellini, G., Greiner, J., Hill, J.E., Hunsberger, S.D., Krimm, H.A., Kulkarni, S.R., Kumar, P., Lebrun, F., Lloyd-Ronning, N.M., Markwardt, C.B., Mattson, B.J., Mushotzky, R.F., Norris, J.P., Osborne, J., Paczynski, B., Palmer, D.M., Park, H.S., Parsons, A.M., Paul, J., Rees, M.J., Reynolds, C.S., Rhoads, J.E., Sasseen, T.P., Schaefer, B.E., Short, A.T., Smale, A.P., Smith, I.A., Stella, L., Tagliaferri, G., Takahashi, T., Tashiro, M., Townsley, L.K., Tueller, J., Turner, M.J.L., Vietri, M., Voges, W., Ward, M.J., Willingale, R., Zerbi, F.M., and Zhang, W.W., 2004, *The Swift Gamma-ray Burst Mission*, The Astrophysical Journal, Vol. 611, pp. 1005-1020.

Gellert, R., Campbell, J.L., King, P.L., Leshin, L.A., Lugmair, G.W., Spray, J.G., Squyres, S.W., and Yen, A.S., 2009, *The Alpha-Particle-X-Ray-Spectrometer(APXS) for the Mars Science Laboratory (MSL) Rover Mission*, 40th Lunar and Planetary Science Conference, (Lunar and Planetary Science XL), 23-27 March, Woodlands, Texas.

Gohil, T., Whale, J., Lioliou, G., Novikov, S.V., Foxon, C.T., Kent, A.J., and Barnett, A.M., 2016, *X-ray Detection with Zinc-Blende (Cubic) GaN Schottky Diodes*, Scientific Reports, Vol. 6, Art. No. 29535.

Greenwood, N.N., and Earnshaw, A., 1997, *Chemistry of the Elements*, Butterworth-Heinemann.

Grimm, O., Bednarzik, M., Birrer, G., Arnold, N., Commchau, V., Hurford, G., Krucker, S., Limousin, O., and Meuris, A., 2015, *Performance and Qualification of CdTe Pixel Detectors for the Spectrometer/Telescope for Imaging X-rays*, Journal of Instrumentation, Vol. 10, Art. No. C02011.

Grotzinger, J.P., Crisp, J., Vasavada, A.R., Anderson, R.C., Baker, C.J., Barry, R., Blake, D.F.,

Conrad, P., Edgett, K.S., Ferdowski, B., Gellert, R., Gilbert, J.B., Golombek, M., Gómez-Elvira, J., Hassler, D.M., Jandura, L., Litvak, M., Mahaffy, P., Maki, J., Meyer, M., Malin, M.C., Mitrofanov, I., Simmonds, J.J., Vaniman, D., Welch, R.V., and Wiens, R.C., 2012, *Mars Science Laboratory Mission and Science Investigation*, Space Science Reviews, Vol. 170, pp. 5-56.

Guainazzi, M., 2013, *XMM-Newton Scientific Highlights: X-ray Spectroscopic Population Studies of AGN*, Acta Polytechnica, Vol. 53, pp. 626-630.

Hall, D.J., and Holland, A., 2010, *Space Radiation Environment Effects of X-ray CCD Background*, Nuclear Instruments and Methods in Physics Research A, Vol. 612, pp. 320-327.

Hameury, J.M., Barret, D., Lasota, J.P., McClintock, J.E., Menou, K., Motch, C., Olive, J.F., and Webb, N., 2003, *XMM-Newton Observations of Two Black Hole X-ray Transients in Quiescence*, Astronomy and Astronphysics, Vol. 399, pp. 631-637.

Hansson, C.T.C., Owens, A., and van den Biezen, J., 2014, *X-ray, γ-ray and Neutron Detector Development for Future Space Instrumentation*, Acta Astronautica, Vol. 93, pp. 121-128.

Hartnett, J.G., Mouneyrac, D., Krupka, J., le Floch, J.M., Tobar, M.E., and Cros, D., 2011, *Microwave Properties of Semi-insulating Silicon Carbide Between 10 and 40 GHz and at Cryogenic Temperatures*, Journal of Applied Physics, Vol. 109, Art. No. 064107.

Hassler, D.M., Zeitlin, C., Wimmer-Schweingruber, R.F., Böttcher, S., Martin, C., Andrews, J., Böhm, E., Brinza, D.E., Bullock, M.A., Burmeister, S., Ehresmann, B., Epperly, M., Grinspoon, D., Köhler, J., Kortmann, O., Neal, K., Peterson, J., Posner, A., Rafkin, S., Seimetz, L., Smith, K.D., Tyler, Y., Weigle, G., Reitz, G., and Cucinotta, F.A., 2012, *The Radiation Assessement Detector (RAD) Investigation*, Space Science Reviews, Vol. 170, pp. 503-558.

Hayes, L.A., Gallagher, P.T., McCauley, J., Dennis, B.R., Ireland, J., and Inglis, A., 2017, *Pulsations in the Earth's Lower Ionosphere Synchronized with Solar Flare Emission*, Journal of Geophysical Research: Space Physics, Vol. 122, pp. 9841-9847.

He, Z., 2001, *Review of the Shockley-Ramo theorem and its Application in Semiconductor Gamma-ray Detectors*, Nuclear Instruments and Methods in Physics Research A, Vol. 463, pp. 250-267.

Henke, B.L., Gullikson, E.M., and Davis, J.C., 1993, *X-ray Interactions: Photoabsorption, Scattering, Transmission, and Reflection at E = 50-30,000 eV, Z = 1-92*, Atomic Data and Nuclear Data Tables, Vol. 54, pp. 181-342.

Hewlett Packard, 1979, *Model HP 4275A Multi-frequency LCR Meter Operating Manual*, 04275-90004, Tokyo, Japan.

Hovington, P., Drouin, D., and Gauvin, R., 1997, *CASINO: A new Monte Carlo Code in C Language for Electron Beam Interaction - Part I: Description of the Program*, Scanning, Vol. 19, pp. 1-14.

Hubbell, J.H., 1982, *Photon Mass Attenuation and Energy-absorption Coefficients*, The International Journal of Applied Radiation and Isotopes, Vol. 33, pp. 1269-1290.

Jansen, F., Lumb, D., Altieri, B., Clavel, J., Ehle, M., Erd, C., Gabriel, C., Guainazzi, M., Gondoin, P., Much, R., Munoz, R., Santos, M., Schartel, N., Texier, D., Vacanti, G., 2001, *XMM-Newton Observatory. 1. The Spacecraft and Operations*, Astronomy and Astrophysics, Vol. 365, pp. L1-L6.

Jenkins, R., Gould, R.W., and Gedcke, D., 1995, *Quantitative X-ray Spectrometry*, 2nd ed., CRC Press, New York.

Johnson, T.V., Yeates, C.M., and Young, R., 1992, *Space Science Reviews Volume on Galileo Mission Overview*, Space Science Reviews, Vol. 60, pp. 3-21.

Jung, H.S., Yang, W.I., Cho, M.S., Joo, K.N., and Lee, S.Y., 2014, *Microwave Losses of Undoped n-type Silicon and Undoped 4H-SiC Single Crystals at Cryogenic Temperatures*, Electronic Materials Letters, Vol. 10, pp. 541-549.

Keithley Instruments, 2011, *Model 6487 Picoammeter/Voltage Source Reference Manual*, 6487-901-01 Rev C, Ohio, USA.

Keithley Instruments, 2013, *Low Level Measurements Handbook*, 7th ed., Ohio, USA.

Klaassen, F.M., 1971, *Comments on Hot Carrier Noise in Filed-effect Transistors*, IEEE Transactions on Nuclear Devices, Vol. 18, pp. 74-75.

Knoll, G.F., 2010, *Radiation Detection and Measurements*, 4th ed., John Wiley & Sons Ltd, Chichester, UK.

Kolawa, E., Balint, T., Birur, G., Bolotin, G., Brandon, E., Del Castillo, L., Garrett, H., Hall, J., Johnson, M., Jones, J., Jun, I., Manvi, R., Mojarradi, M., Moussessian, A., Patel, J., Pauken, M., Peterson, C., Surampudi, R., Schone, H., Whitacre, J., Martinez, E., Laub, B., Venkapathy, R., and Neudeck, P., 2007, *Extreme Environment Technologies for Future Space Science Missions*,

Technical Reports, JPL D-32832.

Kosugi, T., Makishima, K., Murakami, T., Sakao, T., Dotani, T., Inda, M., Kai, K., Masuda, S., Nakajima, H., Ogawara, Y., Sawa, M., and Shibasaki, K., 1991, *The Hard X-ray Telescope (HXT) for the SOLAR-A Mission*, Solar Physics, Vol. 136, pp. 17-36.

Kotz, J., Treichel, P., and Townsend, J., 2008, *Chemistry and Chemical Reactivity*, 7th ed., Cengage Learning, Inc, Belmont, CA, USA.

Krucker, S., Benz, A.O., Hurford, G.J., Arnold, N.G., Orleański, P., Gröbelbauer, H.P., Casadei, D., Kobler, S., Iseli, L., Wiehl, H.J., Csillaghy, A., Etesi, L., Hochmuth, N., Battaglia, M., Bednarzik, M., Resanovic, R., Grimm, O., Viertel, G., Commichau, V., Howard, A., Meuris, A., Limousin, O., Brun, S., Vilmer, N., Skup, K.R., Graczyk, R., Stolarski, M., Michalska, M., Nowosielski, W., Cichocki, A., Mosdorf, M., Seweryn, K., Białek, A., Sylwester, J., Kowalinski, M., Mrozek, T., Podgorski, P., Mann, G., Önel, H., Aurass, H., Bauer, S.M., Bittner, W., Dionies, F., Paschke, J., Plüschke, D., Popow, E., Rendtel, J., Warmuth, A., Woche, M., Wolter, D., Van Beek, H.F., Farnik, F., and Lin, R.P., 2013, *The Spectrometer/telescope for Imaging X-rays on Board the ESA Solar Orbiter Spacecraft*, Nuclear Instruments and Methods in Physics Research A, Vol. 732, pp. 295-298.

Krupka, J., Mouneyrac, D., Hartnett, J.G., and Tobar, M.E., 2008, *Use of Whispering-Gallery Modes and Quasi- TE_{0np} Modes for Broadband Characterization of Bulk Gallium Arsenide and Gallium Phosphide Samples*, IEEE Transactions on Microwave Theory and Techniques, Vol. 56, pp. 1201-1206.

Ladislas Wiza, L., 1979, *Microchannel Plate Detectors*, Nuclear Instruments and Methods, Vol. 162, pp. 587-601.

LD Didactic GmbH, N.D., *Instruction Sheet 554 800*, Federal Republic of Germany.

Lees, J.E., Barnett, A.M., Bassford, D.J., and Mazzillo, M., 2012, *X-ray and Electron Response of 4H-SiC Vertical Interdigitated Schottky Photodiodes*, Journal of Instrumentation, Vol. 7, Art. No. P11024.

Leo, W.R., 1994, *Techniques for Nuclear and Particle Physics Experiments: A How-to Approach*, 2nd ed., Springer-Verlag, Berlin, Germany.

Leroy, C., and Rancoita, P.G., 2016, *Principles of Radiation Interaction in Matter and Detection*, 4th ed., World Scientific, New Jersey.

Levinshtein, M.E., Rumyantsev, S.L., and Shur, M.S., 2001, *Properties of Advanced Semiconductor Materials: GaN, AIN, InN, BN, SiC, SiGe*, John Wiley and Sons Ltd, New York, USA.

Lide, D.R., 2003, *CRC Handbook of Chemistry and Physics*, CRC Press, 84 th ed., Bosa Roca, USA.

Lin, R.P., Dennis, B.R., Hurford, G.J., Smith, D.M., Zehnder, A., Harvey, P.R., Curtis, D.W., Pankow, D., Turin, P., Bester, M., Csillaghy, A., Lewis, M., Madden, N., Van Beek, H.F., Appleby, M., Raudorf, T., McTiernan, J., Ramaty, R., Schmahl, E., Schwartz, R., Krucker, S., Abiad, R., Quinn, T., Berg, P., Hashii, M., Sterling, R., Jackson, R., Pratt, R., Campbell, R.D., Malone, D., Landis, D., Barrington-Leigh, C.P., Slassi-Sennou, S., Cork, C., Clark, D., Amato, D., Orwig, L., Boyle, R., Banks, I.S., Shirey, K., Tolbert, A.K., Zarro, D., Snow, F., Thomsen, K., Henneck, R., Mchedlishvili, A., Ming, P., Fivian, M., Jordan, J., Wanner, R., Crubb, J., Preble, J., Matranga, M., Benz, A., Hudson, H., Canfield, R.C., Holman, G.D., Crannell, C., Kosugi, T., Emslie, A.G., Vilmer, N., Brown, J.C., Johns-Krull, C., Aschwanden, M., Metcalf, T., and Conway, A., 2002, *The Reuven Ramaty High-energy Solar Spectroscopic Imager (RHESSI)*, Solar Physics, Vol. 210, pp. 3-32.

Lindström, G., 2003, *Radiation Damage in Silicon Detectors*. Nuclear Instruments and Methods in Physics Research A, Vol. 512, pp. 30-43.

Lioliou, G., and Barnett, A.M, 2015, *Electronic Noise in Charge Sensitive Preamplifiers for X-ray Spectroscopy and the Benefits of a SiC Input JFET*, Nuclear Instruments and Methods in Physics Research A, Vol. 801, pp. 63-72.

Lioliou, G., and Barnett, A.M., 2016, *Gallium Arsenide Detectors for X-ray and Electron (Beta Particle) Spectroscopy*, Nuclear Instruments and Methods in Physics Research A, Vol. 836, pp. 37-45.

Lioliou, G., Meng, X., Ng, J.S., and Barnett, A.M., 2016a, *Characterization of Gallium Arsenide X-ray Mesa p-i-n Photodiodes at Room Temperature*, Nuclear Instruments and Methods in Physics Research A, Vol. 813, pp. 1-9.

Lioliou, G., Meng, X., Ng, J.S., and Barnett, A.M., 2016b, *Temperature Dependent Characterization of Gallium Arsenide X-ray Mesa p-i-n Photodiodes*, Journal of Applied Physics, Vol. 119, Art. No. 124507.

Lioliou, G., Chan, H.K., Gohil, T., Vassilevski, K.V., Wright, N.G., Horsfall, A.B., and Barnett,

A.M., 2016c, *4H-SiC Schottky Diode Arrays for X-ray Detection*, Nuclear Instruments and Methods in Physics Research A, Vol. 840, pp. 145-152.

Liu, Y.P., Tang, X.B., Xu, Z.H., Hong, L., Wang, H., Liu, M., and Chen, D., 2015, *Influences of Planar Source Thickness on Betavoltaics with Different Semiconductors*, Journal of Radioanalytical and Nuclear Chemistry, Vol. 304, pp. 517-525.

Loh, W.S., Ng, B.K., Ng, J.S., Soloviev, S.I., Cha, H.Y., Sandvik, P.M., Johnson, C.M., and David, J.P.R., 2008, *Impact Ionization Coefficients in 4H-SiC*, IEEE Transactions on Electron Devices, Vol. 55, pp. 1984-1990.

Lowe, B.G., and Sareen, R.A., 2013, *Semiconductor X-ray Detectors*, Taylor & Francis Group, Boca Raton, USA.

Lutz, G., 2006, *Silicon Drift and Pixel Devices for X-ray Imaging and Spectroscopy*, Journal of Synchrotron Radiation, Vol. 13, pp. 99-109.

Mauk, B.H., Haggerty, D.K., Jaskulek, S.E., Schlemm, C.E., Brown, L.E., Cooper, S.A., Gurnee, R.S., Hammock, C.M., Hayes, J.R., Ho, G.C., Hutcheson, J.C., Jacques, A.D., Kerem, S., Kim, C.K., Mitchell, D.G., Nelson, K.S., Paranicas, C.P., Paschalidis, N., Rossano, E., and Stokes, M.R., 2017, *The Jupiter Energetic Particle Detector Instrument (JEDI) Investigation for the Juno Mission*, Space Science Reviews, Vol. 213, pp. 289-346.

Mazzillo, M., Sciuto, A., Catania, G., Roccaforte, F., and Raineri, V., 2012, *Temperature and Light Induced Effects on the Capacitance of 4H-SiC Schottky Photodiodes*, IEEE Sensors Journal, Vol. 12, pp. 1127-1130.

McComas, D.J., Alexander, N., Allegrini, F., Bagenal, F., Beebe, C., Clark, G., Crary, F., Desai, M.I., De Los Santos, A., Demkee, D., Dickinson, J., Everett, D., Finley, T., Gribanova, A., Hill, R., Johnson, J., Kofoed, C., Loeffler, C., Louarn, P., Maple, M., Mills, W., Pollock, C., Reno, M., Rodriguez, B., Rouzaud, J., Santos-Costa, D., Valek, P., Weidner, S., Wilson, P., Wilson, R.J., White, D., 2017, *The Jovian Auroral Distributions Experiment (JADE) on the Juno Mission to Jupiter*, Space Science Reviews, Vol. 213, pp. 547-643.

McGregor, D.S., and Hermon, H., 1997, *Room-temperature Compound Semiconductor Radiation Detectors*, Nuclear Instruments and Methods in Physics Research A, Vol. 395, pp. 101-124.

McKenzie, J.M., 1979, *Development of the Semiconductor Radiation Detector*, Nuclear

Instruments and Methods, Vol. 162, pp. 49-73.

McNutt, R.L., Livi, S.A., Gurnee, R.S., Hill, M.E., Cooper, K.A., Andrews, G.B., Keath, E.P., Krimigis, S.M., Mitchell, D.G., Tossman, B., Bagenal, F., Boldt, J.D., Bradley, W., Devereux, W.S., Ho, G.C., Jaskulek, S.E., LeFevere, T.W., Malcom, H., Marcus, G.A., Hayes, J.R., Moore, G.Ty, Perry, M.E., Williams, B.D., Wilson, P., Brown, L.E., Kusterer, M.B., and Vandegriff, J.D., 2008, *The Pluto Energetic Particle Spectrometer Science Investigation (PEPSSI) on the New Horizons Mission*, Space Science Reviews, Vol. 140, pp. 315-385.

Meidinger, N., Eder, J., Eraerds, T., Nandra, K., Pietschner, D., Plattner, M., Rau, A., and Strecker, R., 2016, *The Wide Field Imager Instrument for Athena*, SPIE proceedings, Space Telescopes and Instrumentation 2016: Ultraviolet to Gamma Ray, Vol. 9905, Art. No. 99052A.

Miyahara, J., Takahashi, K., Amemiya, Y., Kamiya, N., and Satow, Y., 1986, *A New Type of X-ray Area Detector Utilizing Laser Stimulated Luminescence*, Nuclear Instruments and Methods A, Vol. 246, pp. 572-578.

Müller, D., Marsden, R.G., St. Cyr, O.C., and Gilbert, H.R., 2013, *Solar Orbiter: Exploring the Sun-heliosphere Connection*, Solar Physics, Vol. 285, pp. 25-70.

Nakajima, H., Yamaguchi, H., Matsumoto, H., Tsuru, T.G., Koyama, K., Kissel, S., LaMarr, B., and Bautz, M., 2005, *The Ground Calibration of X-ray CCD Cameras (XIS) with Front-illuminated Chips Onboard Astro-E2*, Nuclear Instruments and Methods A, Vol. 541, pp. 365-371.

Nava, F., Vittone, E., Vanni, P., Verzellesi, G., Fuochi, P.G., Lanzieri, C., and Glaser, M., 2003, *Radiation Tolerance of Epitaxial Silicon Carbide Detectors for Electrons, Protons and Gamma-rays*, Nuclear Instruments and Methods in Physics Research A, Vol. 505, pp. 645-655.

Nava, F., Vanni, P., Bruzzi, M., Lagomarsino, S., Sciortino, S., Wagner, G., and Lanzieri, C., 2004, *Minimum Ionizing and Alpha Particles Detectors Based on Epitaxial Semiconductor Silicon Carbide*, IEEE Transactions on Nuclear Science, Vol. 51, pp. 238-244.

Nava, F., Bertuccio, G., Cavallini, A., and Vittone, E., 2008, *Silicon Carbide and Its Use as a Radiation Detector Material*, Measurement Science and Technology, Vol. 19, Art. No. 102001.

Nikjoo, H., Uehara, S., and Emfietzoglou, D., 2012, *Interaction of Radiation with Matter*, CRC Press, Florida, USA.

Niwa, H., Suda, J., and Kimoto, T., 2014, *Temperature Dependence of Impact Ionization*

Coefficients in 4H-SiC, Materials Science Forum, Vol. 778-780, pp. 461-466.

Novara, M., 2001, *The BepiColombo Mercury Surface Element*, Planetary and Space Science, Vol. 49, pp. 1421-1435.

Ogawara, Y., Takano, T., Kato, T., Kosugi, T., Tsuneta, S., Watanabe, T., Kondo, I., and Uchida, Y., 1991, *The SOLAR-A Mission: An Overview*, Solar Physics, Vol. 136, pp. 1-16.

Ong, J.S.L., Ng, J.S., Krysa, A.B., and David, J.P.R., 2011, *Impact Ionization Coefficients in* $Al_{0.52}In_{0.48}P$, IEEE Electron Device Letters, Vol. 32, pp. 1528-1530.

Owens, A., Bavdaz, M., Peacock, A., Poelaert, A., Andersson, H., Nenonen, S., Sipila, H., Tröger, L., and Bertuccio, G., 2001, *High Resolution X-ray Spectroscopy Using GaAs Arrays*, Journal of Applied Physics, Vol. 90, pp. 5376-5381.

Owens, A., Bavdaz, M., Peacock, A., Andersson, H., Nenonen, S., Krumrey, M., and Puig, A., 2002, *High Resolution X-ray Spectroscopy Using a GaAs Pixel Detector*, Nuclear Instruments and Methods in Physics Research A, Vol. 479, pp. 531-534.

Owens, A., and Peacock, A., 2004, *Compound Semiconductor Radiation Detectors*, Nuclear Instruments and Methods in Physics Research A, Vol. 531, pp. 18-37.

Owens, A., 2012, *Compound Semiconductor Radiation Detectors*, Taylor & Francis Inc, Bosa Roca, USA.

Owens, A., Barnes, A., Farley, R.A., Germain, M., and Sellin, P.J., 2012, *GaN Detector Development for Particle and X-ray Detection*, Nuclear Instruments and Methods in Physics Research A, Vol. 695, pp. 303-305.

Patrick, L., and Choyke, W.J., 1970, *Static Dielectric Constant of SiC*, Physical Review B, Vol. 2, pp. 2255-2256.

Paradijs, J.V., and Bleeker, J.A.M., 1999, *X-ray Spectroscopy in Astrophysics*, Springer-Verlag, Berlin Heidelberg.

Prasai, D., John, W., Weixelbaum, L., Krügera, O., Wagner, G., Sperfeld, P., Nowy, S., Friedrich, D., Winter, S., and Weiss, T., 2013, *Highly Reliable Silicon Carbide Photodiodes for Visible-blind Ultraviolet Detector Applications*, Journal of Materials Research, Vol. 28, pp. 33-37.

Pullia, A., and Bertuccio, G., 1996, *Resolution Limits of Silicon Detectors and Electronics for*

Soft X-ray Spectroscopy at Non Cryogenic Temperatures, Nuclear Instruments and Methods in Physics Research A, Vol. 380, pp. 1-5.

Raghunathan, R., and Baliga, B.J., 1999, *Temperature Dependence of Hole Impact Ionization Coefficients in 4H and 6H-SiC*, Solid-State Electronics, Vol. 43, pp. 199-211.

Richards, P.G., 2013, *Solar Cycle Changes in the Photochemistry of the Ionosphere and Thermosphere*, Geophysical Monograph Series, Vol. 201, pp. 29-37.

Rogalla, M., Runge, K., and Söldner-Rembold, A., 1999, *Particle Detectors Based on Semi-insulating Silicon Carbide*, Nuclear Physics B - Proceedings Supplements, Vol. 78, pp. 516-520.

Ruddy, F.H., Seidel, J.G., Chen, H., Dulloo, A.R., and Ryu, S.H., 2006, *High-resolution Alpha-particle Spectrometry Using 4H Silicon Carbide Semiconductor Detectors*, IEEE Transactions on Nuclear Science, Vol. 53, pp. 1713-1718.

Sánchez del Rio, M., Brunetti, A., Golosio, B., Somogyi, A., and Simionovici, A., 2003, *XRAYLIB Tables (X-ray Fluorescence Cross-section)*, European Synchrotron Radiation Facility and University of Sassari.

Santangelo, A., and Madonia, R., 2014, *Fifty Yearys of X-ray Astronomy: A Look Back and into the (Near) Future*, Astroparticle Physics, Vol. 53, pp. 130-151.

Sellin, P.J., 2003, *Recent Advances in Compound Semiconductor Radiation Detectors*, Nuclear Instruments and Methods in Physics Research A, Vol. 513, pp. 332-339.

Sellin, P.J., and Vaitkus, J., 2006, *New Materials for Radiation Hard Semiconductor Detectors*, Nuclear Instruments and Methods in Physics Research A, Vol. 557, pp. 479-489.

Schötzig, U., 2000, *Half-life and X-ray Emission Probabilities of ^{55}Fe*, Applied Radiation and Isotopes, Vol. 53, pp. 469-472.

Schroder, D., 2006, *Semiconductor Material and Device Characterisation*, 3rd ed., John Wiley & Sons, New Jersey, USA.

Schwartz, D.A., 2014, *Invited Review Article: The Chandra X-ray Observatory*, Review of Scientific Instruments, Vol. 85, Art. No. 061101.

Seward, F.D., and Charles, P.A., 2010, *Exploring the X-ray Universe*, 2nd ed., Cambridge

University Press, New York, USA.

Seyller, T., 2006, *Electronic Properties of SiC Surfaces and Interfaces: Some Fundamental and Technological Aspects*, Applied Physics A: Materials Science and Processing, Vol. 85, pp. 371-385.

Sims, G.H.E., and Juhnke, D.G., 1967, *The Beta Self-absorption of Ni^{63} as Metallic Nickel*, The International Journal Of Applied Radiation And Isotopes, Vol. 18, pp. 727-728.

Sims, M.R., Pillinger, C.T., Wright, I.P., Dowson, J., Whitehead, S., Wells, A., Spragg, J.E., Fraser, G., Richter, L., Hamacher, H., Johnstone, A., Meredith, N.P., de la Nougerede, C., Hancock, B., Turner, R., Peskett, S., Brack, A., Hobbs, J., Newns, M., Senior, A., Humphries, M., Keller, H.U., Thomas, N., Lingard, J.S., Underwood, J.C., Sale, N.M., Neal, M.F., Klingelhofer, G., and Ng, T.C., 1999, *Beagle-2: A Proposed Exobiology Lander for ESA's 2003 Mars Express Mission*, Advances in Space Research, Vol. 23, pp. 1925-1928.

Siliconix, 2001, *2N4416/2N4416A/SST4416 N-Channel JFETs*, Data Sheet, 70242 S-04028, Rev. F, 04-Jun-01, Vishay Electronic GmbH, Selb, Germany.

Smith, D.M., Lin, R.P., Turin, P., Curtis, D.W., Primbsch, J.H., Campbell, R.D., Abiad, R., Schroeder, P., Cork, C.P., Hull, E.L., Landis, D.A., Madden, N.W., Malone, D., Pehl, R.H., Raudorf, T., Sangsingkeow, P., Boyle, R., Banks, I.S., Shirey, K., and Schwartz, R., 2002, *The RHESSI Spectrometer*, Solar Physics, Vol. 210, pp. 33-60.

Spahn, M., Strotzer, M., Völk, M., Böhm, S., Geiger, B., Hahm, G., and Feuerbach, S., 2000, *Digital Radiography with A Large-area, Amorphous-silicon, Flat-panel X-ray Detector System*, Investigative Radiology, Vol. 35, pp. 260-266.

Spieler, H., 2005, *Semiconductor Detector Systems*, Oxford University Press, New York, USA.

Strüder, L., Briel, U., Dennerl, K., Hartmann, R., Kendziorra, E., Meidinger, N., Pfeffermann, E., Reppin, C., Aschenbach, B., Bornemann, W., Bräuninger, H., Burkert, W., Elender, M., Freyberg, M., Haberl, F., Hartner, G., Heuschmann, F., Hippmann, H., Kastelic, E., Kemmer, S., Kettenring, G., Kink, W., Krause, N., Müller, S., Oppitz, A., Pietsch, W., Popp, M., Predehl, P., Read, A., Stephan, K.H., Stötter, D., Trümper, J., Holl, P., Kemmer, J., Soltau, H., Stötter, R., Weber, U., Weichert, U., Von Zanthier, C., Carathanassis, D., Lutz, G., Richter, R.H., Solc, P., Böttcher, H., Kuster, M., Staubert, R., Abbey, A., Holland, A., Turner, M., Balasini, M., Bignami, G.F., La Palombara, N., Villa, G., Buttler, W., Gianini, F., Lainé, R., Lumb, D., and Dhez, P., 2001, *The European Photon Imaging Camera on XMM-Newton: The pn-CCD Camera*,

Astronomy and Astrophysics, Vol. 365, pp. L18-L26.

Sze, S.M., 1985, *Physics of Semiconductor Devices*, John Wiley & Sons, New Jersey, USA.

Sze, S.M., and Ng, K.K., 2007, *Physics of Semiconductor Devices*, 3rd ed., John Wiley & Sons, New Jersey, USA.

Talboys, D.L., Potts, P.J., Fraser, G.W., Butcher, G., and Wegrzynek, D., 2009, *The Comparative Analytical Performance of the Beagle 2 X-ray Spectrometer for In-situ Geochemical Analysis on Mars*, X ray Spectrometry, Vol. 38, pp. 417-428.

Tavendale, A.J., and Ewan, G.T., 1963, *A High Resolution Lithium-drift Germanium Gamma-ray Spectrometer*, Nuclear Instruments and Methods, Vol. 25, pp. 185-187.

Torrisi, L., Sciuto, A., Calcagno, L., Musumeci, P., Mazzillo, M., Ceccio, G., and Cannavò, A., 2015, *Laser-plasma X-ray Detection by Using Fast 4H-SiC Interdigit and Ion Collector Detectors*, Journal of Instrumentation, Vol. 10, Art. No. P07009.

Trümper J., 1982, *The ROSAT Misson*, Advanced in Space Research, Vol. 2, pp. 241-249.

Tsuneta, S., Acton, L., Bruner, M., Lemen, J., Brown, W., Caravalho, R., Catura, R., Freeland, S., Jurcevich, B., Morrison, M., Ogawara, Y., Hirayama, T., and Owens, J., 1991, *The Soft X-ray Telescope for the SOLAR-A Mission*, Solar Physics, Vol. 136, pp. 37-67.

Vegard, L., 1921, *Die Konstitution der Mischkristalle und die Raumfüllung der Atome*, Zeitschrift für Physik, Vol. 5, pp. 17-26.

Weisskopf, M.C., Brinkman, B., Canizares, C., Garmire, G., Murray, S., and Van Speybroeck, L.P., 2002, *An Overview of the Performance and Scientific Results from the Chandra X-ray Observatory*, Publications of the Astronomical Society of the Pacific, Vol. 114, pp. 1-24.

Whitaker, M.D.C., Lioliou, G., Butera, S., and Barnett, A.M., 2016, *$Al_{0.2}Ga_{0.8}As$ X-ray Photodiodes for X-ray Spectroscopy*, Nuclear Instruments and Methods in Physics Research A, Vol. 840, pp. 168-173.

Whitaker, M.D.C., Butera, S., Lioliou, G., and Barnett, A.M., 2017, *Temperature Dependence of $Al_{0.2}Ga_{0.8}As$ X-ray Photodiodes for X-ray Spectroscopy*, Journal of Applied Physics, Vol. 122, Art. No. 034501.

Williams, D.J., McEntire, R.W., Jaskulek, S., and Wilken, B., 1992, *The Galileo Energetic*

Particles Detector, Space Science Reviews, Vol. 60, pp. 385-412.

Woods, T.N., Caspi, A., Chamberlin, P.C., Jones, A., Kohnert, R., Mason, J.P., Moore, C.S., Palo, S., Rouleau, C., Solomon, S.C., Machol, J., and Viereck, R., 2017, *New Solar Irradiance Measurements from the Miniature X-Ray Solar Spectrometer Cubesat*, Astrophysical Journal, Vol. 835, Art. No. 122.

Yamaguchi, M., Takamoto, T., and Araki, K., 2006, *Super High-efficiency Multi-junction and Concentrator Solar Cells*, Solar Energy Materials and Solar Cells, Vol. 90, pp. 3068-3077.

Yoshimori, M., Okudaira, K., Hirasima, Y., Igarashi, T., Akasaka, M., Takai, Y., Morimoto, K., Watanabe, T., Ohki, K., Nishimura, J., Yamagami, T., Ogawara, Y., and Kondo, I., 1991, *The Wide Band Spectrometer on the SOLAR-A*, Solar Physics, Vol. 136, pp. 69-88.

Younglove, B.A., and Olien, N.A., 1985, *Tables of Industrial Gas Container Contents and Density for Oxygen, Argon, Nitrogen, Helium, and Hydrogen*, National Institute of Standards and Technology, Gaithersbury, Maryland, USA.

Zaletin, V.M., and Varvaritsa, V.P., 2011, *Wide-bandgap Compound Semiconductors for X- or Gamma- ray Detectors*, Russian Microelectronics, Vol. 40, pp. 443-452.

Zat'ko, B., Dubecký, F., Šagátová, A., Sedlačová, K., and Ryć, L., 2015, *High Resolution Alpha Particle Detectors Based on 4H-SiC Epitaxial Layer*, Journal of Instrumentation, Vol. 10, Art. No. C04009.

Zhang, C., Lechner, P., Lutz, G., Porro, M., Richter, R., Treis, J., Strüder, L., and Nan Zhang, S., 2006, *Development of DEPFET Macropixel Detectors*, Nuclear Instruments and Methods in Physics Research A, Vol. 568, pp. 207-216.